CHARLES UNIVERSITY IN PRAGUE

Faculty of Science

Study programme: Geography

Branch of study: Geoinformatics and Cartography

Bc. Zsolt Paraj

DETECTION OF EQUILIBRIUM LINE ALTITUDE (ELA) CHANGES FROM REMOTE SENSING DATA; CASE STUDY FROM THE CORDILLERA BLANCA, PERU

ZJIŠŤOVÁNÍ ZMĚN POLOHY ELA LEDOVCŮ V POHOŘÍ CORDILLERA BLANCA, PERU Z DAT DPZ

Master thesis

Supervisor: Ing. Markéta Potůčková, Ph.D.

Advisor: Doc. RNDr. Vít Vilímek, CSc.

Prague, 2015

Prohlášení:

Prohlašuji, že jsem závěrečnou práci zpracoval/a samostatně a že jsem uvedl/a všechny použité informační zdroje a literaturu. Tato práce ani její podstatná část nebyla předložena k získání jiného nebo stejného akademického titulu.

V Praze, 29.7.2015 ……...

Zsolt Paraj

Acknowledgement:

Firstly, I would like to express my sincere gratitude to my supervisor Ing. Markéta Potůćková, Ph.D. for the continuous support of my master study, for her patience, motivation and immense knowledge. Her guidance helped me in all the time of research and writing of this thesis. Furthermore, I would like to thank Doc. RNDr. Vít Vilímek, CSc. for introducing me to the topic, as well for sharing his experience in the field of glaciology. Also, I would like to thank Mgr. Adam Emmer, Mgr. Lucie Červená and Mgr. Lukáš Brůha for their precious time and shared advice. Last but not the least, I would like to thank my loved ones for their unceasing encouragement and support.

Abstract

The aim of this diploma thesis is to monitor glacier change in the Cordillera Blanca in the period from 1987 to 2014. This diploma thesis focuses on three mountains and eleven glaciers in the northern part of the Cordillera Blanca. The input data consist of 29 Landsat scenes (Landsat 4,5,7 and 8) and the ASTER global digital elevation model version 2. Semi-automatic classification algorithm is created based on threshold values detected by spectral analyses of selected land cover types in the Cordillera Blanca. Additionally, the mean snowline (equilibrium line) altitude change is computed for all of the three mountains and eleven glaciers. Besides, glacier change depending on slope and aspect is evaluated. The results of this diploma thesis are presented in maps, tables and charts. The results of the classification are compared with the GLIMS Glacier Database and the field measurements provided by Adam Emmer, MSc. Finally, the advantages and disadvantages of the new Landsat 8 satellite sensor are discussed.

Key words: Remote sensing, Landsat, classification, ice and snow detection, ELA, Cordillera Blanca

Abstrakt

Cílem této diplomové práce je zmapovat změny ledovců v Cordillera Blanca v období od roku 1987 do roku 2014. Tato diplomová práce zaměřuje pozornost na tři hory a jedenáct ledovců v severní části Cordillera Blanca. Vstupní data tvoří 29 Landsat scén (Landsat 4,5,7 a 8) a ASTER globální digitální výškový model verze 2. Poloautomatický klasifikační algoritmus je vytvořen na základě prahových hodnot zjištěných spektrální analýzou vybraných typů krajinného pokryvu v Cordillera Blanca. Kromě toho, výšková změna střední sněžné čáry (*Equilibrium line altitude* - ELA) je vypočtena pro všechny tři hory a jedenáct ledovců. Dále je počítána změna ledovců v závislosti na sklonu a aspektu. Výsledky této práce jsou prezentovány v podobě map, tabulek a grafů. Výsledky klasifikace jsou porovnány s GLIMS databází ledovců a s terénním měřením provedeném Mgr. Adamem Emmerem. Na závěr jsou diskutovány výhody a nevýhody snímků pořízených novým satelitem Landsat 8.

Klíčová slova: DPZ, Landsat, klasifikace, mapování sněhu a ledu, ELA, Cordillera Blanca

TABLE OF CONTENTS

LIST OF FIGURES AND TABLES

Figures

Tables

LIST OF USED ABBREVIATIONS (in alphabetical order)

.dem	Digital Elevation Model file format
.num	QA (quality assessment) file format
.pdf	Portable Document Format
.qz, .tar, .zip	compressed file formats
6S	Second Simulation of a Satellite Signal in the Solar Spectrum – advanced radiative transfer code
a.s.l.	above sea level
AAR	Accumulation Area Ratio
ArcMap	ESRI ArcMap 10.2.2.
ASTER	Advanced Spaceborne Thermal Emission and Reflection Radiometer
CC	Cubic Convolution
CFmask	Cloud mask
CGIAR	Consultative Group for International Agricultural Research
DEM	Digital Elevation Model
DEM20 mask	mask of terrain with slope <= 20°
DEM25 mask	mask of terrain with slope <= 25°
E	east
EGM96	Earth Gravitational Model 1996
ELA	Equilibrium Line Altitude
GLIMS	Global Land Ice Measurements from Space
ENVI	Exelis ENVI 5.0
EOS	Earth Observing System
EOSDIS	Earth Observing System Data Information System
EPF	Extended Payload Fairing
ERS	European Remote Sensing
ERSDAC	Earth Remote Sensing Data Analysis Center
ERTS	Earth Resources Technology Satellite
ESA	European Space Agency
Excel	Microsoft Office Excel 2013
FLAASH	Fast Line-of-sight Atmospheric Analysis of Hypercubes
G	green band
GCP	Ground Control Point
GDEM 2	Global Digital Elevation Model version 2
GeoTIFF	TIFF (Tagged Image File Format) file with georeferencing information
GSFC	NASA Goddard Space Flight Center
IRS	Indian Remote Sensing
ISODATA	Iterative Self-Organizing Data Analysis Technique
L4	Landsat 4
L5	Landsat 5
L7	Landsat 7
L8	Landsat 8
L8SR	Landsat 8 Surface Reflectance
Landsat CDR	Landsat Climate Data Records
Landsat ETM+	Landsat Enhanced Thematic Mapper Plus
Landsat OLI/TIRS	Landsat Operational Land Imager/Thermal Infrared Sensor

Landsat TM	Landsat Thematic Mapper
LEDAPS	Landsat Ecosystem Disturbance Adaptive Processing System
Level 1G	Systematic Correction
Level 1Gt	Systematic Terrain Correction
Level 1T	Standard Terrain Correction
LP DAAC	Land Processes Distributed Active Archive Center
LPGS	Level 1 Product Generation System
Matlab	Mathworks Matlab R2014a
MEaSUREs	Making Earth System Data Records for Use in Research Environments
METI	Ministry of Economy, Trade, and Industry
MODIS	Moderate Resolution Imaging Spectroradiometer
N	north
NASA	National Aeronautics and Space Administration
NDSI	Normalized Difference Snow Index
NDVI	Normalized Difference Vegetation Index
NDWI	Normalized Difference Water Index
NE	northeast
NIR	Near Infrared band
NSIDC	National Snow and Ice Data Center
NW	northwest
QUAC	QUick Atmospheric Correction
R	red band
RGB	Red Green Blue – true color image
RMSE	Root Mean Square Error
ROI	Region of Interest
S	south
SA mask	snow mask
SA&V mask	snow and vegetation mask
SA&V&W mask	snow, vegetation and water mask
SA&V&W&D mask	snow, vegetation, water and debris-covered snow mask
SAR	Synthetic Aperture Radar
SE	southeast
SLC	Scan Line Corrector
SPOT	Satellite Pour l'Observation de la Terre
SRTM	Shuttle Radar Topography Mission
SW	southwest
SWIR	Short-Wavelength Infrared band
TIR	Thermal Infrared band
TOA	Top of Atmosphere
USGS	U.S. Geological Survey
UTM	Universal Transverse Mercator
VIS	Visible wavelength
W	west
WGS84	World Geodetic System 1984
YCEO	Yale Center for Earth Observation

1 INTRODUCTION

This diploma thesis is the result of a cooperation between the Department of Applied Geoinformatics and Cartography and the Department of Physical Geography and Geoecology of the Faculty of Science of the Charles University in Prague. The aim of this diploma thesis is to detect glacier changes in the Cordillera Blanca, Peru with the tools and methods of remote sensing.

The mapping of the glaciers and the determination of their area and volume change are important in the context of climate monitoring both on local and global scale. Glaciers contain 75% of all drinking water (National Snow and Ice Data Center, 2014) and are a crucial source of moisture for agriculture in their neighborhood. Glaciers have economic importance in terms of their hydropower (Burns and Nolin, 2014).

Detailed monitoring of high mountain glaciers is a challenging task. This is mostly because they are located in high mountain areas and often challenging terrain reduces or even eliminates their total accessibility. Remote sensing provides a solution for this problem. The methods and possibilities of obtaining data for glacier monitoring were fairly limited at the beginning of the last century, but from the second half of the 20th century, particularly as the result of the rapid development of computer technology, the situation has changed dramatically. Today, this analysis and monitoring are usually done by using a combination of satellite and aerial images (in some cases with additional measured ground data) at different points of time. The simulation of future changes can be provided on their basis at a given probability.

Collecting usable data in high mountain areas is not a trivial task, as these areas are mostly covered by clouds. Visual control is required in order to select the suitable input images. The main data sources of this diploma thesis are Landsat satellite images from several years between 1987 and 2014 and ASTER digital elevation model from the year 2011. The fact that Landsat images are free to download from USGS database is an important aspect for this diploma thesis. In contrast to other studies in this area, this diploma thesis will also use Landsat 8 Operational Land Imager (OLI) images besides of Landsat 5 Thematic Mapper (TM) and Landsat 7 Enhanced Thematic Mapper Plus (ETM+) images. The benefits of Landsat 8 will be discussed, too.

The primal task of this diploma thesis is to accurately preprocess input data and to provide a classification of several types of land cover in the Cordillera Blanca. Besides the classification of snow, rock, water and vegetation, this thesis will also contain debris-covered snow classification, which is an additional approach to monitoring glacier changes. Normalized Difference Snow Index (NDSI), Normalized Difference Vegetation Index (NDVI) and Normalized Difference Water Index (NDWI) based classifications will be used for the

classification of snow, rock, water and vegetation. For the debris-covered snow classification Paul's (2004) methodology will be used, in combination with Landsat images and Digital elevation model (DEM). In order to find the most accurate result, different threshold values will be tested for all of the above mentioned classifications.

Subsequently, snowline altitude analysis will be provided. The analysis will be based on a monography by Paterson (1994), according to which the snowline altitude for temperate glaciers roughly equals the equilibrium line altitude (ELA) at the end of the ablation season.

Slope and orientation analysis will be provided using ASTER GDEM version 2 from the year 2011. The main purpose is to determine, whether a correlation between glacier change and glacier orientation or glacier change and terrain slope exists.

Classification results will be compared with the Global Land Ice Measurements from Space (GLIMS) Glacier Database. Additionally, the results will be compared with measured field data provided by Adam Emmer, MSc. The study 'Recent evolution and degradation of the bent Jatunraju glacier (Cordillera Blanca, Peru)' (2015) is partially based on his field measurements carried out in June 2013 and May 2014. Finally, the quality and the usability of the classification algorithm will be discussed.

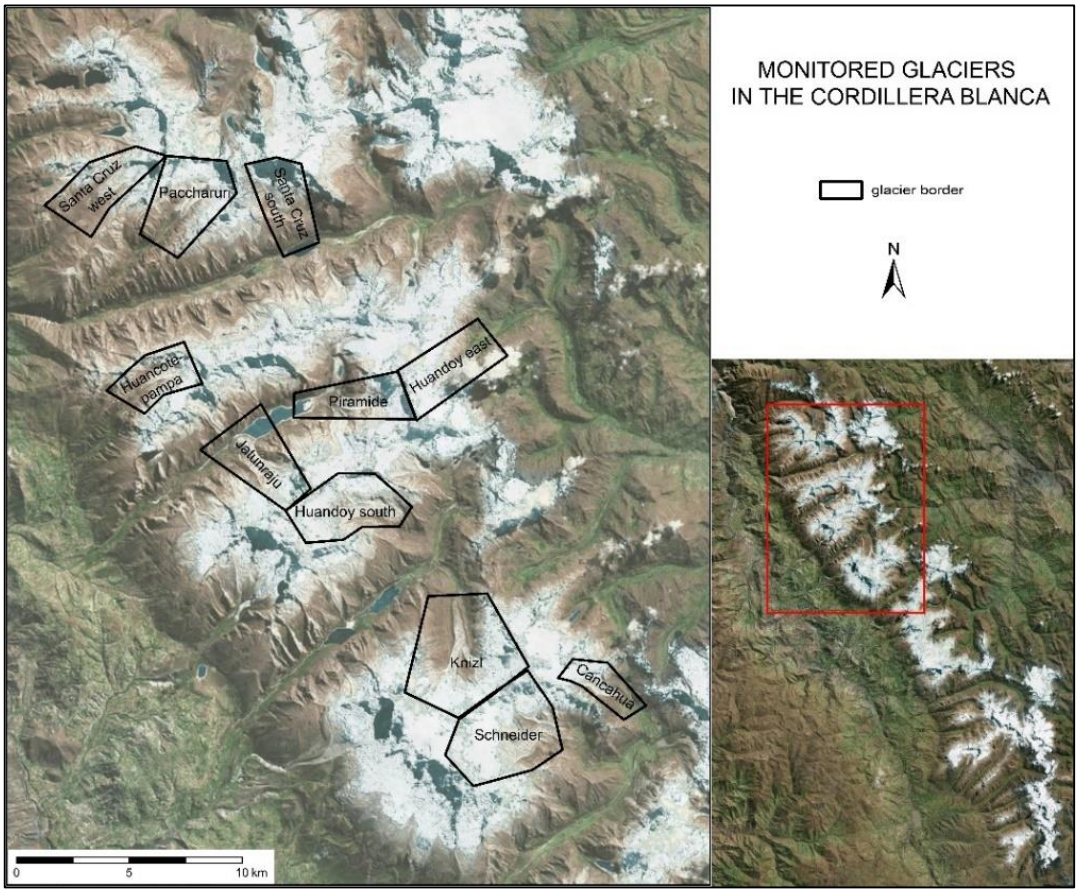

Figure 1: Monitored glaciers in the Cordillera Blanca

Eleven glaciers will be monitored in this diploma thesis: the Huancotepampa glacier, the Piramide glacier, the Jatunraju glacier, the Huandoy East glacier, the Huandoy South glacier, the Cancahua glacier, the Schneider glacier, the Knizl glacier, the Paccharuri glacier, the Santa Cruz South glacier and the Santa Cruz West glacier. The location of the monitored glaciers is presented in Figure 1.

2 LITERATURE REVIEW AND INTRODUCTION TO THE TOPIC

2.1 Brief history of the glacier research

The history of systematic glacier research on a large scale began in 1894, with the establishment of the International Glacier Commission at the 6th International Geological Congress in Zurich, Switzerland (NSIDC, 2014). Since that time glacier research has made a big progress. Glacier research was initially based on expeditions, where the researchers personally collected samples of ice, snow and rock. The maps were created by hand and were based mostly on the researchers' experience. The frequency of mapping at that time was low and the long time monitoring of glaciers was not possible. Because the highest mountains were dangerous to reach, only the lower and easily accessible mountain ranges were mapped. The first expedition in the Cordillera Blanca was realized by the Deutsch- Österreichischer Alpenverein in the 30s of the 20th century. The result of the expedition was a topographic map at a scale of 1:100.000, which was based on terrestrial photogrammetry (Hastenrath and Ames, 1995).

The introduction of a more effective method – aerial photogrammetry – in the 30s of the 20th century was the following milestone of glacier research. Aerial photogrammetry enabled reduction of research costs and increased the frequency of glacier research. However, the results were still based mostly on the researchers' experience and regular glacier monitoring was still not possible. Unfortunately, the highest peaks of the mountain ranges were still not accessible by this technology.

Glacier research has radically changed since the middle of the 20th century as the result of the rapid progress of computer sciences. At that time the world witnessed the birth of a new study field – remote sensing. Remote sensing is now commonly used to describe the science — and art— of identifying, observing, and measuring an object without coming into direct contact with it (NASA, 2015). Nowadays, remote sensing and cosmology enable us to make land cover analyses faster, cheaper and thus more efficient. The collected data are almost instantly available and in some cases for free. The highest peaks of the mountain ranges are visible for satellites and so monitoring glacier changes is easier, than ever before.

2.2 Mapping land cover with remote sensing

Unless it has a temperature of absolute zero (-273,15 °C), an object reflects, absorbs, and emits energy in a unique way, and at all times. This energy, called electromagnetic radiation, is emitted in waves that are able to transmit energy from one place to another (NASA, 2015). Remote sensing is based on the measurement of reflected or emitted radiation from different bodies. Objects having different surface features reflect or absorb the Sun's radiation in different

ways. The reflectance properties of an object depend on the particular material and its physical and chemical state, the surface roughness, as well as the geometric circumstances (Seos Project, 2015). These differences make it possible to identify different Earth surface features or materials by analyzing their spectral reflectance patterns or spectral signatures. These signatures can be visualized in so called spectral reflectance curves as a function of wavelengths (Seos Project, 2015).

2.2.1 Spectral properties of glacier's land cover

Ice, snow and rock the glaciers contain, have unique reflectance properties and unique spectral reflectance curves. The main purpose of the basic classification task is to find the wavelength or the combination of wavelengths (i.e. indexes, ratios) in order to separate different types of land cover with a given probability. There are certain general rules and properties of snow, water, rock and vegetation that are demonstrated in Figure 2. These rules as briefly discussed in the below paragraph can also be found in different sources of literature.

Ice and snow generally show a high degree of reflection at visible wavelengths (VIS; ca 0,4 – 0,75 μm), lower reflection in the NIR (Near InfraRed, wavelength ca 0,78 - 0,90 μm) and very low reflection in the SWIR (ShortWave InfraRed, wavelength ca 1,57 - 1,78 μm). The low reflection of ice and snow in the SWIR is related to their microscopic liquid water content (ESA, 2015). The water curve is characterized by a high absorption at near infrared wavelengths range and beyond (Seos Project, 2015). The spectral reflectance curve of the vegetation has a significant minimum of reflectance in the visible portion of the electromagnetic spectrum resulting from the pigments in plant leaves. Reflectance increases dramatically in the near infrared (Seos Project, 2015). The spectral reflectance curve of bare soil is considerably less variable. The reflectance curve is affected by moisture content, soil texture, surface roughness, presence of iron oxide and organic matter. These factors are less dominant than the absorbance features observed in vegetation reflectance spectra (Seos Project, 2015). Considering that these rules and properties vary according to different conditions and in different locations on Earth, each classification should start with reflectance analysis in order to avoid misclassification and inaccurate results.

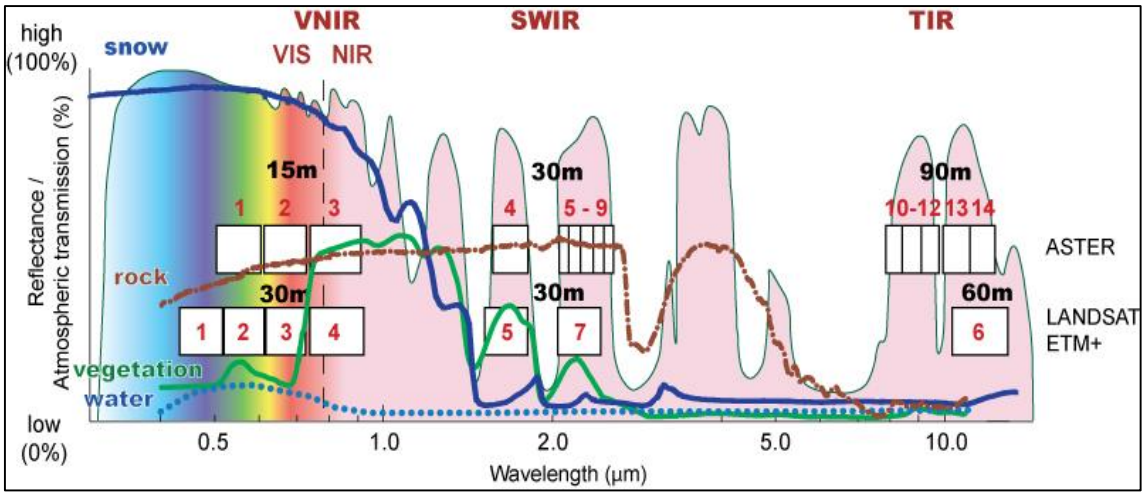

Figure 2: Spectral reflectance curve of snow, rock, vegetation and water (ESA, 2015)

2.2.2 Band ratios and indexes

Modern satellite sensors can measure electromagnetic reflectance of land cover in different spectral intervals, also known as bands. Usually the values measured in particular bands are not used separately. The classifications are mostly based on different combinations of values measured in particular spectral intervals. These combinations can be either simple ratios of two bands or more complicated and specific indexes, e.g. NDVI, NDSI or NDWI.

Band ratios are simple ratios of the electromagnetic reflectance values measured in two bands. Band ratios are used to separate two or more land cover types that are fairly spectrally different. For example Figure 2 shows that the electromagnetic reflectance of vegetation steeply increases between bands 3 and 4 (for Landsat ETM+), whereas the electromagnetic reflectance of water slightly decreases in the same spectral interval. This means that the value of band ratio (Band 4 / Band 3) will be positive for vegetation and slightly negative for water. On the basis of this difference a threshold value can be determined to manually or automatically separate vegetation and water.

Compared to band ratios, band indexes are more complex mathematical expressions. Each band index is defined to easily separate specific types of land cover from the rest of the classification classes. In this diploma thesis the Normalized Difference Snow Index (NDSI), the Normalized Difference Vegetation Index (NDVI) and the Normalized Difference Water Index (NDWI) will be used to separate and classify different types of land covers in the Cordillera Blanca.

2.2.2.1 Normalized Difference Vegetation Index (NDVI)

Nearly all satellite vegetation indexes use the NDVI formula to quantify the density of plant growth on the Earth — near-infrared radiation (NIR) minus visible radiation (VIS) divided by near-infrared radiation (NIR) plus visible radiation (VIS). Visible radiation (VIS) is usually replaced by the red band radiation (R). Written mathematically, the NDVI formula is:

$$NDVI = (NIR — R) / (NIR + R)$$

Calculations of NDVI for a given pixel always result in a number that ranges from minus one (-1) to plus one (+1). A zero means no vegetation and close to +1 (0,8 – 0,9) indicates the highest possible density of green leaves (NASA, 2015).

Figure 3 shows an example of NDVI calculation as a tool for separating healthy and unhealthy vegetation.

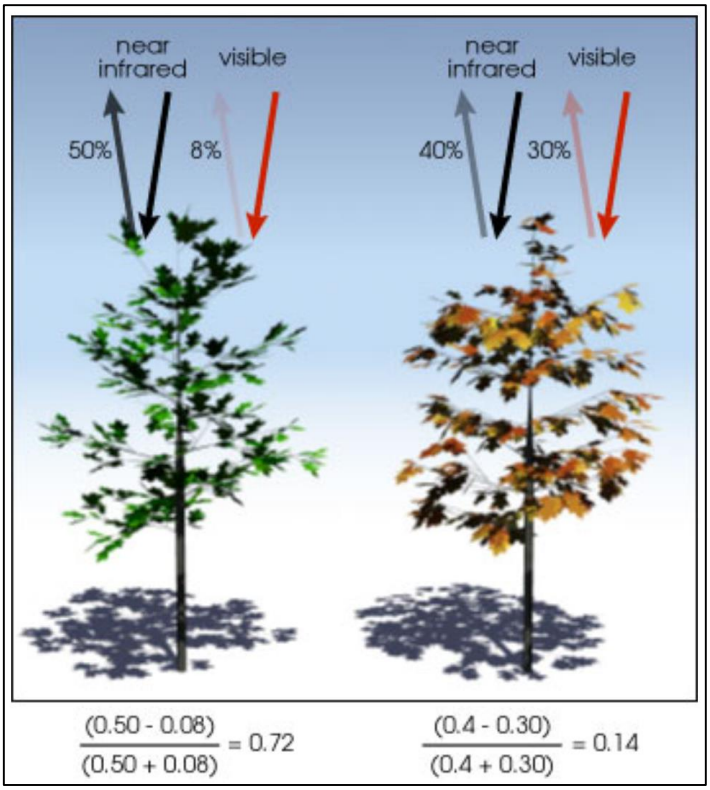

Figure 3: Calculating Normalized Difference Vegetation Index for healthy and unhealthy vegetation (NASA, 2015)

Healthy vegetation (on the left) absorbs most of the visible light that hits it, and reflects a large portion of the near-infrared light. On the other hand, unhealthy or sparse vegetation (on the right) reflects more visible light and less near-infrared light. (NASA, 2015).

2.2.2.2 Normalized Difference Water Index (NDWI)

The Normalized Difference Water Index formula shows the moisture content in soil and vegetation and usually is used to clearly separate and visualize open water areas. NDWI formula equals short-wavelength infrared radiation (SWIR) minus near-infrared radiation (NIR) divided by short-wavelength infrared radiation (SWIR) plus near-infrared radiation (NIR). In some cases, when the SWIR band is not available, the green band (G) can be used. Written mathematically, the NDWI formula is:

$$NDWI = (SWIR — NIR) / (SWIR + NIR)$$

or

$$NDWI = (G — NIR) / (G + NIR)$$

NDWI is useful to assess water content in a normalized way. This index increases with vegetation water content or from dry soil to free water. The SWIR reflectance indicates changes in soil and vegetation water content, while the NIR reflectance is affected by internal structure of leaf and soil but not by water content directly. The combination of the NIR with the SWIR removes variations induced by internal structure of leaf and soil, thus improving the accuracy in retrieving the vegetation and soil water content (Ceccato, et al., 2001). The calculation has a result between minus one (-1) and plus one (1), where the positive values are typical for open water areas; while the negative values are typical for non-water features.

2.2.2.3 Normalized Difference Snow Index (NDSI)

The NDSI formula is used to monitor the extent of snow cover. At visible wavelengths (e.g. 0,66 microns), snow cover is just as bright as clouds, and is therefore difficult to distinguish from cloud cover. However, at 1,6 microns, snow cover absorbs sunlight, and therefore appears much darker than clouds. This allows the effective discrimination between snow cover and clouds. Values of NDSI < 0,4 typically indicate the presence of snow (Ackerman, 2004). NDSI formula equals green band radiation (G) minus short-wavelength infrared radiation (SWIR) divided by green band radiation (G) plus short-wavelength infrared radiation (SWIR). Written mathematically:

$$NDSI = (G — SWIR) / (G + SWIR)$$

As in the case of NDVI and NDWI, the calculated values of NDSI range from minus one (-1) to plus one (1). The higher positive value, the higher the probability of snow cover.

2.2.3 Classification

Digital image classification is the process of representing pixels as a land cover feature. Pixels are the smallest units represented in an image. Image classification uses the reflectance statistics for individual pixels. Classification methods can be divided into 3 main groups:

- Unsupervised image classification
- Supervised classification
- Object-based classification

One of the main goals of this diploma thesis is to create a semi-automatic classification algorithm, which can classify predefined types of land cover in the Cordillera Blanca. It is enough to analyze input data from one year, as the unified character of data allows us to use the tested threshold values for the remaining years. The reason for this is, that Landsat CDR scenes are equally preprocessed. This issue will be discussed in detail in chapter 3.1. For this purpose, unsupervised classification methods are suitable, where pixels are grouped on the basis of their reflectance properties. These groups are called 'clusters'. The user identifies the number of clusters to generate and the bands to use. The image classification software then generates clusters based on this input information. The user manually assigns the appropriate land cover class to each cluster. It often happens, that different clusters represent the same land cover class. In such a case the user merges the clusters into one land cover type.

In this diploma thesis ISODATA and K-means classification will be used from among many different unsupervised classification methods.

2.2.3.1 ISODATA and K-means classifications

ISODATA and K-means classification algorithms are iterative procedures. In general, both of them assign first an arbitrary initial cluster vector. The second step classifies each pixel to the closest cluster. In the third step the new cluster mean vectors are calculated based on all the pixels in one cluster. The second and third steps are repeated until the 'change' between the iteration is small. The 'change' can be defined in several different ways, either by measuring the distances the mean cluster vector have changed from one iteration to another or by the percentage of pixels that have changed between iterations (Yale Center for Earth Observation (YCEO), 2015). Figure 4 describes the ISODATA clustering algorithm scheme.

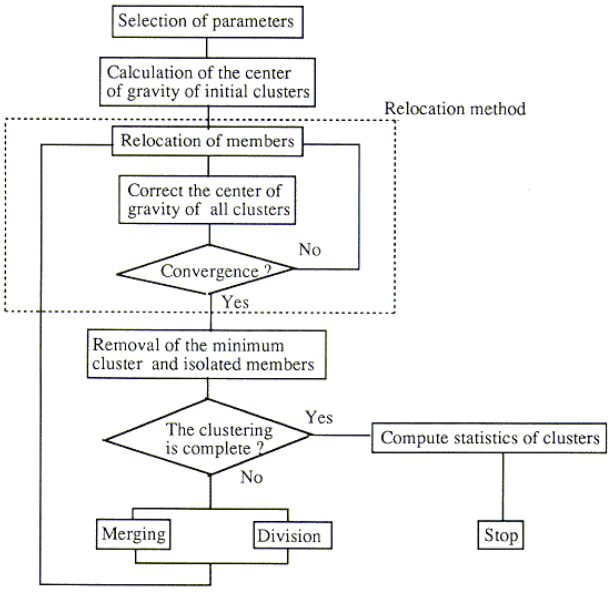

Figure 4: ISODATA clustering algorithm (Japan Association of Remote Sensing, 2015)

The ISODATA algorithm has some further refinements. Clusters are merged if either the number of members (pixels) in a cluster is less than a certain threshold or if the centers of two clusters are closer than a certain threshold. Clusters are split into two different clusters if the cluster standard deviation exceeds a predefined value and the number of members (pixels) is twice the threshold for the minimum number of members (YCEO, 2015).

The main difference between the ISODATA and the K-means algorithm is, that while ISODATA requires only a predefined range of the number of clusters, K-means requires an exact number of final clusters. In K-means algorithm, the main goal is to minimalize the variability inside clusters – to minimalize the sums of square distances between each pixel and its assigned cluster center:

$$SS_{dist.} = \sum_{\forall x}[x - C(x)]^2 ,$$

where C(x) is the center of the cluster, in which x is.

To minimalize the sums of square distances function Mean Squared Error (MSE) is used:

$$MSE = \frac{\sum_{\forall x}[x-C(x)]^2}{(N-c)\times b} = \frac{SS_{dist.}}{(N-c)\times b} ,$$

where N is the number of pixels, c is the number of clusters and b is the number of spectral bands.

Input values and threshold have to be chosen with distinctive attention, as both K-means and ISODATA are extremely sensitive to input values and thresholds.

2.2.4 Analyses workflow to classify glacier land cover

Nowadays both researches and the general public are more aware of climate change, as it determines our present and future. The phenomenon of glacier change is tightly connected to the climate change. This is probably one of the reasons for numerous studies on this topic. Many aspects of glacier analyses are common on every part of the Earth, but also there are certain methods, which are unique for a specific mountain range or glacier. Although thresholds and detailed steps differ for each mountain range or glacier, it is always helpful to be aware of existing studies. In the next part of this diploma thesis ideas and steps serving as its basis will be presented.

Manual delineation, or hand-digitization, of remotely sensed images had been considered the most accurate method for mapping glaciers (Albert, 2002, Cit. In Burns and Nolin, 2014). The limitation of this method is, that it is very time-consuming for a multitemporal change analysis of a large area, such as an entire mountain range. Automated glacier mapping methods using various band ratios have been applied to map glaciers at local to regional scales because these methods are easier to implement, frequently just as precise as manual digitization (Paul et al., 2013, Cit. In Burns and Nolin, 2014), and provide more consistent results.

One of the many studies about glacier area change and snowline altitude change was conducted by Heiskanen et al. (2003). Figure 5 demonstrates the algorithm described in the study 'Mapping glacier changes, snowline altitude and AAR using Landsat data in Svartisen, Northern Norway'.

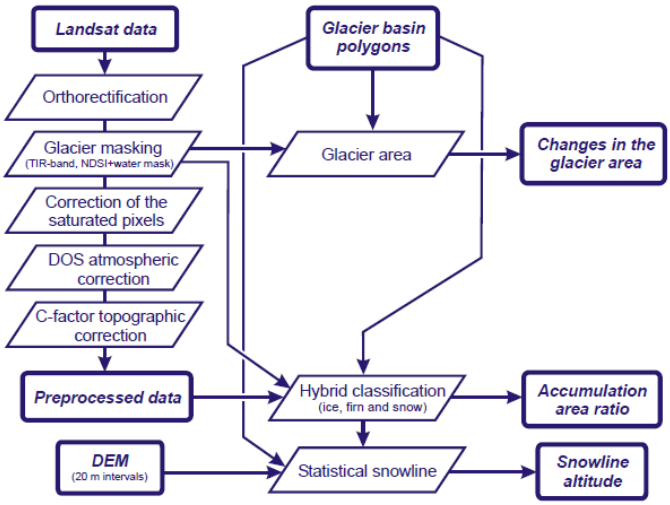

Figure 5: Heiskanen's workflow (Heiskanen et al., 2003)

Heiskanen's analysis was based on Landsat images in 4 years and a 25 m resolution DEM. The first part of the study consisted of the Landsat image preprocessing, which contained atmospheric and topographic corrections. Following the preprocessing, glacier pixels were

classified into ice, firn and snow. A hybrid approach of the unsupervised and supervised classification methods was applied. The training areas were clustered using ISODATA classifier and clusters were visually interpreted into one of the tree classes. The interpreted clusters were then used to derive the features of the various glacier zones, and to complete the supervised maximum likelihood classification for the whole study area. Finally, the snowline altitude was calculated using the statistical methodology of Seidel et al. (1997). According to the definition, the snowline altitude is the altitude of the lowest elevation interval in which the snow coverage is over 50 percent.

Hendriks and Pellikka (2007) developed a semi-automatic two stepped method for glacier masking. In the first step, NDWI was computed and applied for the images. After analyzing the created NDWI images the upper 20–30 % of the pixel values in each image was recognized as water. The second part of the model creates the glacier mask. It uses the NDSI, saturated pixels, the water mask and Landsat 7 ETM+ band 5 within a set of conditional operators. The NDSI is often used for discrimination between snow, soil, rocks and cloud cover (Silverio and Jaquet, 2005, Cit. In Hendriks and Pellikka, 2007). Whenever the NDSI is calculated, the threshold is found by visually investigating the image and sampling NDSI values. Typical NDSI values for Landsat images range between 0,5 and 0,7 and differ for almost any image due to illumination differences. According to Hendriks and Pellikka (2007), this is not practical when dealing with a large set of images in monitoring studies. Band 5 of the Landsat 7 ETM+ sensor is frequently used to detect cloud cover (Choi and Bindschadler, 2004, Cit. In Hendriks and Pellikka, 2007). In this case the model uses band 5 to remove potential clouds from the images. At the final stage of the computation a contiguity analysis is completed. Figure 6 shows the workflow of Hendriks and Pellikka.

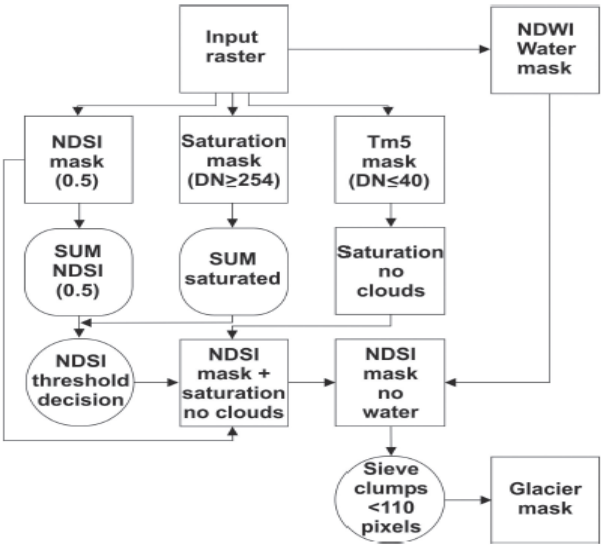

Figure 6: Hendriks and Pellikka's workflow (Hendriks and Pellikka, 2007)

2.2.4.1 Debris-covered snow classification

One of the central goals of this diploma thesis is to develop automatic classification of debris-covered snow. Burns and Nolin (2014) in the summary of his study indicates that future studies should explore new methods to provide for accurate mapping of debris-covered glaciers in the Cordillera Blanca region, as their true extent and role in the water balance are not well known. Mapping debris-covered snow is not a trivial process. The main reason for this is, that the spectral properties of debris-covered snow are very similar to the spectral properties of rocks. One of the methods for eliminating this problem is created by Paul et al. (2004). Numerous studies, e.g. Shukla et al. (2010), Bhardwaj et al. (2014) or Karimi et al. (2012) refer to Paul's method.

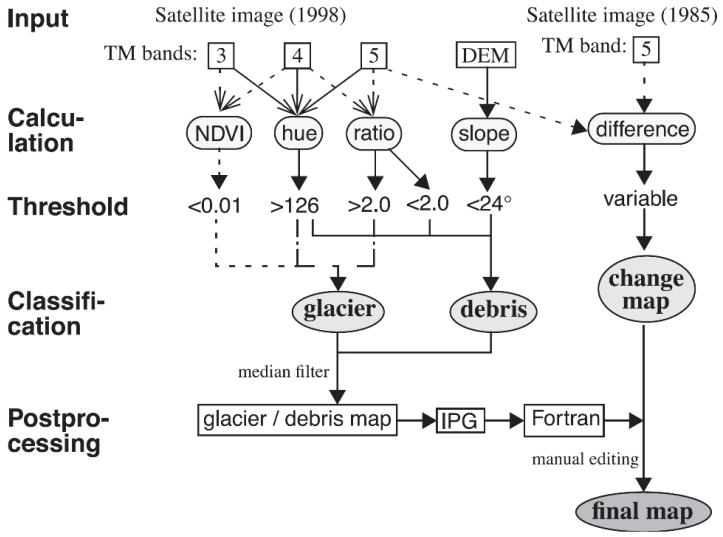

Figure 7: Paul's workflow for debris-covered snow separation (Paul et al., 2004)

Generally, the methods used by Paul for glacier classification are the same as the ones used in other glacier studies. He uses both spectral band index (NDVI) and spectral band ratio (TM5/TM4), as represented in Figure 7. The main benefit of Paul's work is the separation of debris-covered snow using Landsat images and digital elevation model.

In general, the supraglacial debris originates from the surrounding ice free rock walls, which are prone to intense weathering (Maisch et al., 1999, Cit. In Paul et al., 2004). The debris is transported by the down-slope movement of a glacier towards the terminus and is deposited in the glacier forefield. If the local surface slope is too high, debris usually slides farther down until a less steep slope allows accumulation. The high spatial heterogeneity of the debris cover causes that the optical satellite imagery contains numerous mixed pixels (ice/debris). The ice cannot be detected by multispectral classification, if the debris properties dominate in the pixel. As the glacier boundary shows differences in illumination caused by its shape, manual delineation is still possible. However, it sometimes happens, that the boundary between debris and stagnant ice

cannot be delineated even through on site observations. Paul's approach combines the advantages of multispectral remote sensing (mapping of clean ice and vegetation free regions) and DEM-derived slope facet (range from 0° to 24). This combination allows us to exclude most of the vegetation and ice free, steep mountain flanks. They will still remain, if their slope is less than 24°. As the debris-covered glacier ice has to be contiguous with clean glacier ice, a neighborhood-analysis is performed to exclude all remaining areas that are not connected to clean glacier ice.

2.3 Medium resolution satellite images

Remote sensing images acquired from different platforms (satellite, aircraft) using sensors that operate in different spectral regions (visible, infrared, microwave) have been widely used to study glaciers, e.g. to measure ice thickness, surface ice velocities, and changes in surface elevation over time (University of Alaska, 2014). The incorporation of satellite-based data can greatly augment traditional ground-based glacier monitoring studies.

In the past three decades several polar orbiting Earth Observing Satellites have provided a temporal archive of medium resolution images (spatial resolution ranging from 5 m to 60 m). The following table contains the most important satellites and their corresponding sensors that possess great potential for glacier monitoring (University of Alaska, 2014):

Table 1: Important satellites for glacier monitoring (University of Alaska, 2014, with the author's amendments)

Satellite	**Sensor**	**Wavelengths**	**Spatial Resolution**	**Glaciological application**
Landsat	TM ETM OLI/TIRS	Visible, Infrared	15 m - 30 m	Terminus and area mapping; spectral characteristics of snow and ice
Terra	ASTER	Visible, Infrared	15 m - 30 m	Terminus and area mapping; DEM for elevation change monitoring.
SPOT	Pan XS	Visible, NIR	5 m - 20 m	Terminus and area mapping
IRS	Pan LISS	Visible, NIR	5 m - 72 m	Terminus and area mapping
ERS	SAR	Microwave	30 m	Terminus and area mapping; surface velocity estimation; monitoring elevation change
Radarsat	SAR	Microwave	8 m - 100 m	Terminus and area mapping; surface velocity estimation; monitoring elevation change

Although medium resolution satellite images do not constitute high quality data and thus are not the perfect input to detect detailed changes in the land cover, these data are easily accessible. Free data, such as Landsat, ASTER or SPOT data, thus remain the main sources for

educational purposes. On the contrary, high resolution, but expensive satellite images are rather suitable for government and business purposes.

2.3.1 The Landsat program

The main data sources for the purposes of this diploma thesis are Landsat satellite images. Landsat data are free to download via U.S. Geological Survey (USGS) website.

In 1965, William Pecora, the director of the U.S. Geological Survey (USGS) suggested launching a remote sensing satellite program to gather facts about the natural resources of the Earth. While weather satellites had been monitoring the Earth's atmosphere since 1960, terrain data from space were not acknowledged until the mid-1960s. Landsat 1, the first Landsat program satellite, was launched in 1972. At that time the satellite was known as the Earth Resources Technology Satellite (ERTS). It was the first satellite observing the Earth, which was launched with the explicit intent of monitoring its landmasses (NASA, 2015). Since then, altogether 8 Landsat satellites have been launched. Figure 8 illustrates the Landsat program timeline from 1972 to 2023, when Landsat 9 is planned to be launched.

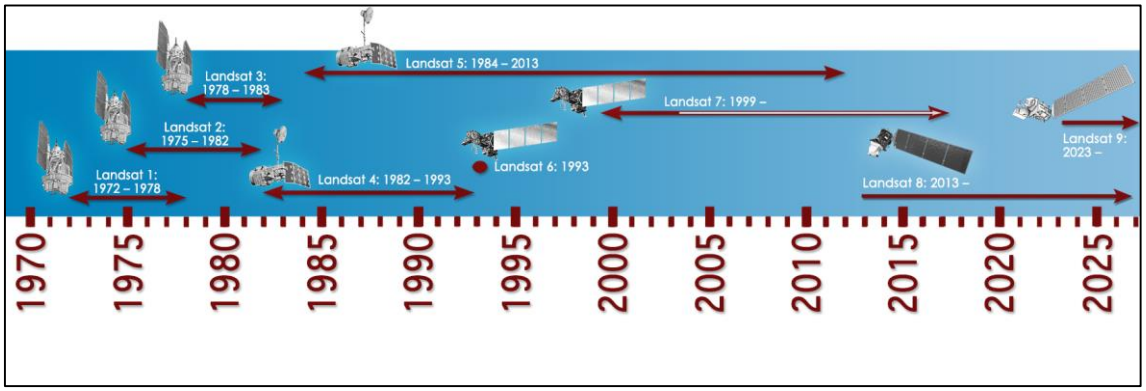

Figure 8: Landsat timeline from 1972 to 2023 (NASA, 2015)

In this diploma thesis mostly Landsat 5, 7 and 8 images are used. The main reason for this is, that Landsat 1-3 images do not have the correct sensor properties for glacier monitoring and that only one Landsat 4 image from 1989 fulfilled the designated criteria.

Landsat 8 launched on February 11, 2013, from Vandenberg Air Force Base, California, on an Atlas-V 401 rocket, with the extended payload fairing (EPF) from United Launch Alliance, LLC. The Landsat 8 satellite payload consists of two science instruments – the Operational Land Imager (OLI) and the Thermal Infrared Sensor (TIRS). These two sensors provide seasonal coverage of the global landmass at a spatial resolution of 30 meters (visible, NIR, SWIR); 100 meters (thermal); and 15 meters (panchromatic) (NASA, 2015). Figure 9 demonstrates the

Landsat 8 OLI and TIRS spectral bands as opposed to Landsat 7 ETM+ bands. OLI provides two new spectral bands, one designed especially for detecting cirrus clouds and the other for coastal zone observations.

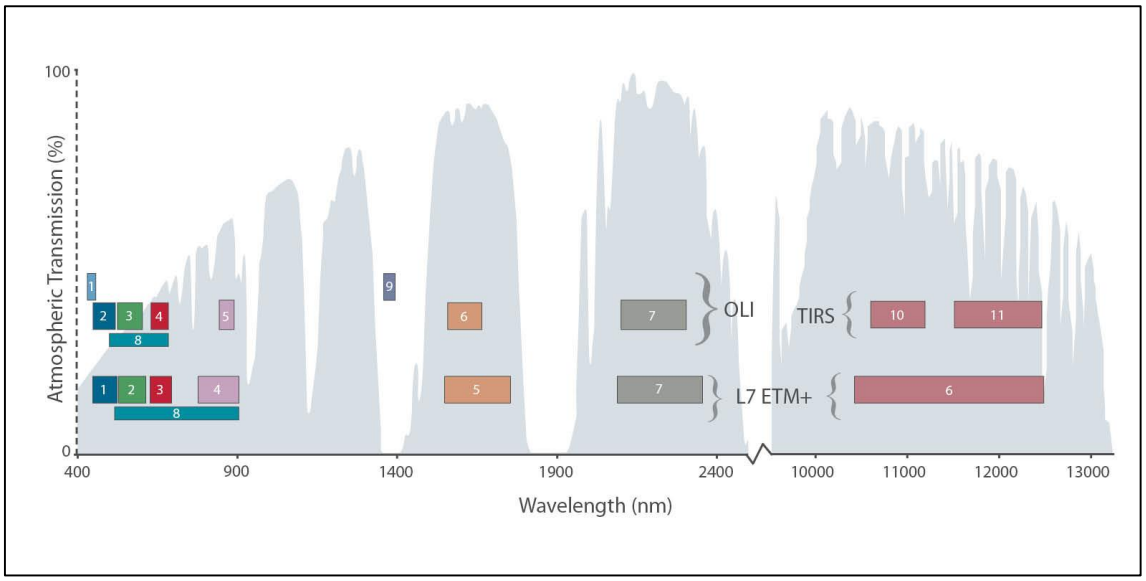

Figure 9: Comparison of Landsat 7 ETM+ and Landsat 8 OLI/TIRS spectral bands (USGS, 2015)

One of the initial hypothesis for this diploma thesis is, that Landsat 8 sensors can add to the quality and accuracy of glacier monitoring. This matter will be further discussed in the following chapters.

2.4 Study area – the Cordillera Blanca, Peru

The tropical Cordillera Blanca is the largest glacierized area in the tropics. It stretches 130 km from 8°30' to 10° S and reaches 6000 m a.s.l. at several summits. The highest mountain is Nevado Huascarán Sur at 6768 m a.s.l (Kaser and Georges, 1997). Almost the entire range of the Cordillera Blanca is encompassed by the Huascarán National Park, which was established in 1975. Figure 10 illustrates the position of the Cordillera Blanca in Peru. The snow and ice cover of the Cordillera Blanca are essential for the inhabitants of Peru, especially for people living in the nearest villages and towns (e.g. Huaraz). They serve as the main source of drinking water and are important for agricultural purposes. Last, but not least, their waterpower potential is extremely high.

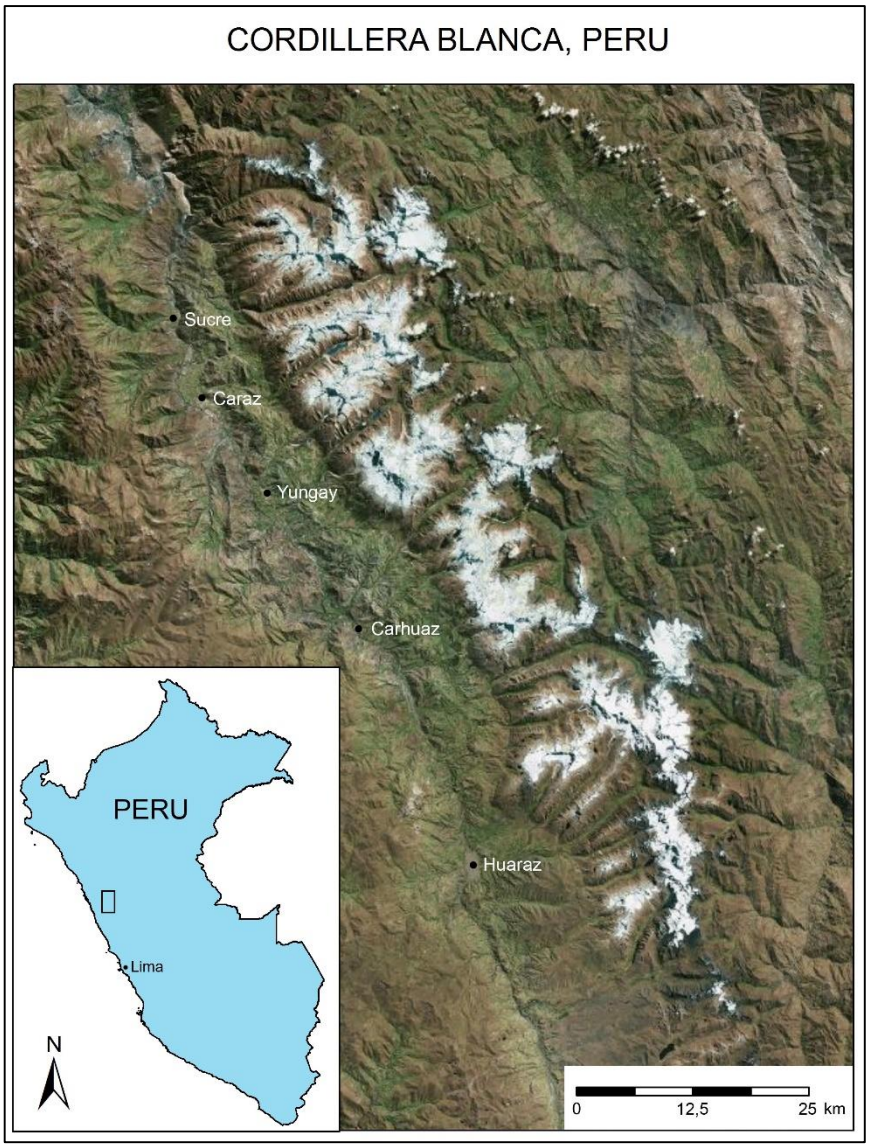

Figure 10: Study Area – The Cordillera Blanca, Peru

2.4.1 Climate of the Cordillera Blanca

The climate in the tropical Cordillera Blanca has some basic characteristics. A pronounced seasonal distinction in precipitation and a lack of seasonal temperature variation are the most important defining features of the climate in this region.

There is a large seasonal distinction in the precipitation totals for the wet (October – April) and dry (May – September) seasons (Burns and Nolin, 2014). The wet season brings 70 – 80% of the annual precipitation (Johnson, 1976, Cit. In Kaser and Georges, 1997). In terms of temperature, the difference between wet season average temperature and dry season average temperature is much smaller than the average diurnal temperature range (Kaser et al., 1990, Cit. In Burns and Nolin, 2014). The hydrometric seasonality is caused by the oscillation of the intertropical convergence zone. As is typical for the tropics, the precipitation processes are

characterized by the combination of a large-scale advection of humid air from the east (i.e. the Amazon river basin) and locally induced convective cells. The Cordillera Blanca is, in any case, a significant barrier in the easterly-southeasterly atmospheric circulation of tropical South America. (Kaser and Georges, 1997). As on all Peruvian cordilleras, the glaciers on the eastern slopes of the Cordillera Blanca extend to generally lower elevations than those on the western slopes (Kaser and Georges, 1997). Assessing the correlation between glacier orientation and glacier change on one hand and glacier slope and glacier change on the other will be part of this diploma thesis.

2.4.2 Former glacier research in the Cordillera Blanca

Considering the effect of the local and global climate change on the Cordillera Blanca glaciers, several studies dealing with past, present and future changes have been conducted. Some of the studies focus on climate characteristics and glacial processes (Kaser, 1999; Licciardi et al., 2009; Vuille et al., 2008; Mark, 2002; Hall et al., 2009; Schauwecker et al., 2014; Solomina et al., 2007), others aim attention at mapping glacier change using different remote sensing methods (Burns and Nolin, 2014; Hastenrath and Ames, 1995; Kaser and Georges, 1997; McFadden et al., 2011; Racoviteanu et al., 2008). There are two projects, which can be used to verify the results of this diploma thesis: 'Global Land Ice Measurements from Space (GLIMS)' and 'Recent evolution and degradation of the bent Jatunraju glacier (Cordillera Blanca, Peru)' by Emmer et al. (2015).

2.4.2.1 GLIMS Glacier Database

Global Land Ice Measurements from Space (GLIMS) is an international project. Its aim is to examine the majority of the world's estimated 160,000 glaciers. GLIMS uses data collected mainly by the Advanced Spaceborne Thermal Emission and Reflection Radiometer (ASTER) instrument aboard the Terra satellite and the LANDSAT Enhanced Thematic Mapper Plus (ETM+), along with historical observations. The GLIMS project is currently establishing a unique glacier inventory for storing information about the extent and rates of change of all the world's glacial resources. GLIMS consists of many institutions called Regional Centers. Each Regional Center conducts glacier analysis for its particular region. Based on these analyses, the GLIMS Glacier Database provides students, educators, researchers and the general public with reliable glacier data. The database is being continually updated with new glacier data (National Snow & Ice Data Center, 2015). Figure 11 shows Cordillera Blanca using the GLIMS Glacier Browser. The browser contains different glacier properties, which are easy to download.

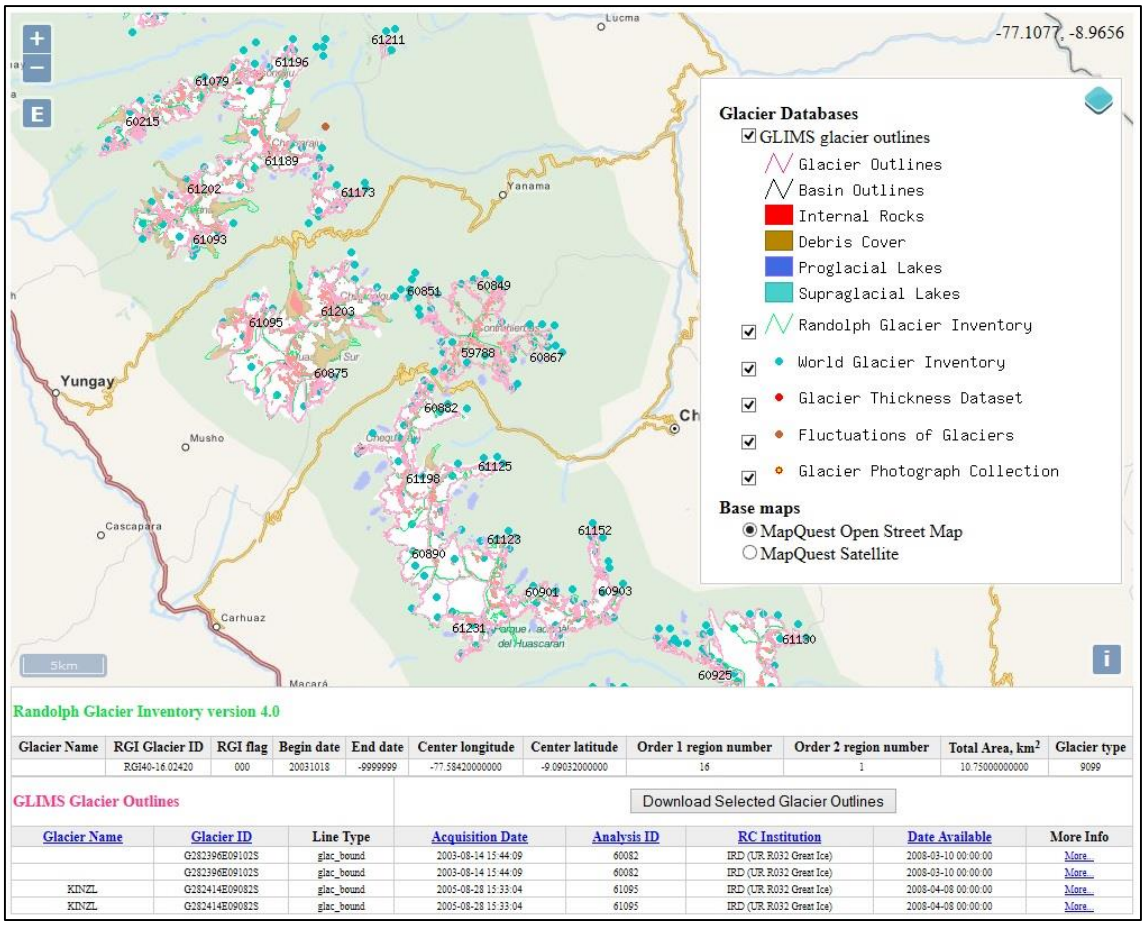

Glacier Name	RGI Glacier ID	RGI flag	Begin date	End date	Center longitude	Center latitude	Order 1 region number	Order 2 region number	Total Area, km²	Glacier type
	RGI40-16.02420	000	20031018	-9999999	-77.58420000000	-9.09032000000	16	1	10.75000000000	9099

Glacier Name	Glacier ID	Line Type	Acquisition Date	Analysis ID	RC Institution	Date Available	More Info
	G282396E09102S	glac_bound	2003-08-14 15:44:09	60082	IRD (UR R032 Great Ice)	2008-03-10 00:00:00	More...
	G282396E09102S	glac_bound	2003-08-14 15:44:09	60082	IRD (UR R032 Great Ice)	2008-03-10 00:00:00	More...
KINZL	G282414E09082S	glac_bound	2005-08-28 15:33:04	61095	IRD (UR R032 Great Ice)	2008-04-08 00:00:00	More...
KINZL	G282414E09082S	glac_bound	2005-08-28 15:33:04	61095	IRD (UR R032 Great Ice)	2008-04-08 00:00:00	More...

Figure 11: Cordillera Blanca in the GLIMS Glacier Database (GLIMS Glacier Browser, 2015)

2.4.2.2 Recent evolution and degradation of the bent Jatunraju glacier (Cordillera Blanca, Peru)

The main object of the study 'Recent evolution and degradation of the bent Jatunraju glacier (Cordillera Blanca, Peru)' by Emmer et al. (2015) is the Jatunraju glacier in the Cordillera Blanca region. Adam Emmer, MSc. is a researcher at the Department of Physical Geography and Geoecology, Faculty of Science of the Charles University in Prague. This study is based on topographical maps, aerial photos and satellite images covering a period of 66 years and a field survey performed in June 2013 and May 2014. Historical geodetic measurements (1967–1968; 1977–1984) and current Landsat images (2001–2013) were used by estimating surface velocities and changes in surface velocities over time. Although the above mentioned study focused only on the Jatunraju glacier located in the northern part of the Cordillera Blanca, the presented data and results may serve as a potential source of verification for the purposes of this diploma thesis. Figure 12 shows the geomorphic map of the Jatunraju glacier based on Emmer's field survey from June 2013 and May 2014.

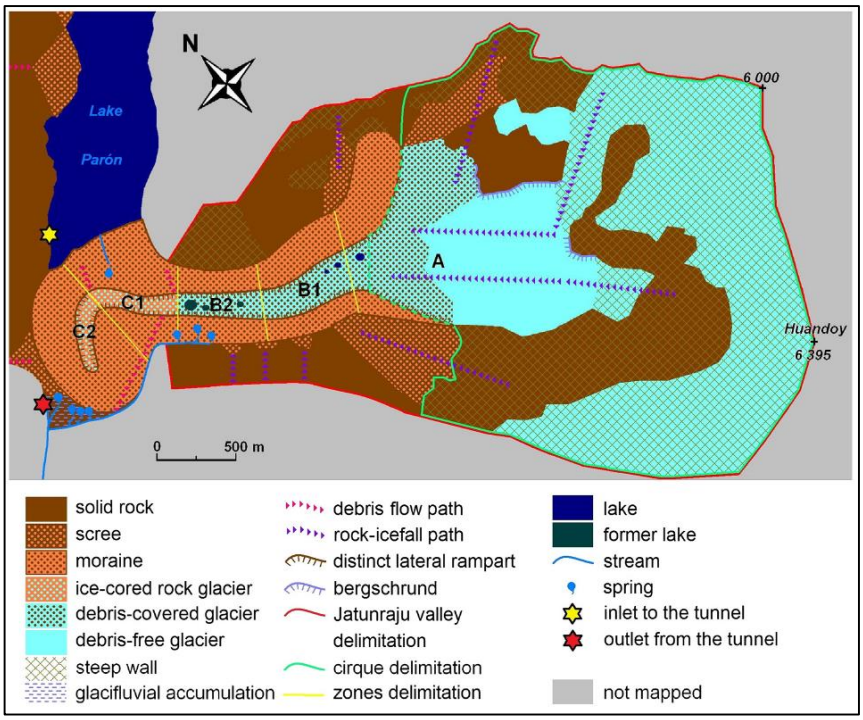

Figure 12: Geomorphic map of the Jatunraju glacier, valley, and close surroundings based on the field survey performed in June 2013 and May 2014 (Emmer et al., 2015)

3 DATA AND METHODOLOGY

In the first part of this chapter the main characteristics of Landsat and ASTER GDEM data will be discussed, as these two digital data sets are the main sources for the analyses conducted in this diploma thesis. It is important to know the scope and limitations of input data in order to find the most precise results and enable their critical assessment. In the second part data preprocessing techniques and their usage will be explained. In the third part the process of creating the classification algorithm will be introduced. Finally, in the last part of this chapter the algorithm for snowline detection, as well as the technique of assessing the impact of slope and aspect on snowline altitude change will be described.

3.1 Landsat data

Landsat data constitute the main data source for this diploma thesis, primarily on the grounds of their quality and financial benefits. Their long term availability is also a big advantage. Although Landsat digital satellite images in the Cordillera Blanca region are available as of 1973, only data as of 1987 meet the quality standards for measuring glacier changes. This enables us to study glacier changes in the Cordillera Blanca based on consistent data quality over the period of almost 28 years. As emphasized in the previous chapter, Landsat digital images have medium resolution (30 m) and thus contain enough information for data analyses for the purposes of this diploma thesis.

Following the registration to the online database, Landsat data are free to download via USGS Earth Explorer website (http://earthexplorer.usgs.gov/). After logging in, the appropriate location by address/place, path/row, feature or circle needs to be selected in the Earth Explorer interface. In this regards, the Cordillera Blanca, as a major geographic location, is easy to search for (Cordillera Blanca, Huascarán National Park, Peru; Latitude -9,2458; Longitude -77,5347; Path 8; Row 66). As regards the date range, it is always practical to select the longest possible time period, i.e. from 1972 (launching the Landsat program) to the present. One of the most useful tools of the Earth Explorer interface is, that the user can select only certain months he/she wishes to search for. As discussed in the previous chapter, the Cordillera Blanca has wet and dry seasonality. It is therefore important to choose scenes from the same season across the years. For the purposes of monitoring glacier changes this is usually the end of the dry season (July, August and September). This guarantees that the snow cover is the smallest in a given year. The repeat cycle for Landsat 5 and 7 is 16 days. This means that only 5-6 scenes are taken during these three months.

In the next step the required data sets need to be selected in Earth Explorer. The USGS archive contains both regular Landsat Archive Products and Landsat Surface Reflectance High Level Data Products (Climate Data Records - CDR). In the early process of data acquisition, Landsat Archive Products were downloaded. However, during preprocessing it was discovered, that it is impossible to provide correct atmospheric corrections without precise meteorological and atmospheric information for each downloaded data set. On the other hand, Landsat CDR scenes are generally atmospherically corrected. For Landsat 4-5 Thematic Mapper (TM) or Landsat 7 Enhanced Thematic Mapper Plus (ETM+) data, Surface Reflectance data are generated from the Landsat Ecosystem Disturbance Adaptive Processing System (LEDAPS), a specialized software originally developed through a National Aeronautics and Space Administration (NASA) Making Earth System Data Records for Use in Research Environments (MEaSUREs) grant by NASA Goddard Space Flight Center (GSFC) and the University of Maryland (Masek et al., 2006, Cit. In USGS, 2015). The software applies Moderate Resolution Imaging Spectroradiometer (MODIS) atmospheric correction routines to Level-1 data products. Water vapor, ozone, geopotential height, aerosol optical thickness, and digital elevation are input with Landsat data to the Second Simulation of a Satellite Signal in the Solar Spectrum (6S) radiative transfer models to generate top of atmosphere (TOA) reflectance, surface reflectance, brightness temperature, and masks for clouds, cloud shadows, adjacent clouds, land, and water (USGS, 2015). Landsat 8 Surface Reflectance data are generated from the L8SR algorithm – this is not the same as the one used for Landsat 4-5 and 7 data – instead, this new method currently uses the scene center for the sun angle calculation and then hardcodes the view zenith angle to 0. The solar zenith and view zenith angles are used for calculations as part of the atmospheric correction (USGS, 2015). Landsat CDR for Landsat 8 data have temporal limitations. Corrected data are available only for the period between April 11, 2013 and December 18, 2014. The accuracy and uniformity of this officially conducted atmospheric correction made us to use Landsat CDR scenes for the purposes of this diploma thesis.

All Landsat standard data products are processed using the Level 1 Product Generation System (LPGS) with the following parameters applied: GeoTIFF output format; Cubic Convolution (CC) resampling method; 30-meter (TM, ETM+) pixel size (reflective bands), Universal Transverse Mercator (UTM) map projection (the Cordillera Blanca is situated in 18 S), World Geodetic System (WGS) 84 datum and MAP (North-up) image orientation (USGS, 2015). According to USGS, there are three levels of correction applied to Landsat data:

- Standard Terrain Correction (Level 1T) - ensures systematic radiometric and geometric accuracy by including ground control points while employing a Digital Elevation Model (DEM) for topographic accuracy. Geodetic accuracy of the product

depends on the accuracy of the ground control points and the resolution of the DEM used.

- Systematic Terrain Correction (Level 1Gt) - ensures systematic, radiometric and geometric accuracy, while employing a Digital Elevation Model (DEM) for topographic accuracy.
- Systematic Correction (Level 1G) - ensures systematic radiometric and geometric accuracy, which is derived from data collected by the sensor and spacecraft. Geometric accuracy of the systematically corrected product should be within 250 meters (1 sigma) for low-relief areas at sea level.

Setting up the cloud cover percentage is the last important step in the data acquisition process. In the early process different cloud coverage limits were tested. In the end visual controlling of the available data without setting up the cloud cover criteria was conducted. The final step is listing of search results and controlling of the data to download. Earth Explorer interface contains a RGB preview image, which allows us to visually control cloud cover and general image quality. In some cases, the cloud cover percentage was high, but the cloud cover did not group in the Cordillera Blanca. In these cases the generated image was accepted. If more than one image fulfilled the seasonality and cloud cover criteria for a particular year, the visually most suitable one was selected. It is important to mention, that on May 31, 2003 Landsat 7 Scan Line Corrector (SLC) failed. As the failure caused black lines in the images that could have influenced the results of this thesis, no Landsat 7 image has been accepted since that date.

In the end, 29 data scenes from the period between the years 1987 and 2014 were downloaded. No suitable image was available for the year 2012. The majority of downloaded scenes was taken by Landsat 5 TM sensor (24 pieces). Two images were taken by Landsat 7 ETM+ and Landsat 8 OLI and one image by Landsat 4 TM. After extraction, each of the downloaded '.gz' ('.tar') files contained about 1 GB data. Extracted Landsat Surface Reflectance output from Landsat 8 OLI/TIRS, Landsat 7 ETM+, Landsat 5 TM and Landsat 4 TM contains:

- Surface Reflectance data files (Bands 1-5, 7 for Landsat 4,5,7; Bands 1-7 for Landsat 8) – Band 6 for Landsat 4,5,7 can be ordered separately
- Cloud mask (CFmask) band
- CFmask cloud confidence band
- Surface Reflectance quality files
- Surface Reflectance metadata files
- Readme file

The differences between Landsat 4,5,7 bands and Landsat 8 bands are shown in Table 2. These differences are used for computing the NDSI, NDVI and NDWI indexes and for spectral analyses in the following chapters.

Appendix 1 shows the basic characteristics of downloaded scenes. These are the acquisition date and time, the Landsat generation, the sensor type and the solar angles, i.e. zenith and azimuth.

Table 2: Comparison of Landsat 4,5,7 bands and Landsat 8 bands

Landsat 4,5 TM and Landsat 7 ETM+ Bands				**Landsat 8 OLI/TIRS Bands**			
	Bandwiths [µm]	**Band name**	**Resolution [m]**		**Bandwiths [µm]**	**Band name**	**Resolution [m]**
				Band 1	0,435-0,451	Costal/Aerosol	30
Band 1	0,441-0,514	Blue	30	Band 2	0,452-0,512	Blue	30
Band 2	0,519-0,601	Green	30	Band 3	0,533-0,590	Green	30
Band 3	0,631-0,692	Red	30	Band 4	0,636-0,673	Red	30
Band 4	0,772-0,898	NIR	30	Band 5	0,851-0,879	NIR	30
Band 5	1,547-1,749	SWIR-1	30	Band 6	1,566-1,651	SWIR-1	30
Band 6	10,31-12,36	TIR	60	Band 10	10,60-11,19	TIR-1	100
				Band 11	11,50-12,51	TIR-2	100
Band 7	2,064-2,345	SWIR-2	30	Band 7	2,107-2,294	SWIR-2	30
Band 8	0,515-0,896	Pan	15	Band 8	0,503-0,676	Pan	15
				Band 9	1,363-1,384	Cirrus	30

3.2 ASTER GDEM

Generally, two digital elevation models are available in the Cordillera Blanca: the ASTER GDEM version 2 and the SRTM version 3. Both are available via USGS Earth Explorer. With respect to the quality differences in the Cordillera Blanca (presented in Figure 13), the ASTER GDEM 2 has been selected to download and use for the purposes of further analyses.

The Advanced Spaceborne Thermal Emission and Reflection Radiometer (ASTER) Global Digital Elevation Model (GDEM) is being distributed from the Ministry of Economy, Trade, and Industry (METI) Earth Remote Sensing Data Analysis Center (ERSDAC) in Japan and the National Aeronautics and Space Administration (NASA) Earth Observing System (EOS) Data Information System (EOSDIS) Land Processes (LP) Distributed Active Archive Center (DAAC) in the United States (ASTER GDEM 2 Readme file, 2011). ASTER GDEM2 was released in October 2011 and has made a significant improvement in comparison to the first version, which had many errors in the Cordillera Blanca region. ASTER GDEM2 is a compilation

of ASTER DEMs that are acquired on different dates and then stacked together. In general, the more cloud-free scenes that cover a point, the higher the elevation accuracy. For most areas in the Cordillera Blanca, the GDEM2 was created using 10 to 20 ASTER scenes. This corresponds to about 8 m vertical root-mean-square error (RMSE). On the other hand, there are also large areas in the northern part of the Cordillera Blanca, where the DEM was only generated from up to 5 scenes. This corresponds to between 8 and 15 m vertical RMSE. Although the nominal grid resolution of the ASTER GDEM2 is 30 m, the actual horizontal resolution was determined to be about 72 m (ASTER GDEM Validation Team et al., 2011).

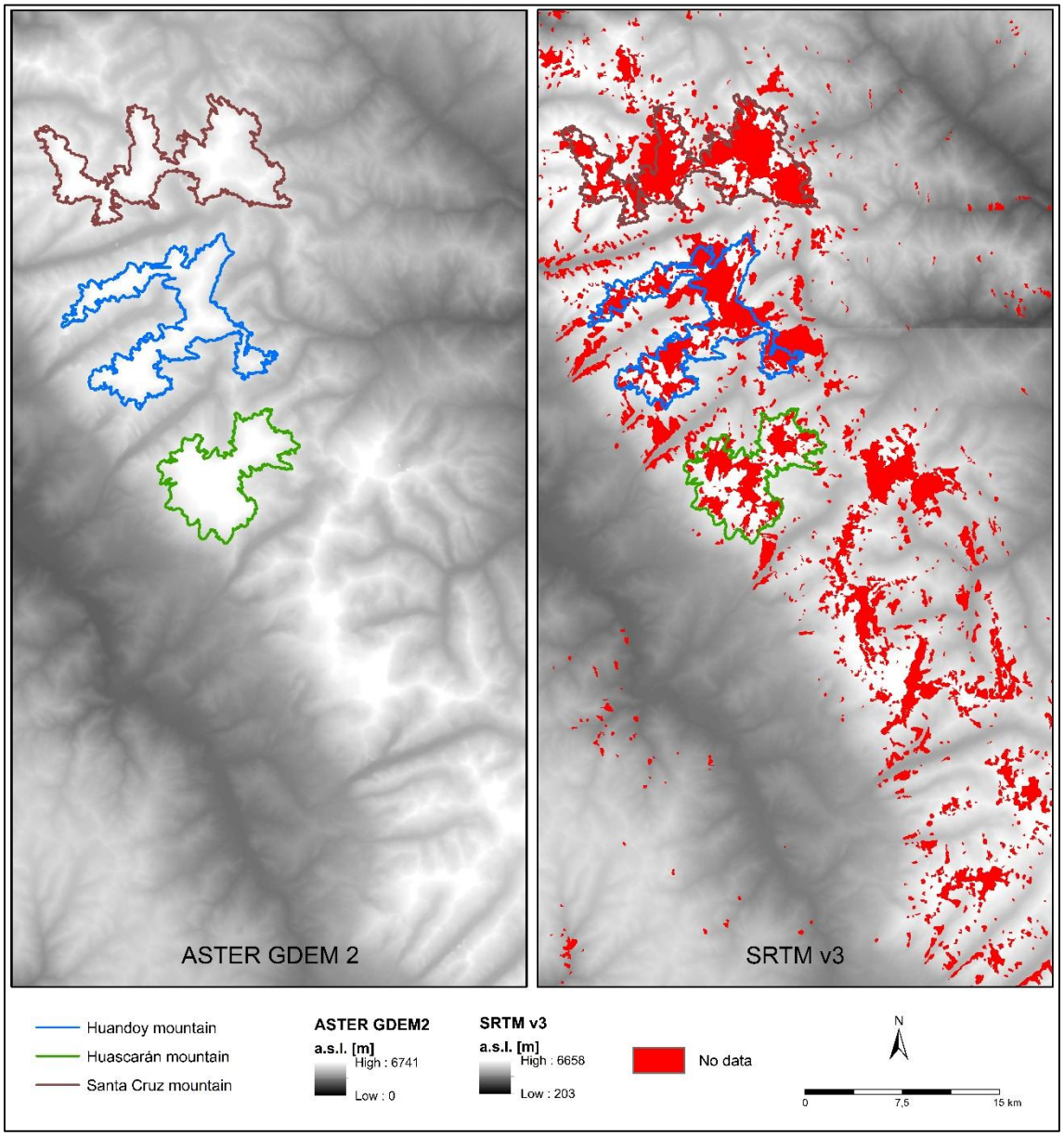

Figure 13: Quality comparison of the ASTER GDEM 2 and the SRTM v3 in the Cordillera Blanca

As Landsat scenes, ASTER GDEM data are also free to download via USGS Earth Explorer interface. Following the selection of the Cordillera Blanca region, the Digital Elevation – ASTER GLOBAL DEM item has be selected in the Data Sets tab. For ASTER GDEM no additional search criteria have to be set. Because of the long north-south dimension of the Cordillera Blanca, both S09W078 and S10W078 scenes were downloaded and afterwards merged into one scene using ENVI 5.0. Each downloaded tile contains a DEM (.dem), a quality assessment (QA, .num) and a readme file (.pdf), all of which are compressed to a '.zip' file. General basic characteristics of ASTER GDEM are listed in Table 3.

Table 3: ASTER GDEM general characteristics (ASTER GDEM 2 Readme, 2011)

Tile Size	3601 x 3601 (1° x 1°)
Pixel Size	1 arc-second
Geographic Coordinate System	Geographic latitude and longitude
DEM Output Format	GeoTIFF, signed 16-bit, in units of vertical meters; Referenced to the WGS84/EGM96 geoid
Special DN Values	-9999 for void pixels, and 0 for sea water body
Coverage	North 83 to South 83, 22,702 tiles

3.3 Landsat data preprocessing

Generally, preprocessing of raw data is essential in order to get the most accurate and unified results of analyses, given that the data come from several years and are created by different sensors. The preprocessing of input data consists of atmospheric correction, topographic correction, orthorectification and coregistration. Some of these preprocessing steps are already reflected in Landsat CDR images.

3.3.1 Atmospheric correction

Atmospheric correction is the process of removing the effects of the atmosphere on the reflectance values of images taken by satellite or airborne sensors. The objective of atmospheric correction is to retrieve the surface reflectance, which characterizes the surface properties. Atmospheric correction algorithms consist of two major steps:

- In the first step, optical properties of the atmosphere are estimated either by using special features of the ground surface or by direct measurements of the atmospheric factors or by using theoretical models. Given the atmospheric optical properties,

various quantities related to the atmospheric correction can be computed by the radiative transfer algorithms.

- In the second step, the remotely sensed imagery can be corrected based on inversion procedures that derive the surface reflectance.

ENVI software includes three radiometric correction modules for Landsat data:

- Calibrate Landsat (Radiometric Correction):
  This tool converts Landsat TM or ETM digital numbers to radiance or exoatmospheric reflectance (reflectance above the atmosphere). Calibration coefficients can be found in Landsat metafiles or downloaded from web servers.
- QUick Atmospheric Correction (QUAC) (Radiometric Correction/Atmospheric Correction Module):
  QUAC is a method of atmospheric correction for multispectral and hyperspectral imagery that works with wavelengths ranging from the visible and near-infrared to shortwave infrared. QUAC determines atmospheric correction parameters directly from the observed pixel spectra in a scene, without ancillary information. QUAC is based on the empirical finding that the average reflectance of diverse material spectra is not dependent on each scene, thus processing is faster than in the case of first-principles methods. QUAC can also be used for any view angle or solar elevation angle. QUAC can still retrieve reasonably accurate reflectance spectra, even if a sensor does not have appropriate radiometric or wavelength calibration, or in case the solar illumination intensity is unknown (Exelis Visual Information Solutions, 2015).
- FLAASH Atmospheric Correction (/Radiometric Correction/Atmospheric Correction Module):
  Compared to the QUAC or the Landsat Calibration Tool, Fast Line-of-sight Atmospheric Analysis of Hypercubes (FLAASH) is a more complex atmospheric correction module. In addition to the basic sensor and measuring properties, FLAASH includes e.g. atmospheric models options, water retrieval options and aerosol options. On the other hand, this module needs more input information.

Generally, Landsat Calibration Module and QUick Atmospheric Correction Module require only basic sensor measurement values, which can be found in metadata files. On the other hand, FLAASH Atmospheric Correction needs further information, which is difficult to find or apply. As mentioned in chapter 3.1, Second Simulation of a Satellite Signal in the Solar Spectrum (6S) radiative transfer models are applied to Landsat CDR data in order to generate top of atmosphere reflectance, surface reflectance, brightness temperature and masks for clouds, cloud shadows, adjacent clouds, land and water. In view of the above, Landsat CDR data were

downloaded and used for the purposes of this diploma thesis instead of conducting equally or less correct atmospheric correction using ENVI tools.

3.3.2 Topographic correction

When possible, satellite images used for change analysis in mountainous terrain should also be corrected for topographic effects like slope and aspect, since these effects can introduce additional radiometric distortion, especially in mid-infrared bands (Kawata et al., 1990, Cit. In Burns and Nolin, 2014). There are two methods for applying topographic correction, i.e. band rationing and correction based on local illumination geometry. Band ratios have been shown to eliminate, or at least to reduce illumination differences resulting from rugged terrain (Jensen, 2005, Cit. In Burns and Nolin, 2014). Corrections based on local illumination geometry require an accurate digital elevation model that has the same resolution as the data acquired from the sensor (Burns and Nolin, 2014). The quality of the topographic correction process strongly depends on the quality of the digital elevation model. In the Cordillera Blanca, because of the high elevation differences, only a few digital elevation models are available. These are:

- ASTER Global DEM (version 2, year 2011 – available via USGS Earth Explorer)
- SRTM DEM (version 4.1, available via The CGIAR Consortium for Spatial Information website)
- DEM generated from Carta National del Peru (year 1987 – effective scale 1:25000, Cit. In Georges, 2004)

In this diploma thesis, due to the lack of quality DEM, no topographic correction has been applied to Landsat data. Inaccuracy caused by this decision has been reduced by applying normalized difference indexes and separated snow classification in the illuminated and shadowed areas.

3.3.3 Image coregistration

Landsat CDR scenes downloaded via USGS Earth Explorer are generally projected and coregistered. On the other hand, detailed visual and statistical examination revealed a mistake, which had to be corrected. In the early stages of thesis writing, the correlation between the downloaded scenes was computed using ESRI ArcMap 10.2.2. Band Collection Statistics Tool. As the first step, for each of the Landsat scenes a subset of 2300 by 2300 pixels over the Cordillera Blanca was created using ENVI. For completing this task SWIR band (band 5 for Landsat 4,5 and 7; band 6 for Landsat 8) was chosen, as in this band the cloud cover is easier to visually detect. Subsequently, covariance and correlation matrix was computed using Band Collection Statistics

Tool. The final correlation matrix is shown in Appendices 2 and 3. The value of correlation with other bands is in the interval 0,5-0,75 for 5 scenes, whereas for 3 scenes it is lower than 0,5.

There are three possible explanations of these results. Firstly, Landsat scenes from years 1993 (Landsat 5), 2000 (Landsat 5), 2004 (Landsat 5), 2007 (Landsat 5) and 2009 (Landsat 5), which have a correlation value ranging from 0,5-0,75, were partly covered by clouds. Likewise, Landsat scenes from years 1989 (Landsat 4) and 2011 (Landsat 5), with a correlation value lower than 0,5, were significantly covered by clouds. Secondly, different snow extent, different water extent and different vegetation extent could lower correlation values, too. These scenes were excluded from the analysis of the whole range of the Cordillera Blanca, but used for the analysis of some particular glaciers. Finally, visual check of the images showed, that the Landsat scene from the year 1999 (Landsat 7) suffered from geometric distortion.

Additionally, a Matlab algorithm (shown in Appendix 4) has been applied to compare Landsat scenes through control points. The difference between scene pairs was calculated through 9 control points. The sample area around the points in the first image was set to 15 by 15 pixels. The search area in the second image was set to 31 by 31 pixels, i.e. 4 times the sample crop. During the algorithm, the search window (15 by 15 pixels) was shifted across the search area and correlation values were computed between the sample area and the search window. The highest correlation value and the correspondent distance between centers (center of the sample area and the search window) were saved for each of the 9 control points. In the last step, the maximum and the median value of the distances was computed. The maximum distance values are represented in Appendices 5 and 6. The median distance values equaled 0 pixels, except of the Landsat scenes from years 1999 (Landsat 7) and 2011 (Landsat 5). The median distance values for these two Landsat scenes are shown in Appendix 7. The observed median distance values for the Landsat 5 scene from the year 2011 can be explained by high cloud cover. On the other hand, as described previously, the Landsat 7 scene from the year 1999 had geometric distortion. Geometric transformation has been applied in order to eliminate this defect.

The geometric transformation of the Landsat scene from the year 1999 (Landsat 7) was completed using ENVI Registration: Image to image tool (/Geometric correction/Registration). The Landsat scene from the year 1999 (Landsat 5) was selected for the base map. In the first step, 14 Ground control points (GCPs) with equal spatial distribution were selected (Figure 14). Based on these points, 1st degree polynomial transformation (Affine Transformation) was completed with a total RMS error of 1,1 pixels. The detailed RMS error distribution is shown in Appendix 8. In the next step, the transformed scene was used to create a subset of 2300 by 2300 pixels over the Cordillera Blanca. To test the results of the geometric transformation, the correlation calculation using ArcMap and the median distance calculation using Matlab have been repeated.

The results are represented in Appendix 9. After completing the geometrical transformation, the results show a significant increase in correlation and a significant decrease in median distances between Landsat scenes from different years. For further analyses the transformed Landsat 7 scene from the year 1999 was used.

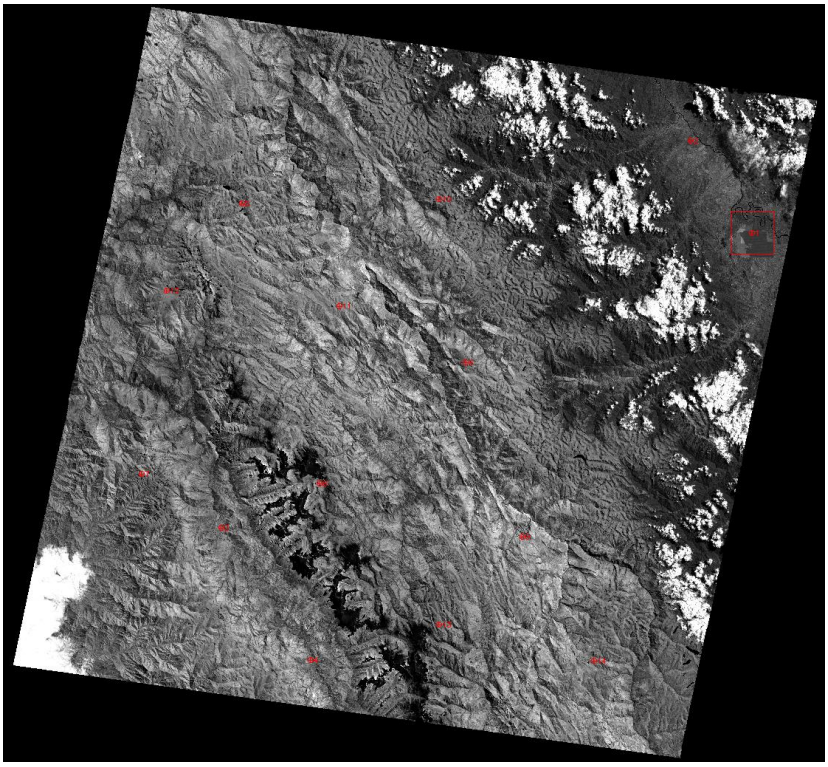

Figure 14: Selected ground control points for geometric transformation of Landsat scene from the year 1999 (Landsat 7)

3.3.4 Index computing and band stacking

Prior to the classification procedure, band indexes had been calculated, as a significant part of the classification is based on these indexes. Theoretical information regarding index calculation was discussed in previous chapters, however, due to Landsat sensor differences, practical calculation varies for each particular Landsat generation. The computations were realized using ENVI Band Math Tool (/Band ratio). The formulas used in this tool are indicated in Table 4. An example of the index computation results (NDVI, NDWI, NDSI) is shown if Figure 15.

Table 4: NDVI, NDWI, NDSI calculation formula for Landsat 4,5,7 and 8

	Landsat 4, 5 and 7	**Landsat 8**
NDVI	float(band 4 - band 3) / float(band 4 + band 3)	float(band 5 - band 4) / float(band 5 + band 4)
NDWI	float(band 4 - band 5) / float(band 4 + band 5)	float(band 5 - band 6) / float(band 5 + band 6)
NDSI	float(band 2 - band 5) / float(band 2 + band 5)	float(band 3 - band 6) / float(band 3 + band 6)

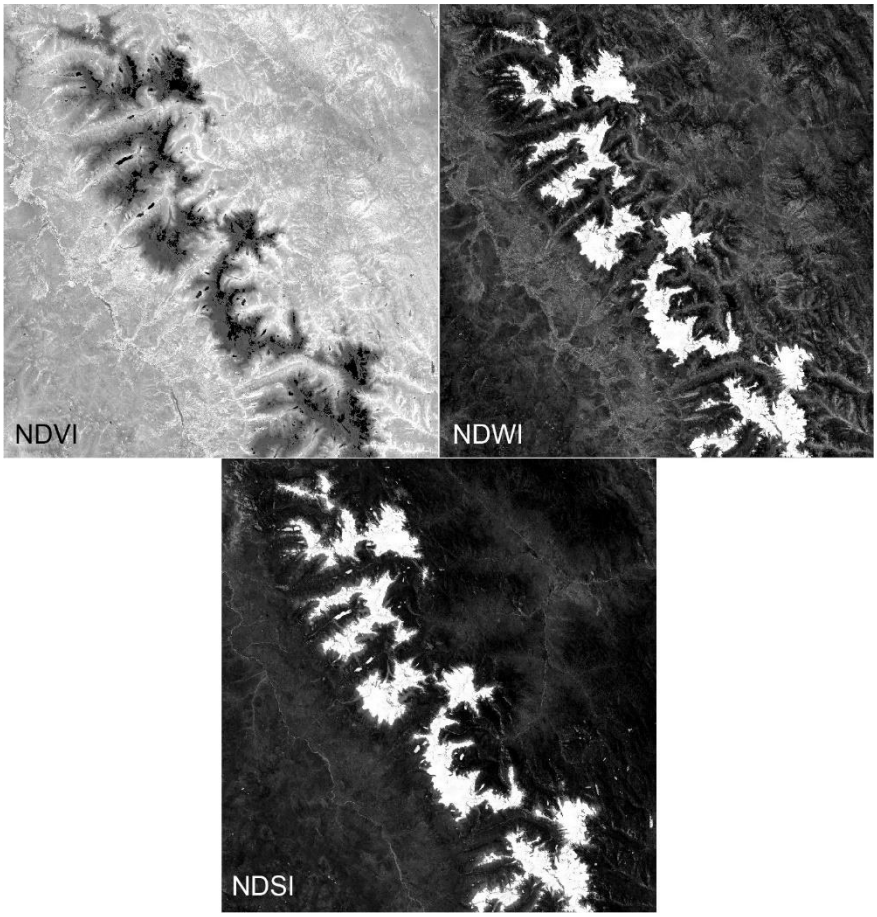

Figure 15: Example of NDVI, NDWI and NDSI computation results – applied for the Landsat 5 scene from the year 1999

This has been the last step of Landsat preprocessing followed by spectral analysis and providing classification algorithm. All the bands and indexes for each of the Landsat scenes were stacked together using ENVI Layer Stacking Tool (/Raster Management) and a 2400 by 2500 pixels subset over the Cordillera Blanca has been created. In order to facilitate the analysis, only the stacked subsets were used in the subsequent parts of the diploma thesis.

3.4 ASTER GDEM preprocessing

In the first step of ASTER GDEM preprocessing, the two downloaded scenes had to be merged. As mentioned in chapter 3.2, two separate scenes (S09W078 and S10W078) had to be downloaded because of the north-south length of the Cordillera Blanca. The process of merging was completed using ENVI Georeferenced Mosaicking Tool (/Mosaicking). The two downloaded images were loaded into the tool, which then automatically placed the images in the right order. The final image was saved as a TIFF file.

In the next step, the digital elevation model had to be reprojected to Universal Transvers Mercator (UTM) to match the Landsat data projection. This has been completed using ENVI Project Raster Tool (/Raster Management). After loading the input file, the output Coordinate System had to be selected. The Cordillera Blanca is situated in the WGS 1984 UTM Zone 18S (/Projected Coordinate Systems/UTM/WGS 1984/Southern Hemisphere). In order to match Landsat data pixel size, the output pixel size was set to 30 m. The resampling was set to Nearest Neighborhood. The final image was saved as a TIFF file.

In the final step, a subset of the Cordillera Blanca was created based on the Landsat 5 subset scene from the year 1999. This was feasible, because the ASTER GDEM projection and pixel size were the same as the Landsat projection and pixel size. In the subsequent parts of the diploma thesis, this ASTER GDEM subset was used.

Further analyses required two additional scenes, i.e. slope and aspect, which were computed based on ASTER GDEM. These files were created using ENVI Topographic Modeling Tool (/Terrain). For the kernel size, 9 by 9 pixels was chosen.

3.5 Spectral analyses

Spectral analysis is the process of comparing measured reflectance values in different bands, i.e. different wavelengths, for each observed type of land cover. The final output of this process is a spectral reflectance curve. The main task is to find spectral differences between the observed land covers in order to enable their separation during the classification process.

In this diploma thesis two groups of sensors are used depending on the measured wavelength. The first group contains Landsat 4 TM, Landsat 5 TM and Landsat 7 ETM+ sensors. The second group contains Landsat 8 OLI/TIRS. The differences between their band distribution are explained in chapter 3.1. The spectral analysis needs to be done for both groups, so that one may know, which band and index combinations should be included in the classification algorithm.

The spectral analysis was entirely completed using ENVI 5.0 software. This process consists of different steps. For the first group, the Landsat 5 scene from the year 2010 was

selected, whereas for the second group, the Landsat 8 scene from the year 2013 was selected. For both scenes, the subset of the Cordillera Blanca from the multiband stacked image (the stacked image contains all the bands and indexes that were computed during the Landsat image preprocessing) was used.

In the first step, different Regions of Interests (ROIs), i.e. for water, snow, snow in shadow, vegetation, rock and debris-covered snow, had to be defined. Because of the lack of topographic correction, 'snow' and 'snow in shadow' had to be defined separately. In the latter stages, these two classes were merged together as snow cover. Besides the band and index images, the Google Earth software, as well as visual interpretation of the objects' forms and shapes were used for the purposes of ROI assignment. For the Landsat 5 image 46 Regions of Interests were selected, whereas for the Landsat 8 image 65 Regions of Interests were selected. Their distribution over the Cordillera Blanca is represented in Figures 16 and 17.

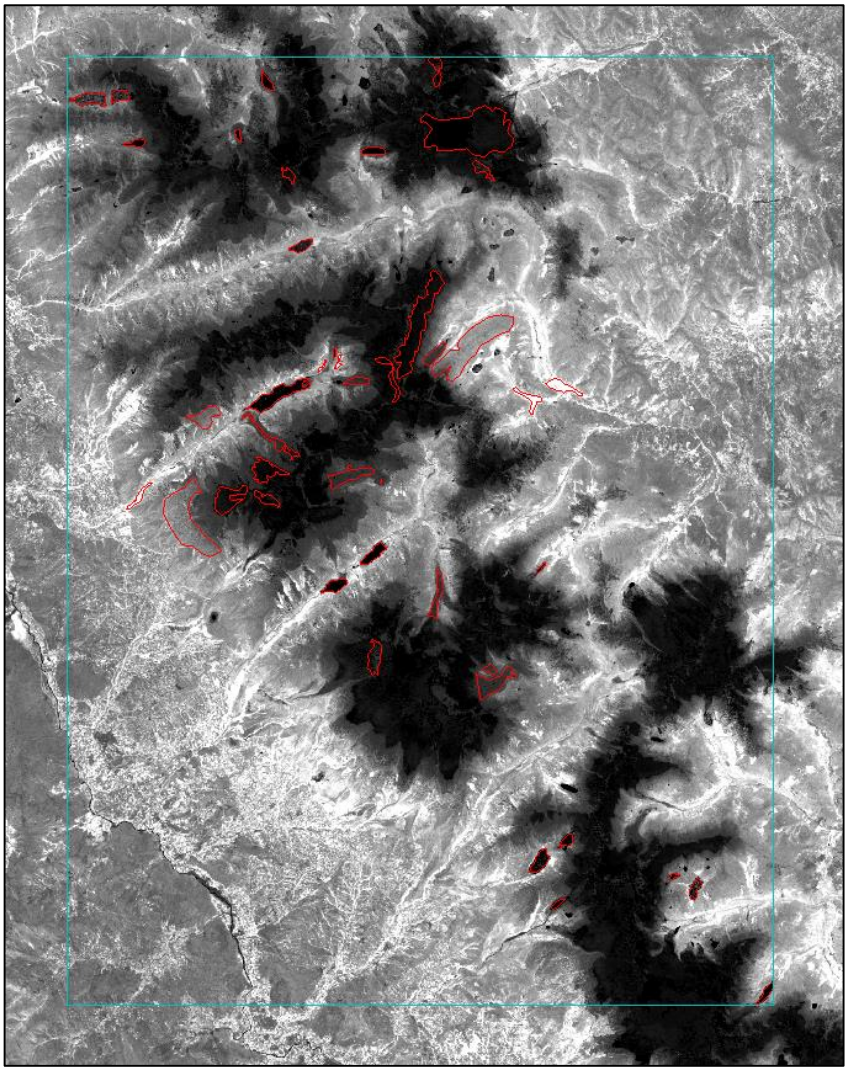

Figure 16: Selected ROIs over NDVI image (Landsat 5 of the year 2010) – ROIs represented as red polygons

The selected ROIs were connected to the stacked images. Statistical spectral characteristics were computed and exported to Excel for each land cover type. This is specified in Tables 5 and 6. For bands they contain minimal value, maximal value, mean value and standard deviation value of reflectance and for indexes they contain the respective index value ranging from -1 to +1. The mean values were visually interpreted in line charts (Figures 18 to 21). The standard deviation value was used to show the error interval. These line charts helped to separate the observed types of land cover and to create the classification algorithm. In the next part of this chapter, the spectral reflectance curve of the Landsat 5 and Landsat 8 scenes will be discussed.

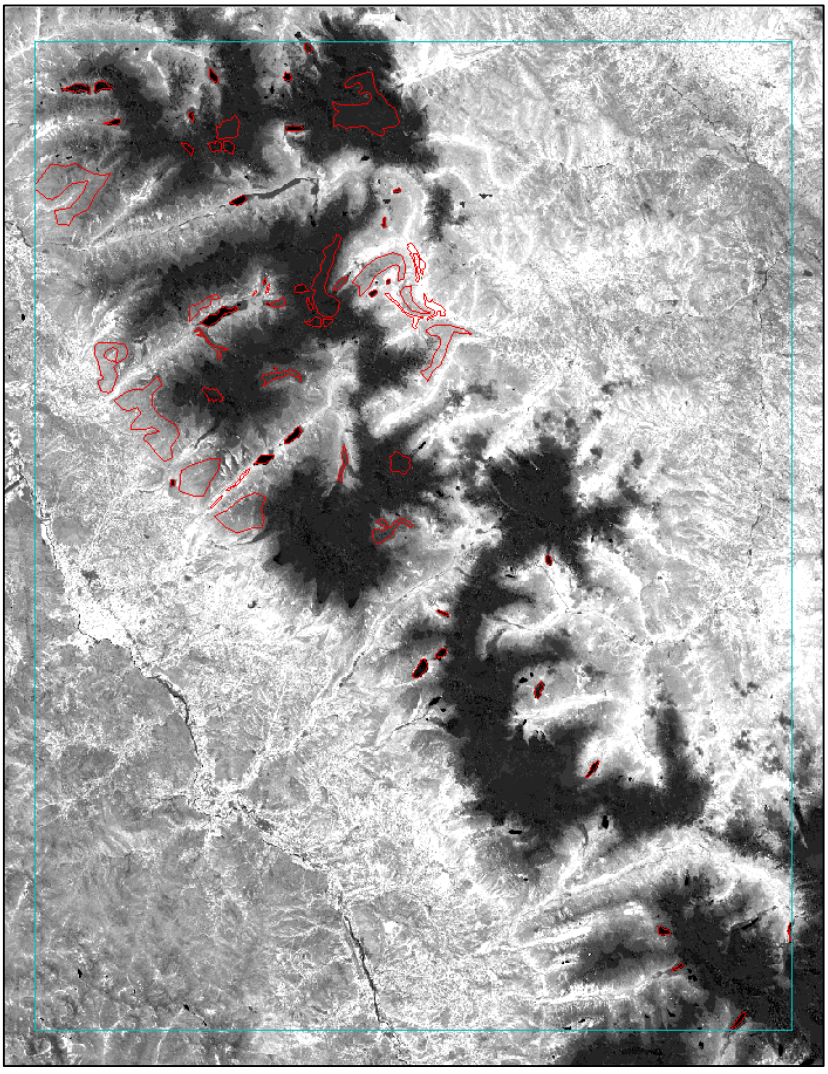

Figure 17: Selected ROIs over NDVI image (Landsat 8 of the year 2013) – ROIs represented as red polygons

The spectral reflectance curves based on Landsat 5 and Landsat 8 bands do not show big differences between water, vegetation, rock, debris-covered snow and snow in shadow. On the other hand, in Figures 18 and 20 snow has a considerably different curve, than the rest of land cover types. Band 1 of Landsat 5 is suitable for snow separation, whereas Bands 2 to 7 have a risk of misclassification. Bands 1 to 5 of Landsat 8 are suitable for snow separation, whereas Bands 6

and 7 are not applicable for this purpose. In the classification algorithm, Band 1 of all Landsat generations will be used for snow separation.

Table 5: Spectral characteristics of selected land cover types (Landsat 5 – year 2010)

water					**vegetation**				
	min	**max**	**mean**	**stdev**		**min**	**max**	**mean**	**stdev**
Band 1	274	3882	880,8	397,0	**Band 1**	202	654	345,3	64,2
Band 2	188	4293	825,2	506,1	**Band 2**	195	984	438,6	94,9
Band 3	98	4149	484,3	421,6	**Band 3**	193	1092	441,5	115,3
Band 4	15	3271	336,9	255,4	**Band 4**	553	3340	2029,3	429,2
Band 5	-8	2507	232,4	143,0	**Band 5**	342	2872	1457,6	383,4
Band 7	-12	2339	205,7	133,9	**Band 7**	175	1755	799,0	245,3
NDVI	-0,77	0,37	-0,1	0,2	**NDVI**	0,35	0,79	0,6	0,1
NDWI	-0,88	1,12	0,2	0,2	**NDWI**	-0,15	0,36	0,2	0,1
NDSI	-0,45	1,06	0,5	0,2	**NDSI**	-0,64	-0,19	-0,5	0,1
snow					**rock**				
Band 1	554	16000	13942,7	4683,1	**Band 1**	142	2075	583,0	197,5
Band 2	322	16000	6261,0	2577,7	**Band 2**	121	2396	695,1	224,4
Band 3	388	16000	8402,2	5066,3	**Band 3**	133	2540	790,9	233,3
Band 4	397	8809	5655,5	1527,6	**Band 4**	254	3007	1381,8	320,5
Band 5	62	1947	461,4	177,5	**Band 5**	166	3980	2351,1	580,7
Band 7	-12	1719	337,9	133,2	**Band 7**	99	4010	1841,7	527,2
NDVI	-0,48	0,06	-0,1	0,2	**NDVI**	0,07	0,57	0,3	0,1
NDWI	0,32	0,94	0,9	0,0	**NDWI**	-0,39	0,21	-0,3	0,1
NDSI	0,33	0,96	0,9	0,0	**NDSI**	-0,67	0,07	-0,5	0,1
snow in shadow					**debris-covered snow**				
Band 1	451	2958	977,5	279,9	**Band 1**	712	3796	2189,3	470,7
Band 2	399	2856	840,2	267,4	**Band 2**	856	4190	2443,3	501,7
Band 3	338	2553	761,7	252,8	**Band 3**	982	4351	2523,2	520,7
Band 4	255	2648	729,5	228,7	**Band 4**	1001	4878	2879,7	578,9
Band 5	14	1170	215,5	99,0	**Band 5**	795	5695	3325,9	574,5
Band 7	-87	1079	179,6	95,1	**Band 7**	705	5944	3372,8	585,8
NDVI	-0,22	0,15	0,0	0,0	**NDVI**	-0,25	0,23	0,1	0,0
NDWI	-0,18	0,93	0,5	0,1	**NDWI**	-0,25	0,13	-0,1	0,0
NDSI	-0,09	0,95	0,6	0,2	**NDSI**	-0,48	0,46	-0,2	0,1

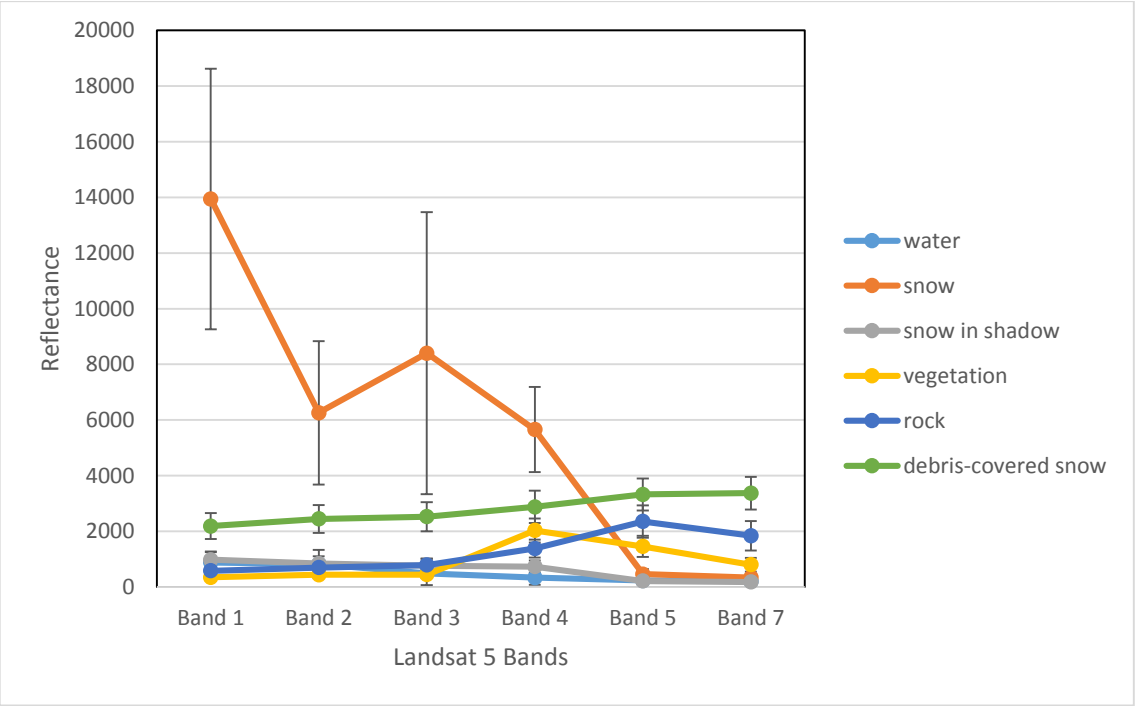

Figure 18: Spectral reflectance curve of selected land cover types as the function of Landsat 5 Bands

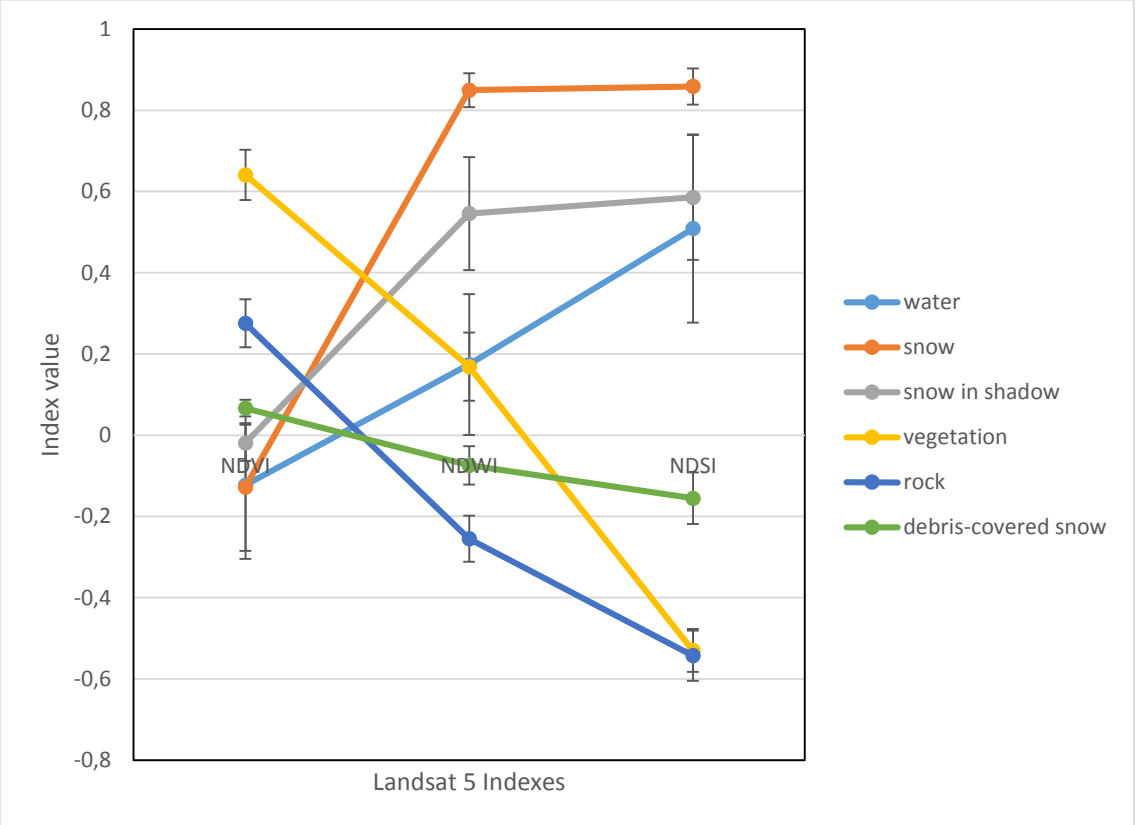

Figure 19: Spectral reflectance curve of selected land cover types as the function of Landsat 5 Indexes

Table 6: Spectral characteristics of selected land cover types (Landsat 8 – year 2013)

water					**vegetation**				
	min	**max**	**mean**	**stdev**		**min**	**max**	**mean**	**stdev**
Band 1	170	3519	676,2	310,3	**Band 1**	221	550	338,7	47,1
Band 2	189	3811	798,4	420,8	**Band 2**	206	551	339,9	54,7
Band 3	130	3855	802,8	516,6	**Band 3**	198	816	427,9	100,8
Band 4	24	3838	342,2	234,0	**Band 4**	157	728	371,4	100,3
Band 5	4	3116	156,2	106,6	**Band 5**	664	4182	2059,8	580,9
Band 6	-8	2025	130,4	92,2	**Band 6**	375	2479	1256,7	401,0
Band 7	32	1799	119,5	80,4	**Band 7**	190	1485	659,8	222,9
NDVI	-0,94	0,38	-0,3	0,2	**NDVI**	0,38	0,87	0,7	0,0
NDWI	-0,78	1,31	0,1	0,1	**NDWI**	-0,01	0,49	0,2	0,1
NDSI	-0,53	1,03	0,7	0,2	**NDSI**	-0,60	-0,19	-0,5	0,1
snow					**rock**				
Band 1	3886	11693	9208,2	906,7	**Band 1**	6	2150	449,8	165,4
Band 2	3825	12331	9638,2	985,3	**Band 2**	24	2445	493,4	193,9
Band 3	3805	13060	10044,9	1083,6	**Band 3**	7	2907	587,8	238,6
Band 4	3659	13439	10178,5	1141,5	**Band 4**	21	3183	655,9	264,9
Band 5	3245	12277	9227,2	1077,4	**Band 5**	86	3543	1211,0	387,7
Band 6	200	2847	710,7	217,6	**Band 6**	135	4248	1638,1	552,8
Band 7	196	2935	761,1	220,5	**Band 7**	89	3894	1246,4	512,4
NDVI	-0,15	0,06	0,0	0,0	**NDVI**	-0,06	0,75	0,3	0,1
NDWI	0,36	0,93	0,9	0,0	**NDWI**	-0,46	0,79	-0,1	0,1
NDSI	0,33	0,94	0,9	0,0	**NDSI**	-0,93	0,69	-0,5	0,1
snow in shadow					**debris-covered snow**				
Band 1	852	4122	1505,9	329,3	**Band 1**	351	4064	1542,0	543,9
Band 2	791	4040	1390,2	332,2	**Band 2**	402	4407	1774,3	583,5
Band 3	629	4122	1204,4	335,0	**Band 3**	443	4582	2115,2	623,4
Band 4	486	3934	1065,0	325,8	**Band 4**	459	4835	2234,5	644,0
Band 5	385	3584	892,4	271,5	**Band 5**	456	4978	2406,5	643,1
Band 6	82	449	137,0	23,3	**Band 6**	152	5760	2693,9	626,8
Band 7	78	424	130,8	22,3	**Band 7**	275	5529	2624,1	616,9
NDVI	-0,17	0,05	-0,1	0,0	**NDVI**	-0,38	0,21	0,0	0,0
NDWI	0,45	0,84	0,7	0,1	**NDWI**	-0,30	0,70	-0,1	0,1
NDSI	0,45	0,89	0,8	0,0	**NDSI**	-0,46	0,88	-0,1	0,1

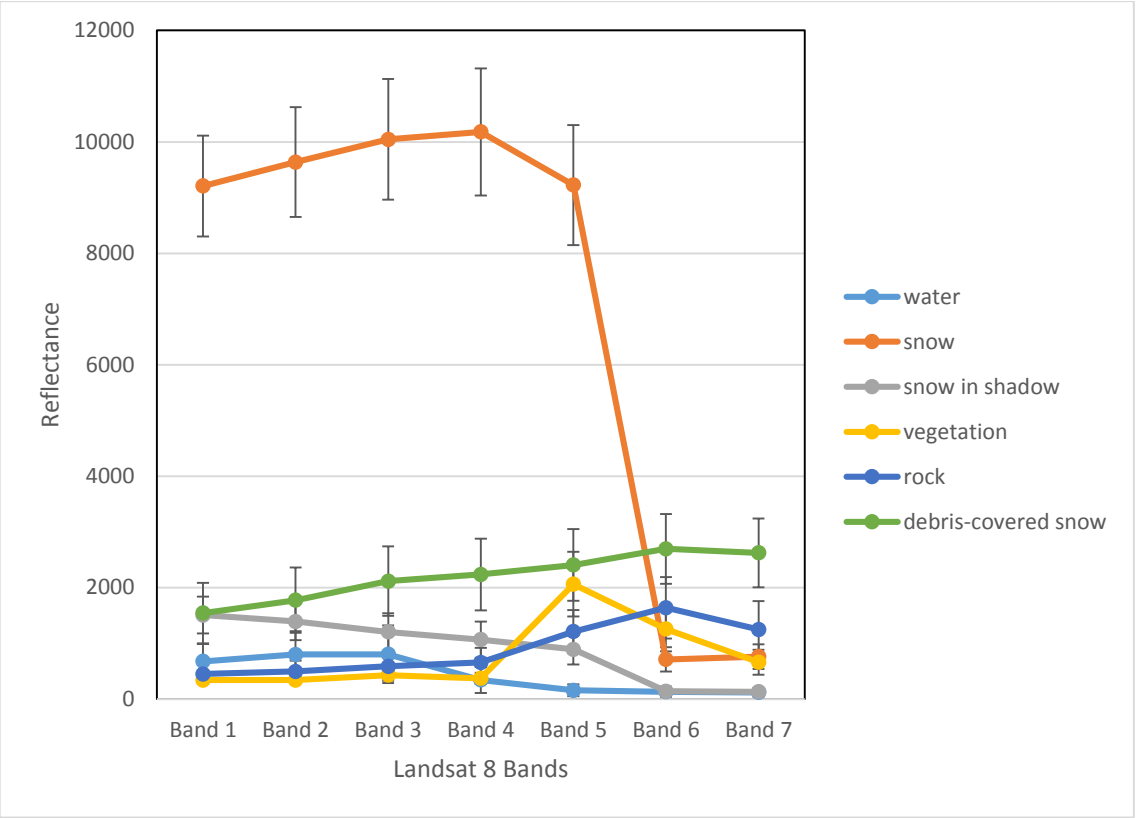

Figure 20: Spectral reflectance curve of selected land cover types as the function of Landsat 8 Bands

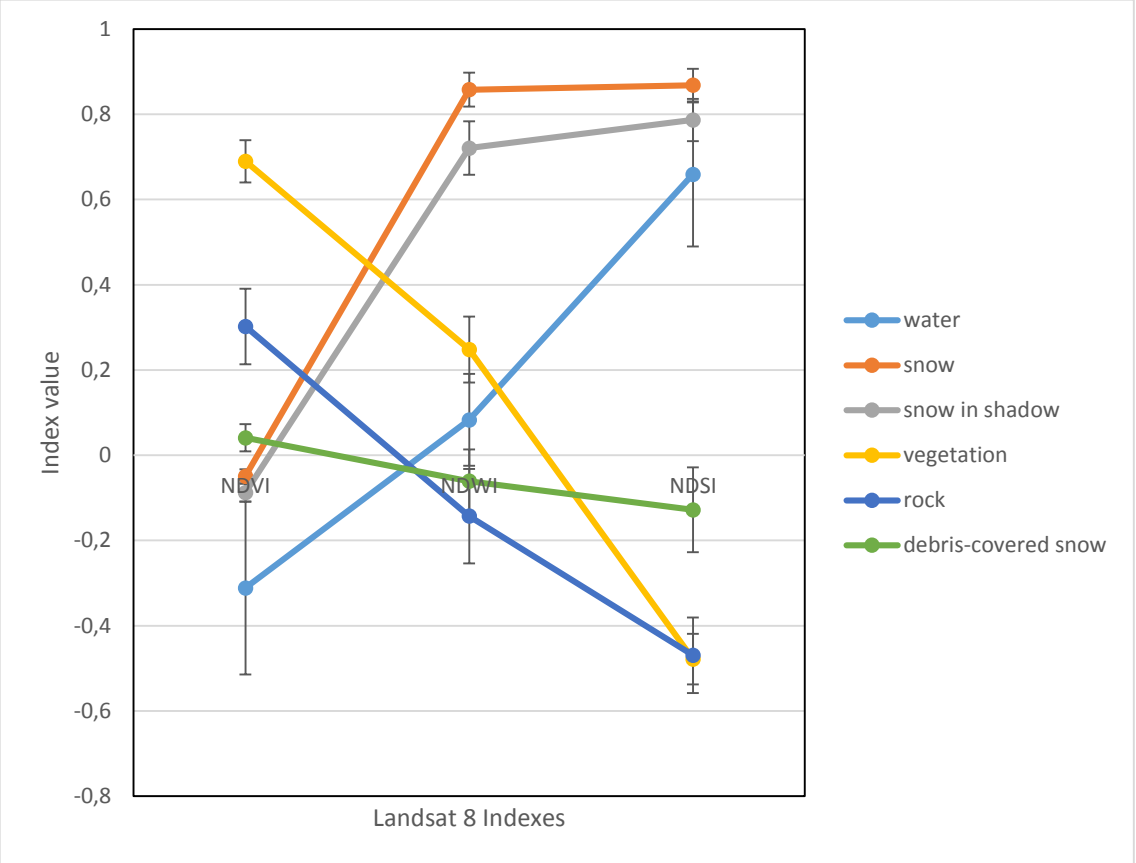

Figure 21: Spectral reflectance curve of selected land cover types as the function of Landsat 8 Indexes

Figures 18 and 20 show, that except for snow separation, Landsat 5 and Landsat 8 bands are not suitable for separating other types of land cover. The remaining land cover separation can be completed using indexes.

NDVI of Landsat 5 and Landsat 8 is not suitable for separating water, snow, snow in shadow, rock or debris-covered snow. On the other hand, vegetation has the highest NDVI value in both Landsat 5 and Landsat 8, which differs from the NDVI value of other land cover types to an extent sufficient for the precise separation of vegetation.

For Landsat 8, the observed types of land cover can be divided into two groups based on NDWI values. These groups are: a) snow and snow in shadow and b) the remaining land cover types. Based on the above discussed process, i.e. the separation of snow based on Band 1, the snow in shadow can be separated based on NDWI values. On the contrary, for Landsat 5, the two groups are not strictly distinguishable, yet snow in shadow is still separable based on NDWI.

For both Landsat 5 and Landsat 8, the observed types of land cover can be divided into two groups based on NDSI values. These groups are: a) snow, snow in shadow and water and b) debris-covered snow, rock and vegetation. Following the separation of snow and snow in shadow, the NDSI values can be used to separate water from the rest of the unclassified areas.

The final and most difficult part of the classification process is the separation of rock from debris-covered snow, as their spectral reference curve is almost the same. However, rock and debris-covered snow can be separated using normalized difference snow index. In order to achieve more precise classification, the ASTER GDEM will be involved in the classification process.

Finally, an automatic classification algorithm can be created based on the differences between the spectral reflectance curves of the observed types of land cover.

3.6 Classification algorithm

The main goal of this diploma thesis is to create a semi-automatic classification algorithm for classifying snow, water, vegetation, debris-covered snow and rock in the Cordillera Blanca. Following the manual setting of the threshold values, this algorithm is based on unsupervised classification methods, masking techniques and conditional raster calculator and has been completed using ENVI 5.0 and ArcMap 10.2.2. The input files of the algorithm are Landsat Band 1, NDVI, NDWI, NDSI and ASTER GDEM images. The classification algorithm comprises several steps, which will be discussed in the next part of this chapter. The algorithm diagram is shown in Figure 22.

At the first stage, a mask of the illuminated snow in the Cordillera Blanca was created using ENVI 5.0. ISODATA classification was used to complete this task. The input image was the Landsat Band 1 scene. As already discussed, the snow is distinctly separated from other observed land cover types at Band 1 wavelengths, hence only 2 classes were requested in the ISODATA classification. The classification created 2 classes with pixel values of 1 and 2. In the next step, where the pixel value was less or equal to 1, the snow mask was created. This mask was used in the later process.

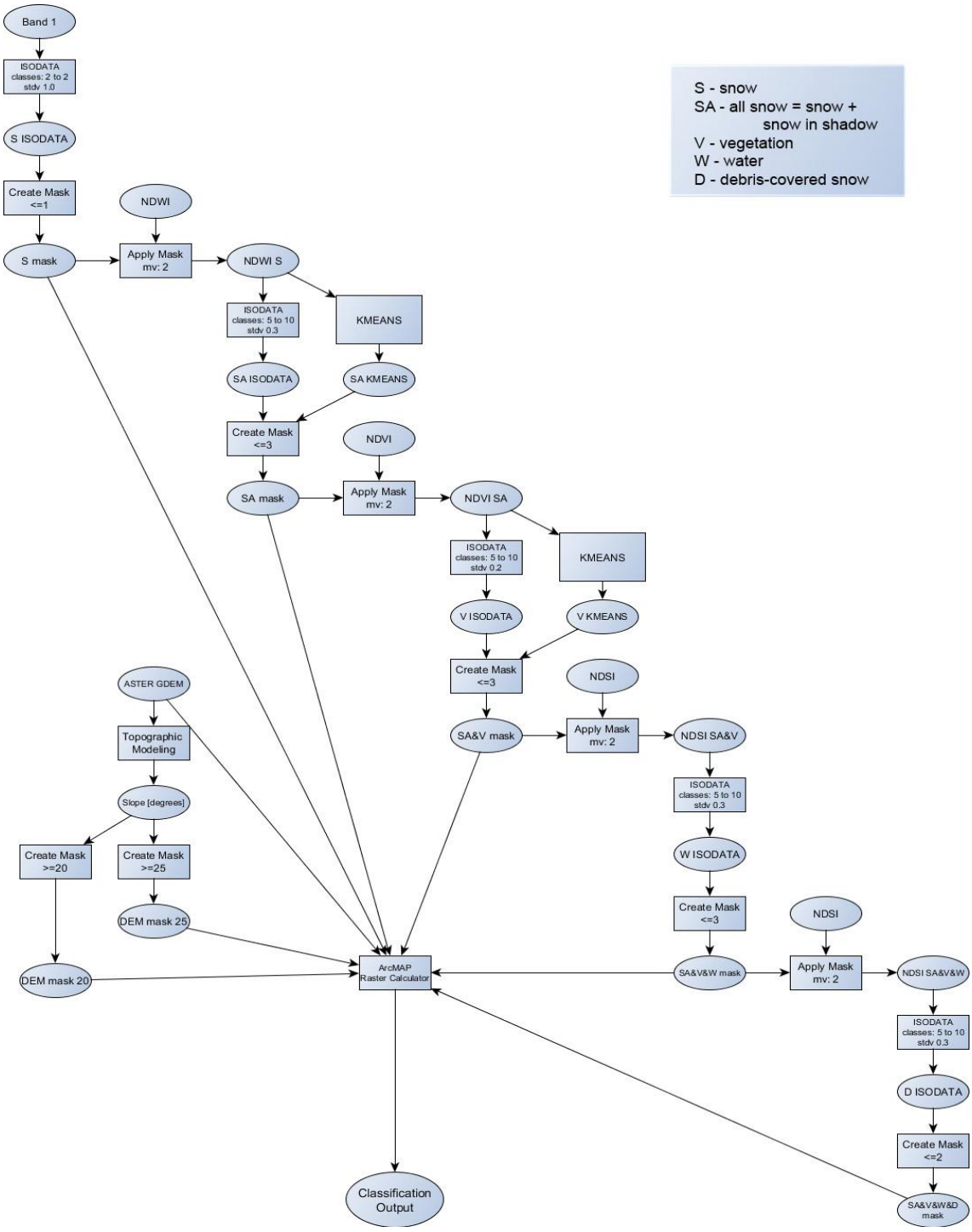

Figure 22: Classification workflow

At the second stage, a mask of all snow, i.e. snow in illuminated areas and in shadowed areas in the Cordillera Blanca was created. The intention was to compensate the lack of topographic correction. The detailed process of creating the mask of all snow is the following: The snow mask from the first step was applied to the NDWI image. The pixel value of the masked areas was set to +2. In the next step of the process, ISODATA classification with maximum in class standard deviation of 0,3 was used. The desired number of classes was set to 5 - 10 and the ISODATA classification created 5 classes based on initial criteria. Visual interpretation showed, that class 5 contains snow in illuminated areas and class 4 contains snow in shadowed areas. Upon these facts, a mask of all snow was created. In three particular years, K-means classification had to be used instead of ISODATA classification. This process will be discussed in the next chapter.

At the third stage of the classification process, a mask of all snow and vegetation was created: The previously created all snow mask was applied to the NDVI image. The pixel value of the masked areas was set to +2. As NDVI pixel values range from -1 to +1, masked areas with +2 pixel value could be clearly separated during the unsupervised classification. Except for two particular years, when using K-means classification, ISODATA classification with maximum in class standard deviation of 0,2 has been completed with an input file of the masked NDVI image. The initial criteria of final class number was set to 5 - 10. The ISODATA classification created 5 classes. Visual interpretation showed, that class 5 contains all snow and class 4 contains vegetation. Upon these facts, a mask of all snow and vegetation was created.

At the fourth stage of the classification process, a mask of all snow, vegetation and water was created: The all snow and vegetation mask was applied to the NDSI image. The pixel value of the masked areas was set again to +2. In this step, the ISODATA classification was suitable for all of the Landsat scenes. Initially, 5 - 10 classes with 0,3 maximum in class standard deviation were required. The minimal value of class members was set to 1000 pixels. The classification process took about 40 iterations and resulted altogether in 5 classes. Based on visual observation, the all snow, vegetation and water mask was created.

At the fifth stage of the classification process, a mask of all snow, vegetation, water and debris-covered snow was created: The all snow, vegetation and water mask was applied to the NDSI image. With the same masking technique, the pixel value of the masked areas was set to +2. ISODATA classification has been completed with an input file of the masked NDSI image. The number of requested classes was set to 5 - 10, however, due to the similarity between pixel values in the image, the final number of classes was only 4. Based on visual observation, the previous criteria of ≤ 3 was changed to ≤ 2. This masking process resulted in the creation of the fifth mask containing all snow, vegetation, water and debris-covered snow. The debris-covered snow areas are clarified in the subsequent parts of the whole classification process.

At the sixth stage of the classification algorithm, ASTER GDEM data were prepared and added to the final calculation process. As discussed in chapter 3.4, the slope analysis was completed using ENVI Topographic Modeling Tool and based on the merged and reprojected ASTER GDEM. The resulting slope image was used to create a mask of 20 degree (areas with slope of less or equal to 20°) and a mask of 25 degree (areas with slope of less or equal to 25°).

At the final stage of the classification process, all of the masks had to be merged in order to create a classified map of the Cordillera Blanca. This process was completed using ArcMap Raster Calculator with the following input images:

- the SA mask containing snow in illuminated areas and snow in shadowed areas,
- the SA&V mask containing all snow and vegetation areas,
- the SA&V&W mask containing all snow, vegetation and water areas,
- the SA&V&W&D mask containing all snow, vegetation, water and debris/covered snow areas,
- the ASTER GDEM image,
- the DEM 20 mask and
- the DEM 25 mask.

Figure 23 demonstrates the differences between SA, SA&V, SA&V&W and SA&V&W&D masks.

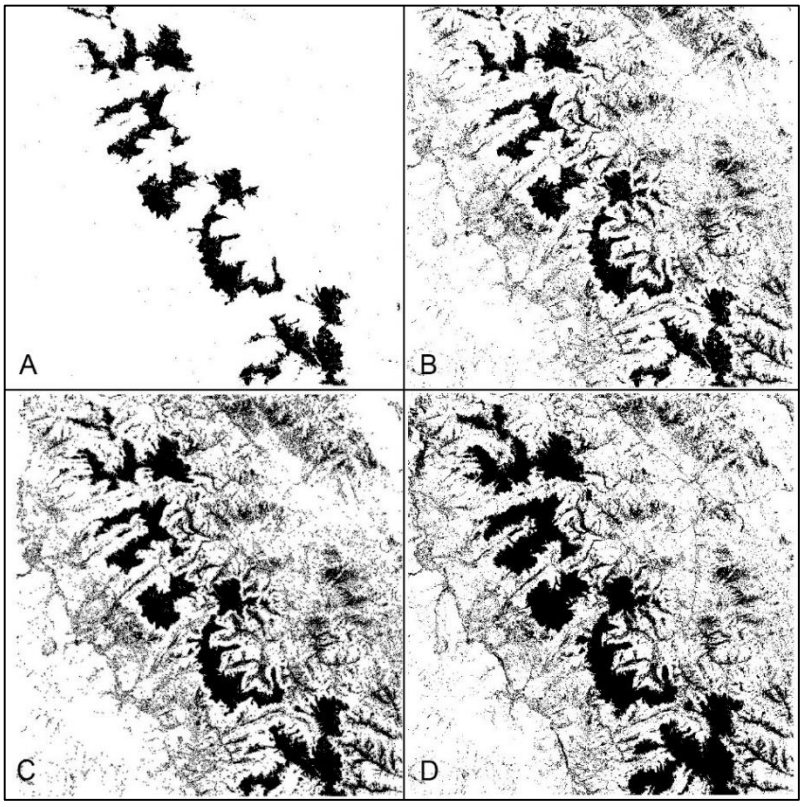

Figure 23: SA (A), SA&V (B), SA&V&W (C) and SA&V&W&D (D) masks comparison

In the Raster Calculator a multiple conditioned expression presented in the Figure 24 was used to assign different class numbers to different types of land cover in the Cordillera Blanca:

- 1 for debris-covered snow areas,
- 2 for water areas,
- 3 for vegetation areas,
- 4 for snowed areas,
- 0 for other unclassified areas.

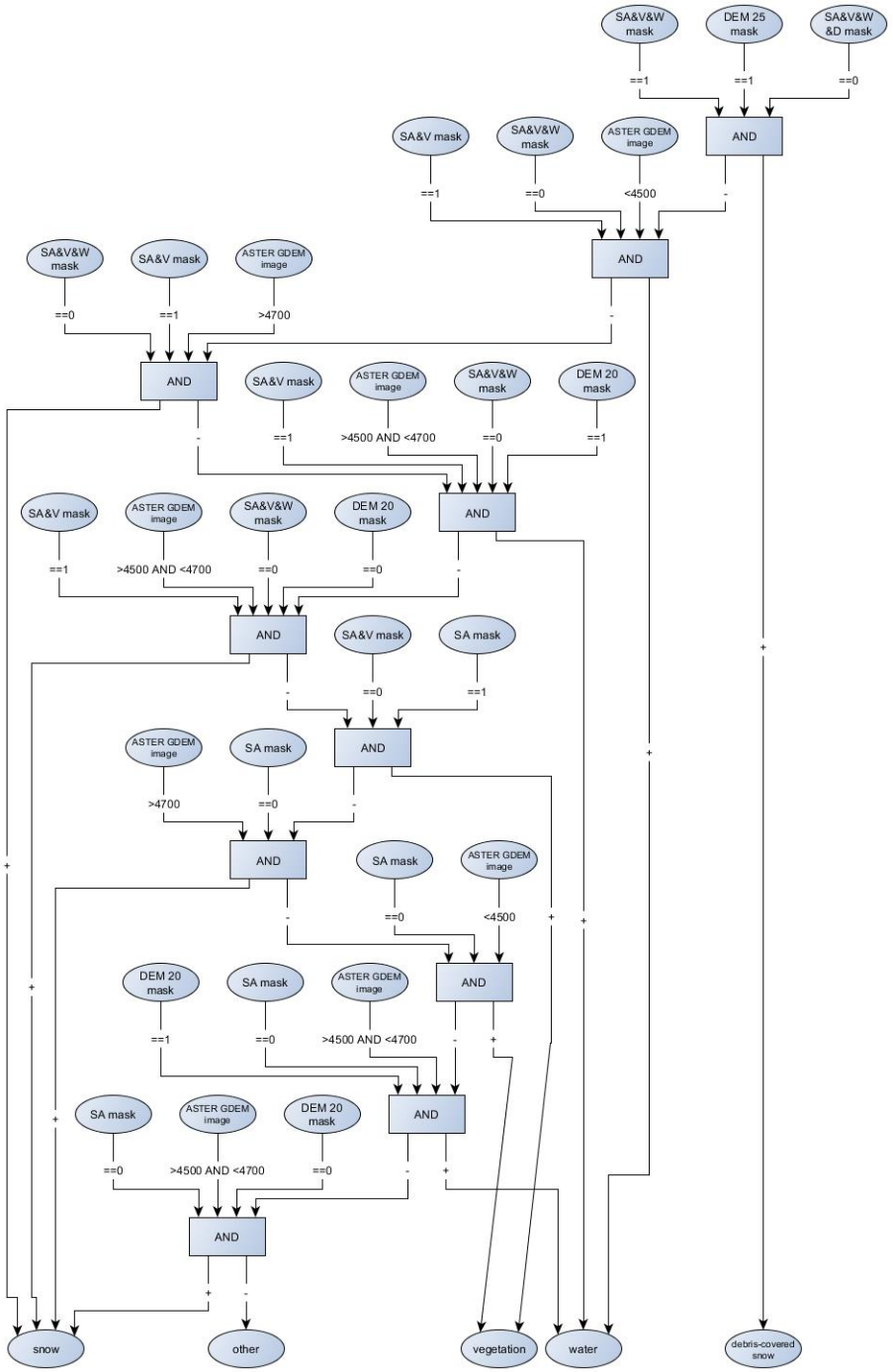

Figure 24: Multiple conditioned expression used in Raster Calculator

This expression includes different conditions, which will be explained in the next section.

- Con(("SA&V&W&D_mask.tif" == 0) & ("SA&V&W_mask.tif" == 1) & ("DEM_25_mask.tif" == 1)),1 – all the pixels included in SA&V&W&D_mask.tif, but not included in SA&V&W_mask.tif, are classified as debris-covered snow areas. The expression is extended with Paul's (2004) criteria, i.e. only areas with a slope not exceeding 25° are evaluated as debris-covered snow (Paul used the criteria of 24°, however 25° was more precise for the purposes of this diploma thesis).
- Con((("SA&V&W_mask.tif" == 0) & ("SA&V_mask.tif" == 1) & ("ASTER_GDEM.tif" < 4500)),2 – all the pixels included in SA&V&W_mask.tif, but not included in SA&V_mask.tif, are classified as water areas. The expression is extended with the altitude criteria, i.e. areas with an altitude lower than 4500 m a.s.l., are evaluated as water areas. This criteria was adopted, because in some cases the basic classification algorithm led to the misclassification on water and snow areas. Areas with an altitude higher than 4500 m a.s.l. will be discussed in the next steps.
- Con((("SA&V&W_mask.tif" == 0) & ("SA&V_mask.tif" == 1) & ("ASTER_GDEM.tif" > 4700)),4 – all the pixels included in SA&V&W_mask.tif, but not included in SA&V_mask.tif, which have a higher altitude than 4700 m a.s.l., are classified as snow areas.
- Con((("SA&V&W_mask.tif" == 0) & ("SA&V_mask.tif" == 1) & ("ASTER_GDEM.tif" > 4500) & ("ASTER_GDEM.tif" < 4700) & ("DEM_20_mask.tif" == 1)),2 – all the pixels included in SA&V&W_mask.tif, but not included in SA&V_mask.tif, which have an altitude between 4500 m a.s.l. and 4700 m a.s.l. and have an aspect lower than 20° (evaluated as flat area), are classified as water areas.
- Con((("SA&V&W_mask.tif" == 0) & ("SA&V_mask.tif" == 1) & ("ASTER_GDEM.tif" > 4500) & ("ASTER_GDEM.tif" < 4700) & ("DEM_20_mask.tif" == 0)),4 – all the pixels included in SA&V&W_mask.tif, but not included in SA&V_mask.tif, which have an altitude between 4500 m a.s.l. and 4700 m a.s.l. and have an aspect higher than 20°, are classified as snow areas.
- Con((("SA&V_mask.tif" == 0) & ("SA_mask.tif" == 1)),3 – all the pixels included in SA&V_mask.tif, but not included in SA_mask.tif, are classified as vegetation areas.
- Con((("SA_mask.tif" == 0) & ("ASTER_GDEM.tif" > 4700)),4 – all the pixels included in SA_mask.tif and having higher altitude than 4700 m a.s.l., are classified as snow areas.

- Con((("SA_mask.tif" == 0) & ("ASTER_GDEM.tif" < 4500)),2 – all the pixels included in SA_mask.tif and having lower altitude than 4500 m a.s.l., are classified as water areas.
- Con((("SA_mask.tif" == 0) & ("ASTER_GDEM.tif" > 4500) & ("ASTER_GDEM.tif" < 4700) & ("DEM_20_mask.tif" == 1)),2 – all the pixels included in SA_mask.tif and having an altitude between 4500 m a.s.l. and 4700 m a.s.l., which have an aspect lower than 20°, are classified as water areas.
- Con((("SA_mask.tif" == 0) & ("ASTER_GDEM.tif" > 4500) & ("ASTER_GDEM.tif" < 4700) & ("DEM_20_mask.tif" == 0)),4 – all the pixels included in SA_mask.tif and having an altitude between 4500 m a.s.l. and 4700 m a.s.l., which have an aspect higher than 20°, are classified as snow areas.
- The rest of the areas is classified as 'Other'.

The full classification algorithm was applied to all of the 29 downloaded and preprocessed Landsat scenes.

3.6.1 ISODATA vs. K-means classification

As indicated in the previous chapter, full ISODATA classification was not applicable to five Landsat scenes. In these cases ISODATA classification resulted in a non-ending cycle and thus had to be interrupted. In these cases, ISODATA classification was replaced by K-means classification for some parts of the classification algorithm:

- In the process of the SA mask creation – Landsat 5 (year 1995), Landsat 8 (years 2013 and 2014)
- In the process of the SA&V mask creation – Landsat 5 (year 1989) and Landsat 8 (year 2014)

Obviously, it was necessary to test, whether the partial K-means classification gives a significantly different result, than the full ISODATA classification. The Landsat 5 scene from the year 1997 was chosen for testing, as this scene was suitable for both classification methods. As shown in Figure 25, both classification methods gave the same results in both full and detailed extent.

Additionally, a correlation matrix between the two classified images was computed using ArcMap Band Collection Statistics Tool (/Spatial Analyst). The statistical calculation gave the same result, i.e. a correlation of +1.0 between the two classified images.

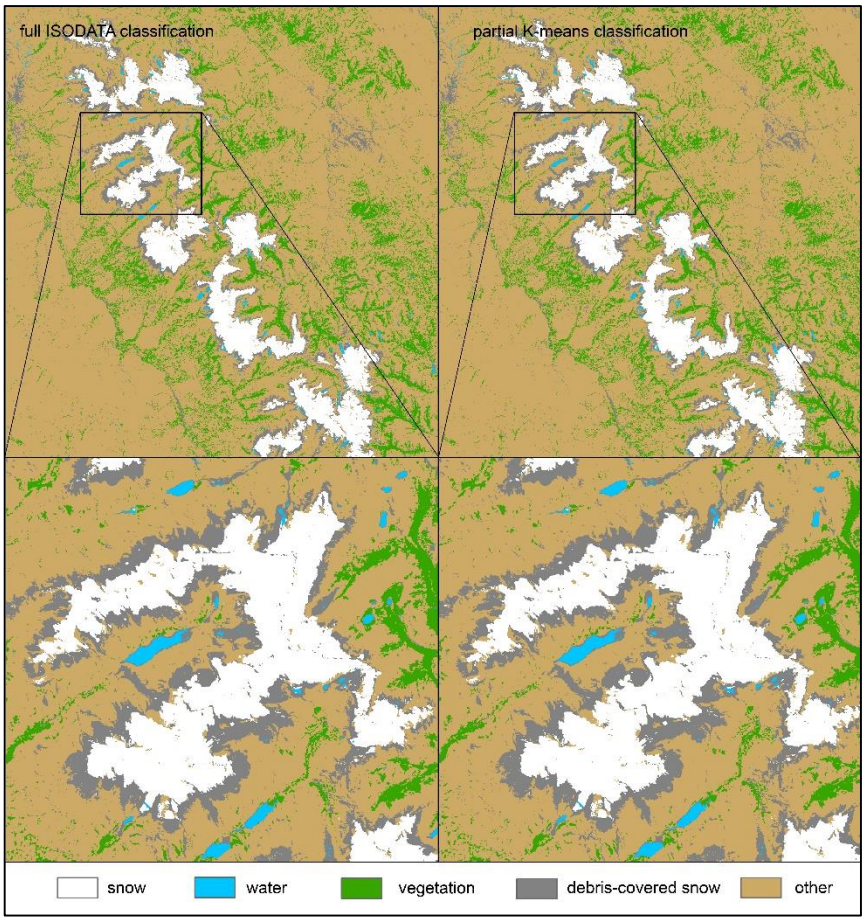

Figure 25: Comparison of full ISODATA classification and partial K-means classification

3.7 Post classification – image filtering

Visual observation of the output images of the classification process discovered, that the final results contain many separated pixels (areas). Because of the easier use in further analyses and easier comparison with results of other works, image filtration has been applied to each classified image using ArcMap Majority Filter (\Spatial Analyst). During the filtration process, two kernel sizes were tested – either with four or with eight neighboring cells. For the purpose of this diploma thesis, the kernel size of eight neighboring cells was used to filter the classified image.

In the next step, the filtered image created by Majority filter had to be verified in order to determine the extent of pixel change between different classes. If the extent of pixel change was significant, it would influence the results of further analyses. The difference between the non-filtered and filtered image was computed using ArcMap Raster Calculator Tool. The pixel values ranged from 0 to 4 (1 – debris-covered snow, 2 – water, 3 – vegetation, 4 – snow, 0 – other) for both images. The mean change between the filtered and non-filtered image was 0,03. This means, that the pixel change after the filtering process was balanced, thus the filtering process had no

significant impact on further analyses. The visual difference between the original and the filtered image is presented in Figure 26.

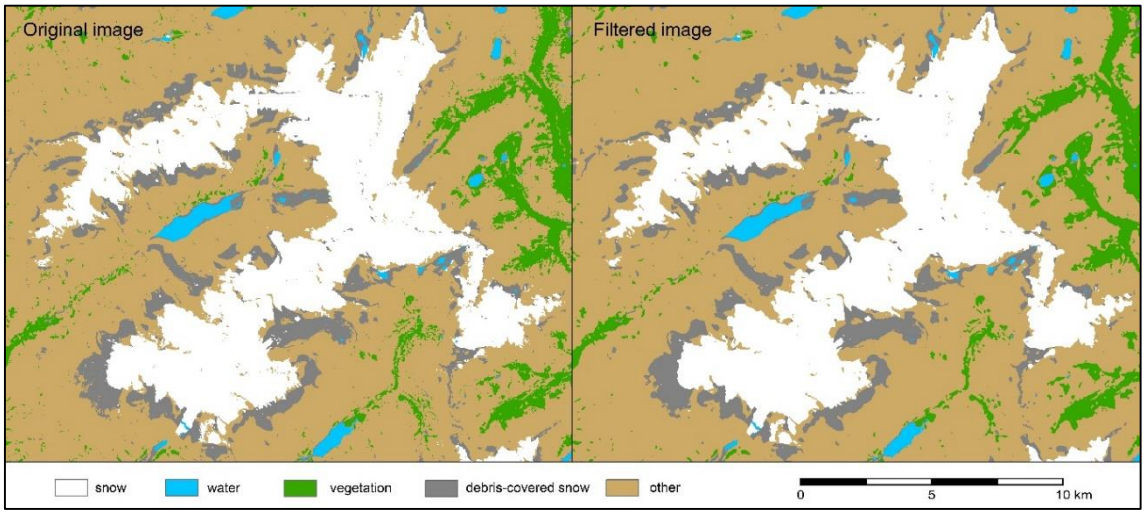

Figure 26: Visual difference between the original and the filtered image

3.8 Detection of the snowline altitude

The next task of this diploma thesis was to calculate the mean snowline altitude in the Cordillera Blanca. According to Paterson (1994), the snowline altitude can be used to determine the equilibrium line altitude (ELA) for temperate glaciers. The mean snowline altitude calculation was completed on two levels, i.e. on mountain and glacier level. This means, that the mean snowline altitude was calculated for three mountains (the Huascarán mountain, the Huandoy mountain and the Santa Cruz mountain) and for eleven glaciers (the Huancotepampa glacier, the Piramide glacier, the Jatunraju glacier, the Huandoy East glacier, the Huandoy South glacier, the Cancahua glacier, the Schneider glacier, the Knizl glacier, the Paccharuri glacier, the Santa Cruz South glacier and the Santa Cruz West glacier). The above listed glaciers were chosen for snowline altitude analysis based on their size, i.e. larger glaciers were preferred to smaller ones, and the size of the debris-cover snow area. The name of the Huancotepampa glacier, the Piramide glacier, the Jatunraju glacier, the Cancahua glacier, the Schneider glacier, the Knizl glacier and the Paccharuri glacier was imported from the GLIMS Glacier Database. On the other hand, the Huandoy East glacier, the Huandoy South glacier, the Santa Cruz South glacier and the Santa Cruz West glacier were named based on their position in the Cordillera Blanca.

The input data comprised 29 classified images from the years 1986 to 2014. The calculation was provided using ArcMap. The full calculation algorithm is shown in the Figure 27.

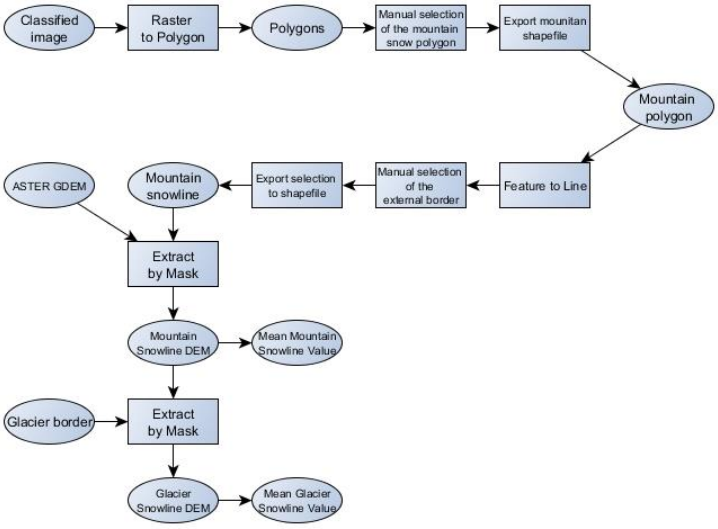

Figure 27: Snowline calculation algorithm

At the first stage of the algorithm, the classified image was converted to polygons using Raster to Polygon Tool (/Conversion). In order to get the most precise results, the 'simplify polygons' option was left unchecked.

At the second stage of the algorithm, the mountain snow polygon (the Huascarán mountain, the Huandoy mountain and the Santa Cruz mountain) was selected and exported as a shapefile. In some cases the snow cover extended to the neighboring mountain (when the snow cover was larger) or consisted of more than one polygon (when the snow cover was smaller). In both cases, the process of merging and splitting was completed later. Examples are shown in Figure 28. Part A (Landsat 4 – year 1989) shows the situation, where the snow polygon is extended from the Huandoy mountain to the neighboring Santa Cruz mountain as the consequence of high snow level. The red circle indicates the area, where the split process had to be done. Part B (Landsat 5 – year 1993) shows the situation, where the Huandoy snow polygon consists of two separated polygons as the result of low snow level. The red circle indicates the area, where the merge process had to be done.

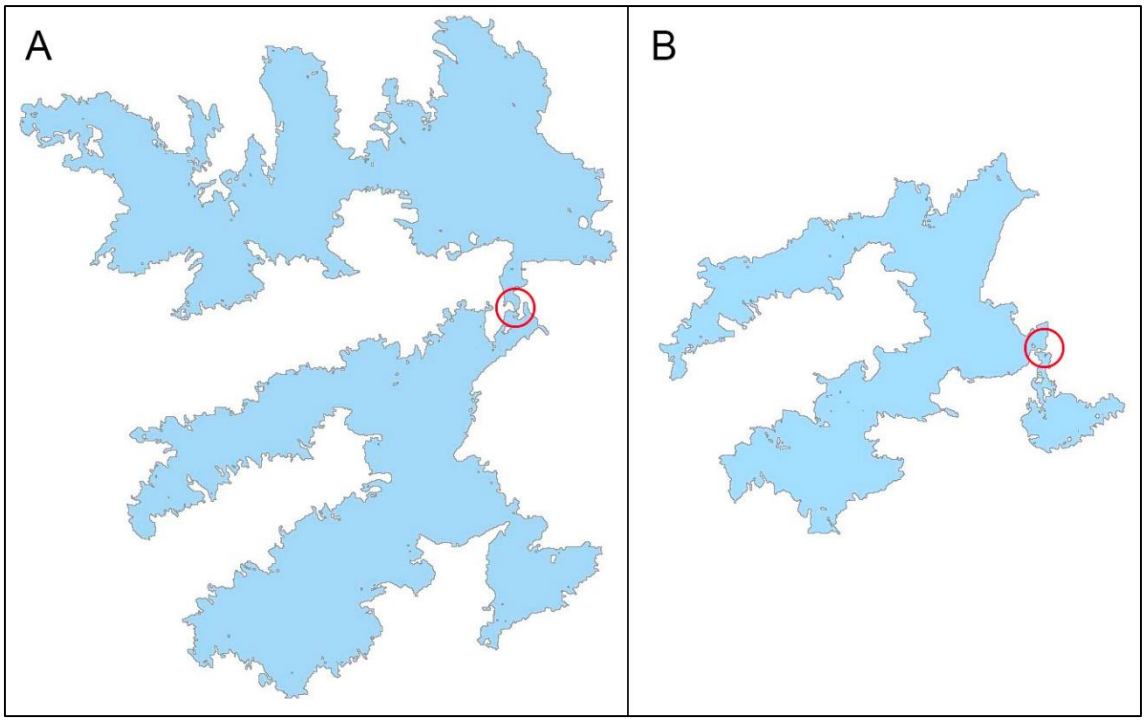

Figure 28: Raster to Polygon Conversion problems

At the third stage, the external border of the polygon representing the snowline had to be selected. To allow for this task, the snow polygon had to be converted to lines using Feature to Line Tool (/Data Management). At this stage, the problems described at the previous stage were solved using Editor Tool. During this process the external border of the polygon was selected and then exported as a shapefile. On the contrary, internal lines were not selected.

At the fourth stage, ASTER GDEM was included to the process. A subset of the DEM representing the Huandoy mountain snowline was created using Extract by Mask Tool (/Spatial Analyst).

At the fifth stage of the algorithm, the average mountain snowline altitude was computed and exported to Excel.

In order to proceed to the final stage, a glacier shapefile had to be created. This process was performed using ArcMap Editing Tool and was based on ArcMap Basemaps. At the final stage, the glacier snowline was created using Extract by Mask Tool. The average glacier snowline altitude was computed and exported to Excel.

The snowline calculation algorithm was then applied to all eleven glaciers, three mountains and 29 Landsat scenes.

3.9 Slope and aspect analysis

The final task of this diploma thesis was to determine the effect of slope and aspect of the terrain on glacier change in the Cordillera Blanca.

The analysis has been conducted on the Huandoy, the Huascarán and the Santa Cruz mountains. The calculation was made using ArcMap, ENVI and Excel. The calculation algorithm is shown in Figure 29.

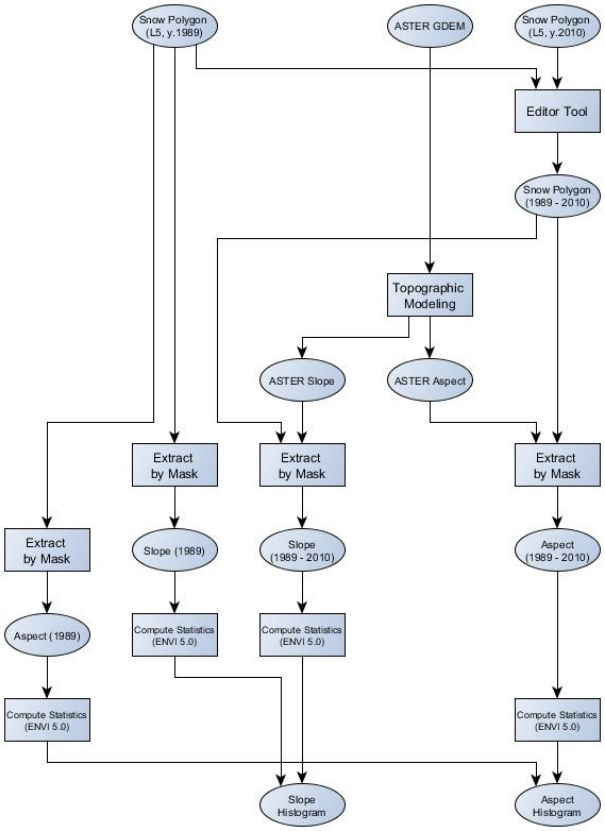

Figure 29: Slope and aspect analysis algorithm

The first input data to the algorithm was the ASTER digital elevation model. This was used to calculate the slope image (ASTER Slope) and the aspect image (ASTER Aspect) in the Cordillera Blanca using ENVI Topographic Modelling Tool.

In addition to the above data, snow polygons of the mountain areas from the previous snowline calculation algorithm were imported to the slope and aspect analysis algorithm. Two scenes were selected to calculate the area of glacier change in the observed period of time (from 1987 to 2014). Landsat 5 scenes from the years 1989 and 2010 were selected on the basis of previous mean snowline analysis. The subtraction of the two polygons (Snow Polygon (1989 minus 2010)) has been created using ArcMap Editor Tool.

The slope image of the changed area (Slope (1989 minus 2010)) has been computed through the ASTER Slope image and the Snow polygon (1989 minus 2010) using ArcMap Extract by Mask Tool. In the following step, statistical characteristics of the Slope (1989 minus 2010) image have been computed using ENVI Compute Statistics Tool (\Statistics).

The statistical characteristics were used to create a histogram in Excel. If the number of pixels for each particular slope of the Slope (1989 minus 2010) image was considered, the histogram would not give relevant results. To this end, the number of pixels for each particular slope of the Slope (1989 minus 2010) image needs to be divided by the corresponding number of pixels of the Slope 1989 image, which has been created using ASTER Slope and Snow Polygon 1989. The histogram shows this ratio depending on the slope (in 5 degree intervals).

The same process has been applied to aspect images. The final aspect histograms show the aspect ratio depending on the 4 (north, east, south and west) and 8 (north, northeast, east, southeast, south, southwest, west and northwest) cardinal directions.

Additionally, the growth of the snow area between the years 1989 and 2010 was computed (Snow Polygon (2010 minus 1989)). In view of the fact, that the number of pixels represented in this area was low, it was not suitable for slope and aspect analyses.

4 RESULTS

In this chapter, the results of this diploma thesis will be presented. The first part of the chapter will include characteristics of the classification of land cover in the Cordillera Blanca, i.e. accuracy of the classification and snow area changes between the classified Landsat images from various years. In the second part of the chapter, the mean snowline altitude change will be presented in different parts of the Cordillera Blanca. Finally, the results of the slope and aspect analyses will be shown. The results will be presented in tables, charts and maps. Due to the relatively large amount of outputs, only result from Huandoy mountain will be presented in the text. Remaining outputs can be found in the appendices.

4.1 Classification of land cover in the Cordillera Blanca

The first task of this diploma thesis was to create a semi-automatic classification algorithm to classify several types of land cover in the Cordillera Blanca. Several classification methods and threshold values were tested. The classification algorithm is described in Chapter 3.6.

4.1.1 Classification accuracy

Classification accuracy has been tested by comparing the classification results with GLIMS Glacier Database shapefiles downloaded via GLIMS Global Glacier Viewer. Landsat 5 classified images from the years 2003 and 2005 were chosen for comparison, as the metadata files of the GLIMS Glacier Database shapefile showed, that the GLIMS analyses of the Cordillera Blanca were provided based on SPOT images from 2003 and ASTER images from 2005. The two GLIMS polygons are slightly different. Figures 30 and 31 show visual differences between the classified Landsat images and the GLIMS Glacier Database polygon borders in the Huascarán mountain.

Further, the snow and debris-covered snow area comparison between the classified image and the GLIMS Glacier Database has been computed. Unfortunately, it was not possible to compute the vegetation and water area comparison, as the GLIMS Glacier Database does not contain vegetation classification and water classification is limited only for certain lakes. The area differences are represented in Table 7.

Table 7: Comparison of snow and debris-covered snow areas in classified Landsat 5 images and the GLIMS Glacier Database

	2003		2005	
	Landsat 5	GLIMS	Landsat 5	GLIMS
snow area [km^2]	483,00	427,68	454,45	402,00
debris-covered snow area [km^2]	105,80	15,98	105,10	13,66

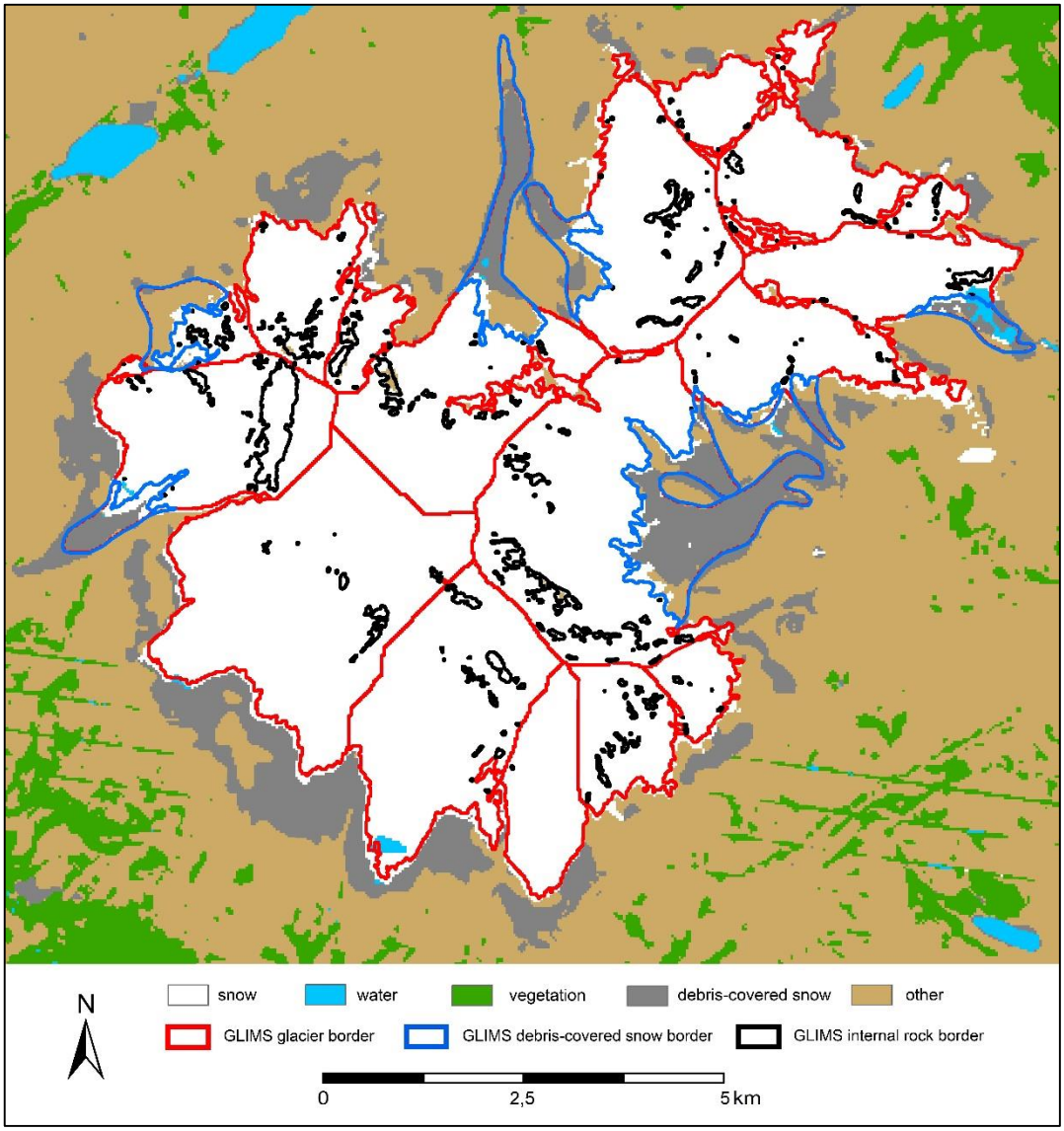

Figure 30: Comparison of the Landsat 5 classified image from the year 2003 and the GLIMS Glacier Database borders from the year 2003

In comparison to the GLIMS Glacier Database, the snow area in the classified Landsat 5 image is larger by 12,94 % and 13,05 % in the years 2003 and 2005, respectively.

The difference in the debris-covered areas is significant in both cases. As it is noticeable from Figures 30 and 31, the GLIMS Glacier Database contains only debris-covered snow areas, which are strictly connected to the largest glaciers in the Cordillera Blanca. On the other hand, the classification provided in this diploma thesis detected all of the debris-covered snow areas. The differences among the results can be explained by methodology differences.

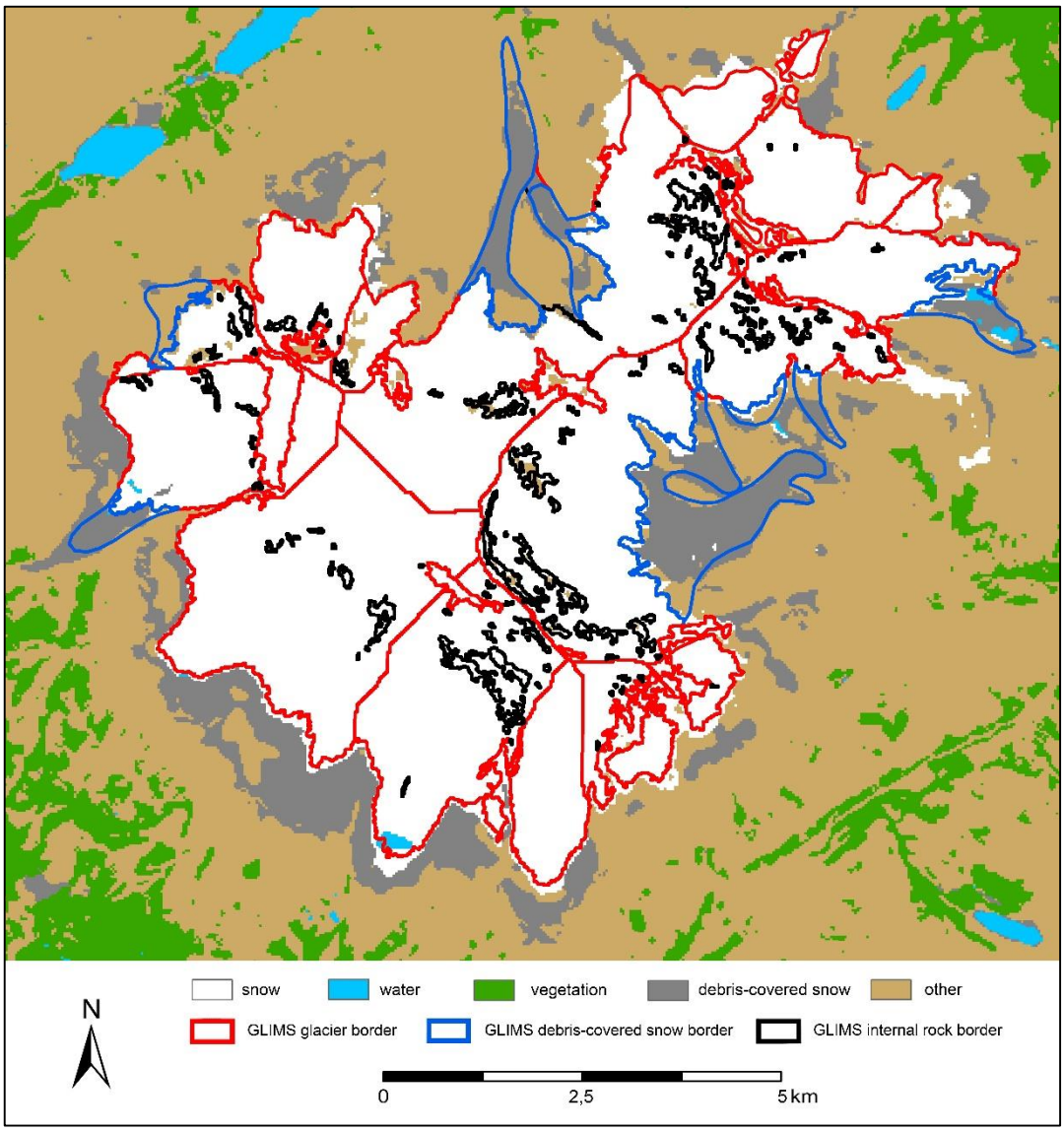

Figure 31: Comparison of the Landsat 5 classified image from the year 2005 and the GLIMS Glacier Database borders from the year 2005

Additionally, the classification results have been compared with field measured data provided by Adam Emmer, MSc. from the period 2012 to 2015. The locations of the sample points are presented in Figure 32. Unfortunately, the number of sample points is very low (only 45 measured points). Although from statistical point of view such a low number of field data is not ideal for computing classification accuracy, this option has been the only available source of field

data comparison. The measured points have been compared with the classified Landsat 5 image from 2010, as this image had the lowest cloud cover in the period from 2010 to 2014. Full comparison is presented in Appendices 10 and 11. The comparison gave the accuracy of 55%. This low accuracy can be explained by several reasons.

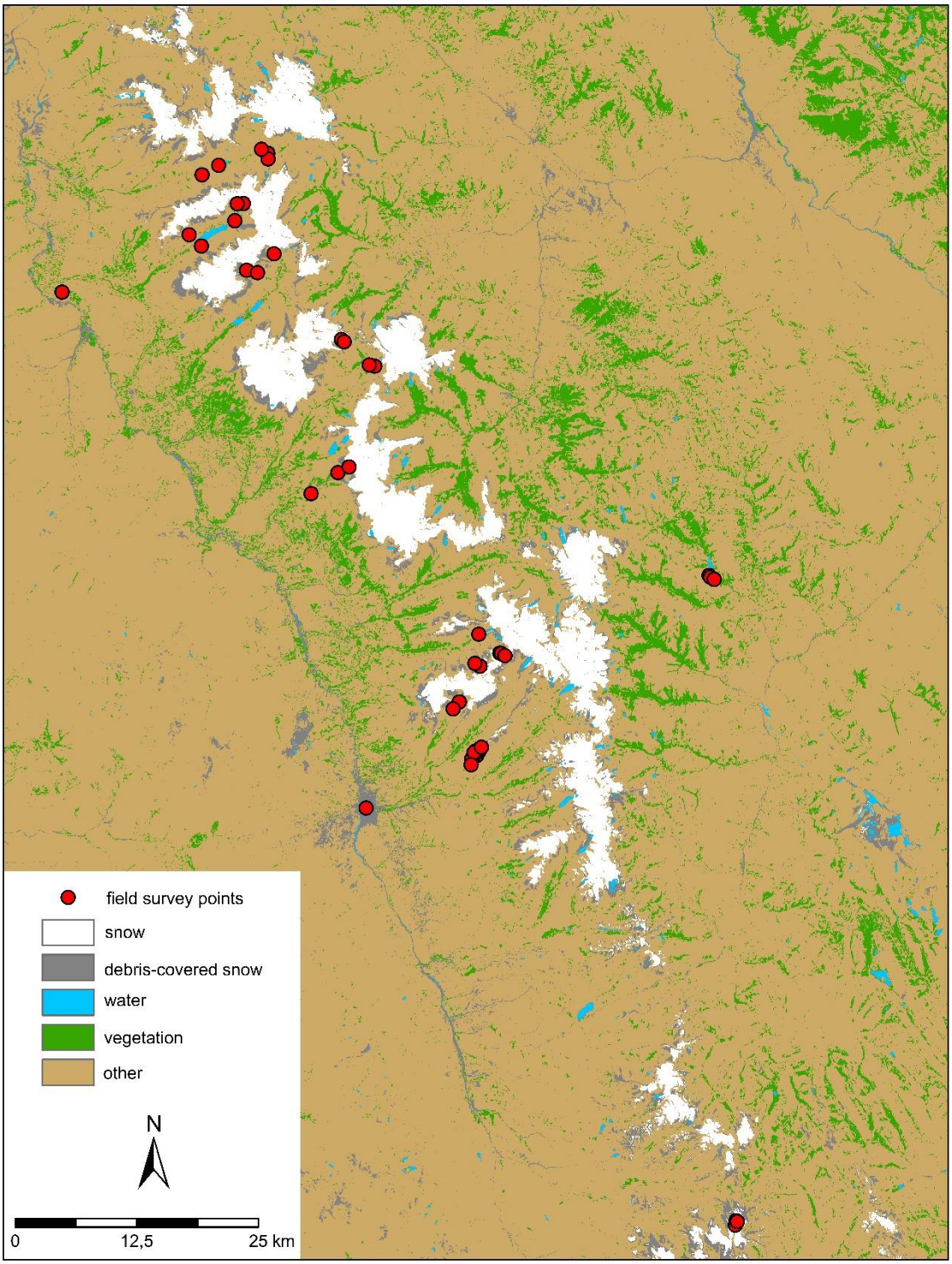

Figure 32: Distribution of field survey points from the period 2012 to 2015

Firstly, points 25 and 26 are situated in urban areas. The classification algorithm has not been set to classify this type of land cover. Similar spectral properties cause, that urban areas could have been misclassified as debris covered areas. Secondly, in most of the cases, 'debris-covered snow' and 'other' have been misclassified, i.e. debris fans and screes described by Emmer as 'other', have been classified as 'debris-covered snow'. Still, it is hard to detect from satellite images, whether there is snow or rock under the debris layer. Thirdly, point 10 represents a young proglacial lake. Its small extent could have caused its misclassification as snow cover. On the other hand, it is important to note, that all of the points measured by Emmer as snow area, have been classified correctly.

4.1.2 Classification results

The semi-automatic classification algorithm has been applied to all of the 29 Landsat scenes between years 1987 and 2014. Maps created from the classified image from the year 1987 for the Cordillera Blanca, the Huandoy mountain, the Huascarán mountain and the Santa Cruz mountain, are presented in Figure 33 and Appendices 12, 13 and 14. All of the classified Landsat images are available on the digital disk attached to this diploma thesis.

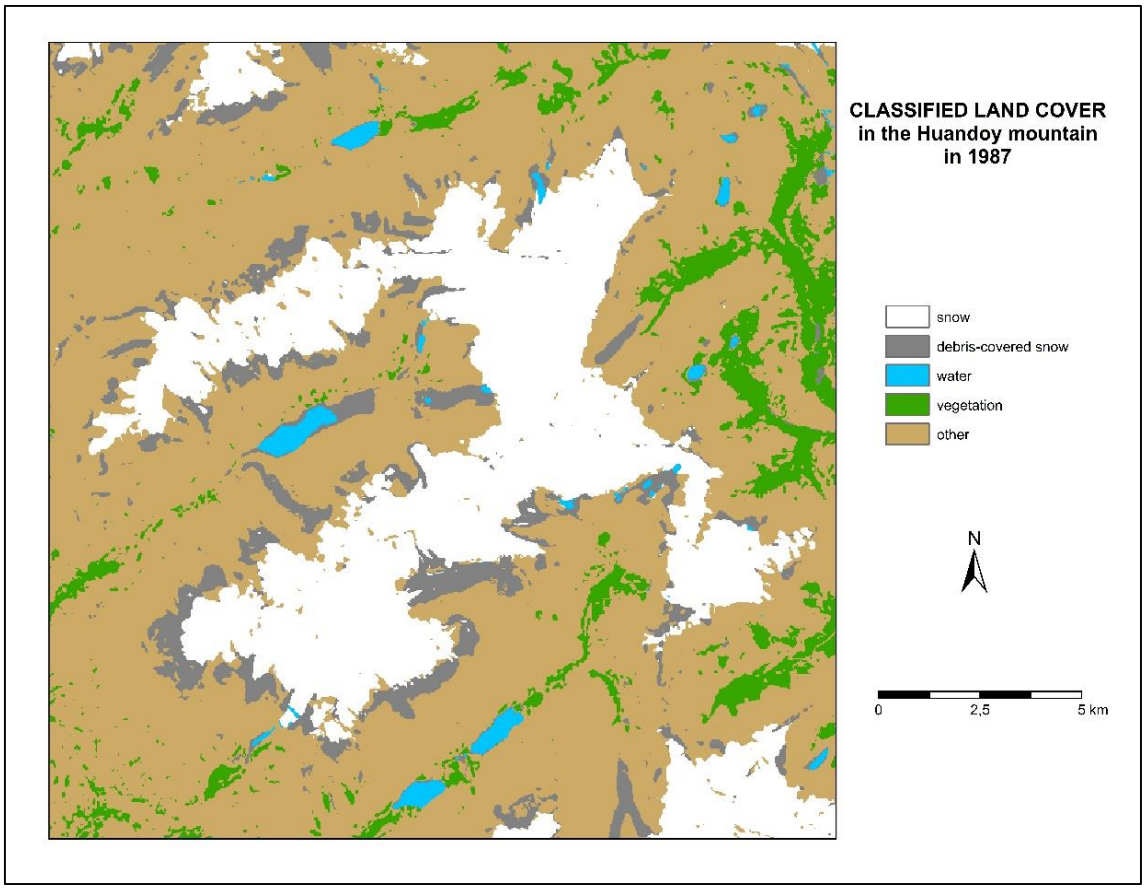

Figure 33: Classified land cover in the Huandoy mountain in 1987

Further, the snow and debris-covered snow area change has been calculated. Visual representation of the results is shown in Figures 34 and 35, whereas numeric results are presented in Appendix 15.

In the period from 1987 to 2014, the snow area varied from 433,71 km^2 to 566,43 km^2. With respect to the misclassification caused by the cloud cover in the downloaded Landsat 5 images from the years 1989 and 2011, these results (718,72 km^2 for the year 1989 and 728,93 km^2 for the year 2011) were not used. In the period from 1987 to 2014, the snow area change had a negative trend.

In the period from 1987 to 2014, the debris-covered snow area varied from 91,06 km^2 to 178,53 km^2. With respect to the misclassification caused by the cloud cover in the downloaded Landsat 5 image from the year 1991, this result (284,59 km^2) was not used. In the period from 1987 to 2014, the debris-covered snow area change had a positive trend.

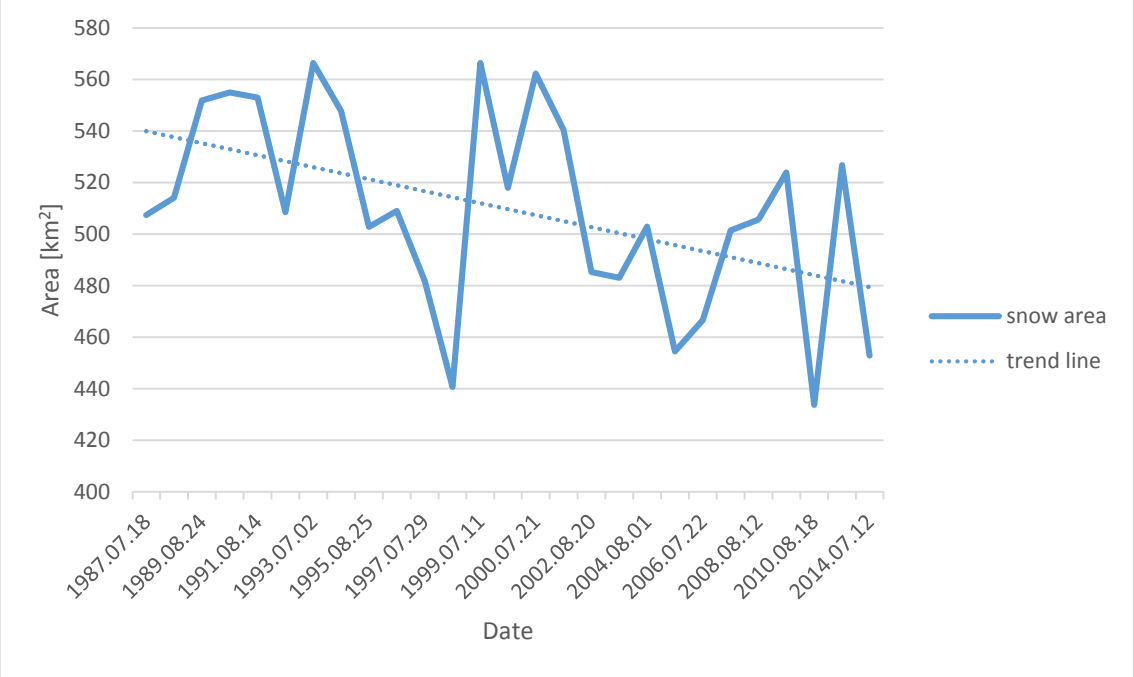

Figure 34: Snow area change in the Cordillera Blanca

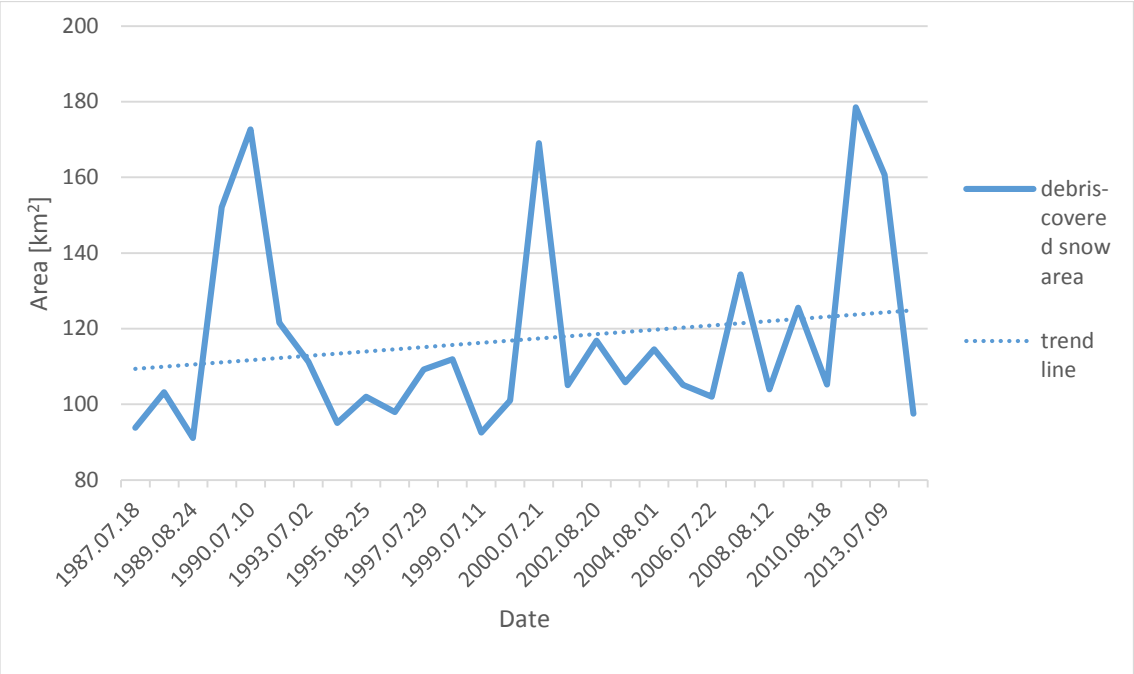

Figure 35: Debris-covered snow area change in the Cordillera Blanca

4.2 Mean snowline altitude change in the Cordillera Blanca

The second task of this diploma thesis was to calculate the mean snowline altitude change in the Cordillera Blanca. The calculation algorithm has already been described in Chapter 3.8. The calculation algorithm has been applied to all of the eleven glaciers, three mountains and 29 Landsat scenes. Maps showing the snowline change in the eleven glaciers for the selected years (1987, 1990, 1995, 2000, 2005, 2010 and 2014) are presented in Figure 36 and Appendices 16 to 25. The snowline shapefiles are available on the digital disk attached to this diploma thesis. Visual representation of the results is shown in Figures 37 to 40. Numeric results are presented in Appendices 26 to 29.

As it has been mentioned earlier, the Landsat 4 image from 1989 had a high cloud cover, which led to snow area misclassification. This resulted in an extremely low mean snowline altitude for all of the Cordillera Blanca. As a consequence, the Landsat 4 image from 1989 has been left out from the description of the calculation results.

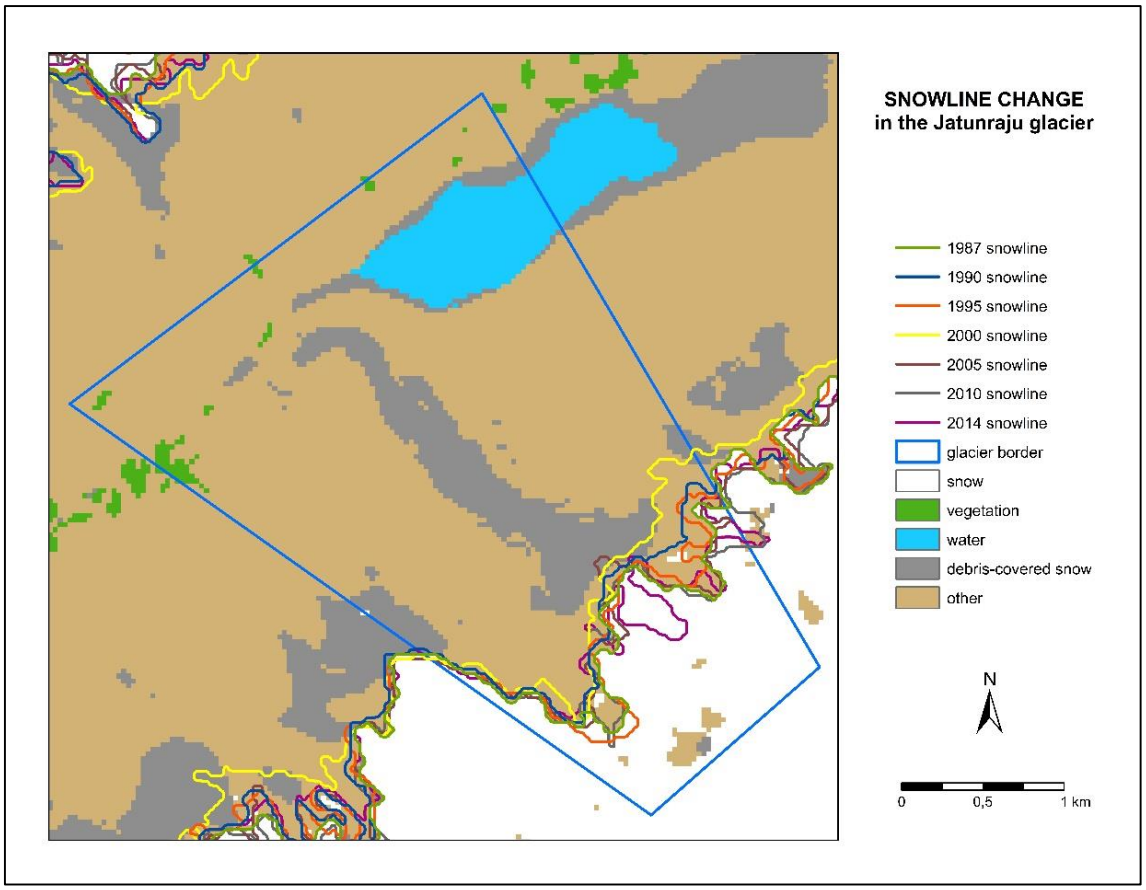

Figure 36: Snowline change in the Jatunraju glacier

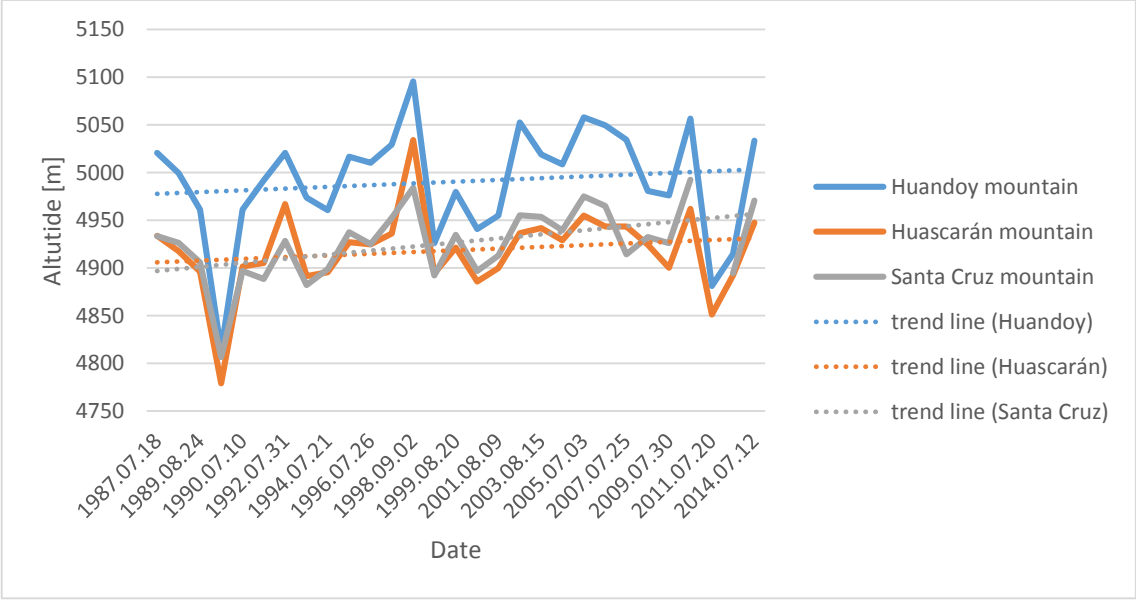

Figure 37: Mean snowline altitude change in the Cordillera Blanca

Among the selected mountain ranges, the highest mean snowline altitude value was reached in the Huandoy mountain. With respect to the high cloud cover in the Landsat 5 image from 2011, this image has not been used for mean snowline altitude calculation in the Santa Cruz mountain. For the remaining two mountains, the calculated mean snowline altitude for this year was low, but acceptable. In the period from 1987 to 2014, the computed mean snowline altitude values for the three mountains varied from 4851,4 m to 5095,6 m. In the period from 1987 to 2014, the mean snowline altitude change had a positive trend for all of the three mountains. No north-south location differences were discovered with respect to the three monitored mountains.

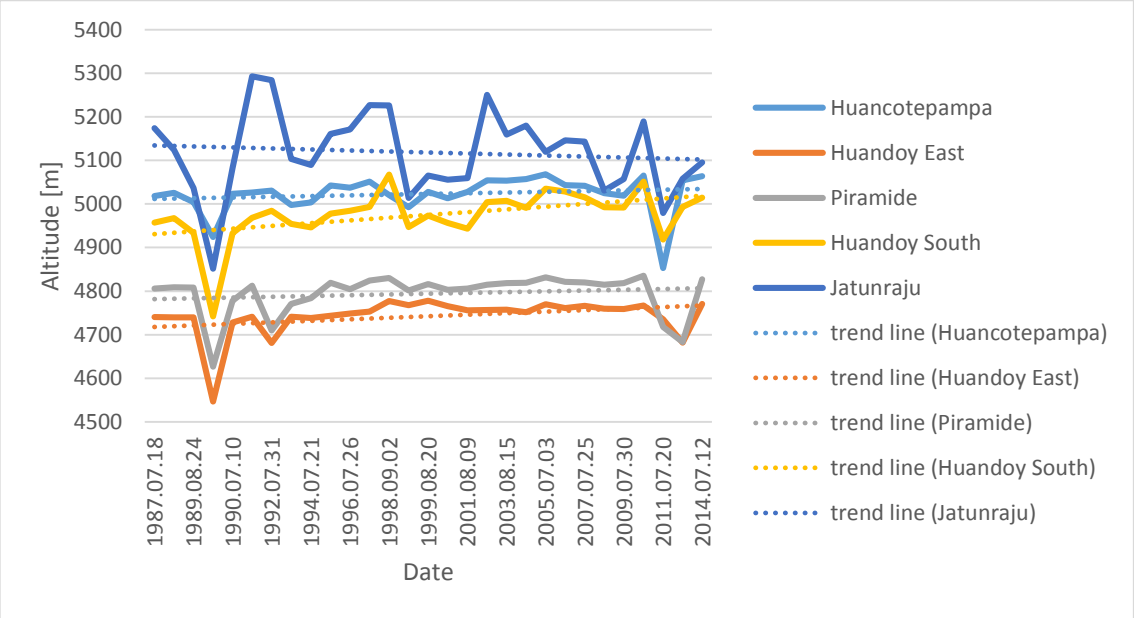

Figure 38: Mean snowline altitude change in the glaciers of the Huandoy mountain

Among the glaciers in the Huandoy mountain, the highest mean snowline altitude value was reached in the Jatunraju glacier. In the period from 1987 to 2014, the Jatunraju glacier has a bigger variability of mean snowline altitudes, compared to other glaciers in the Huandoy mountain. The mean snowline altitude change had a positive trend for the glaciers in the Huandoy mountain, except of the Jatunraju glacier.

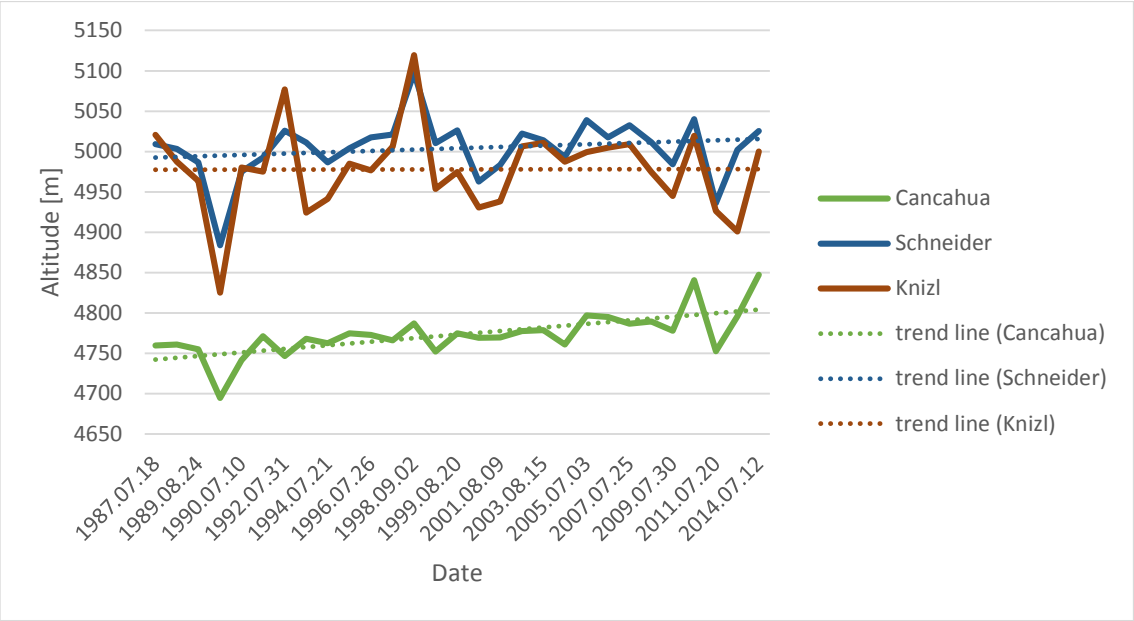

Figure 39: Mean snowline altitude change in the glaciers of the Huascarán mountain

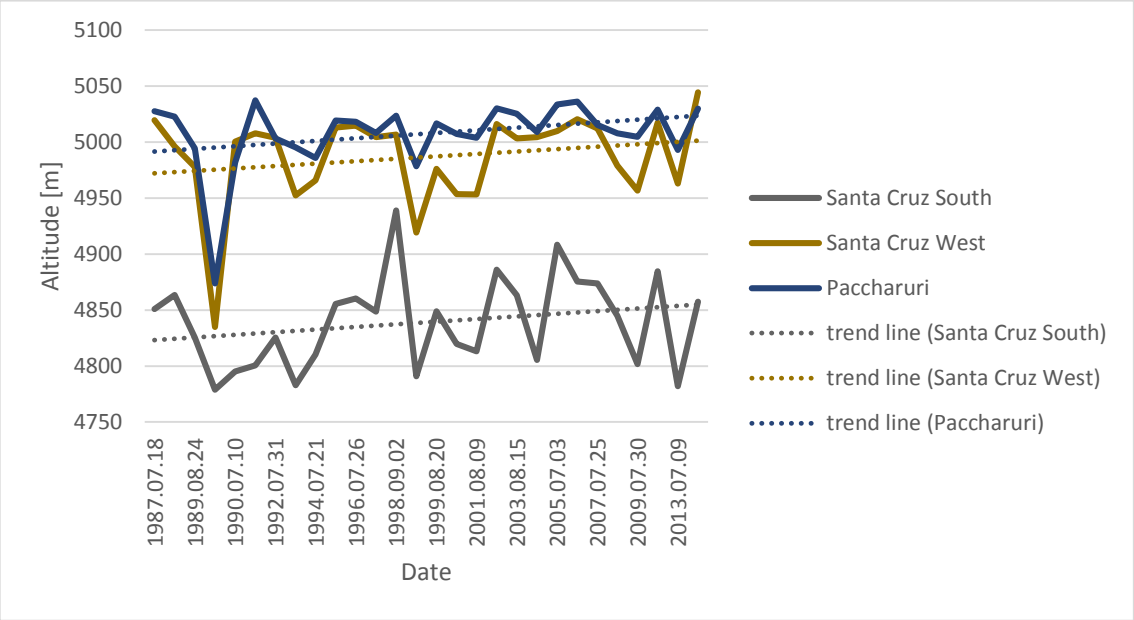

Figure 40: Mean snowline altitude change in the glaciers of the Santa Cruz mountain

In the Huascarán mountain, the mean snowline altitude change had a positive trend for the Schneider glacier and the Cancahua glacier. On the other hand, neither positive, nor negative trend was shown for the Knizl glacier. In the monitored time period, the Cancahua glacier had significantly lower mean snowline altitude values, than the Schneider and the Knizl glaciers.

Among the three glaciers in the Santa Cruz mountain, the mean snowline altitude change had a positive trend during the monitored time period. The Santa Cruz South glacier had

significantly lower mean snowline altitude values, than the Santa Cruz West and the Paccharuri glaciers.

4.3 Slope and aspect analysis of the glacier change in the Cordillera Blanca

Lastly, the slope and aspect analysis of the glacier change has been computed. The calculation algorithm has already been described in Chapter 3.9. The algorithm has been applied to all of the three mountains and 29 Landsat scenes. Glacier change means the difference in the snow area between the years 1989 and 2010. For glacier loss, both detailed computation and visual representation has been created. In the case of glacier gain, only visual representation was suitable, as the extent of glacier gain was very limited. Maps showing glacier change depending on slope in the three monitored mountains are presented in Figure 41 and Appendices 30 and 31. Maps showing glacier change depending on aspect in the three mountains are presented in Figure 42 and Appendices 36 and 37. All of the computed shapefiles are available on the digital disk attached to this diploma thesis. Visual representation of the results is shown in Figures 43 to 45 and Appendices 32 to 34 and 38 to 43. Numeric results are presented in Appendices 35 and 44.

Generally, the relative number of changed pixels (see Chapter 3.9) varied from 11,15 % to 32,28 % in the Cordillera Blanca. The highest value of the relative number of changed pixels was in the interval 60,0-64,9 degrees. This means, that between 1989 and 2010, 32,28 % of the snow area with a slope between 60,0 and 64,9 degrees has changed.

The glacier change depending on slope in the Huandoy and Huascarán mountains shows almost the same trend. The relative numbers of changed pixels are higher for higher slope intervals in both mountains. In the case of the Santa Cruz mountain, the relative numbers of changed pixels are higher for mid-range slope intervals and lower for extreme slope intervals.

Generally, there is no dominant cardinal direction influence on glacier change in the Cordillera Blanca. The relative numbers of changed pixels are roughly the same for all of the 4 (and of the 8) cardinal directions. In the Huandoy and Santa Cruz mountains, the impact of the south direction on glacier change is slightly dominant. In the Huascarán mountain, the impact of the north-east direction is slightly dominant.

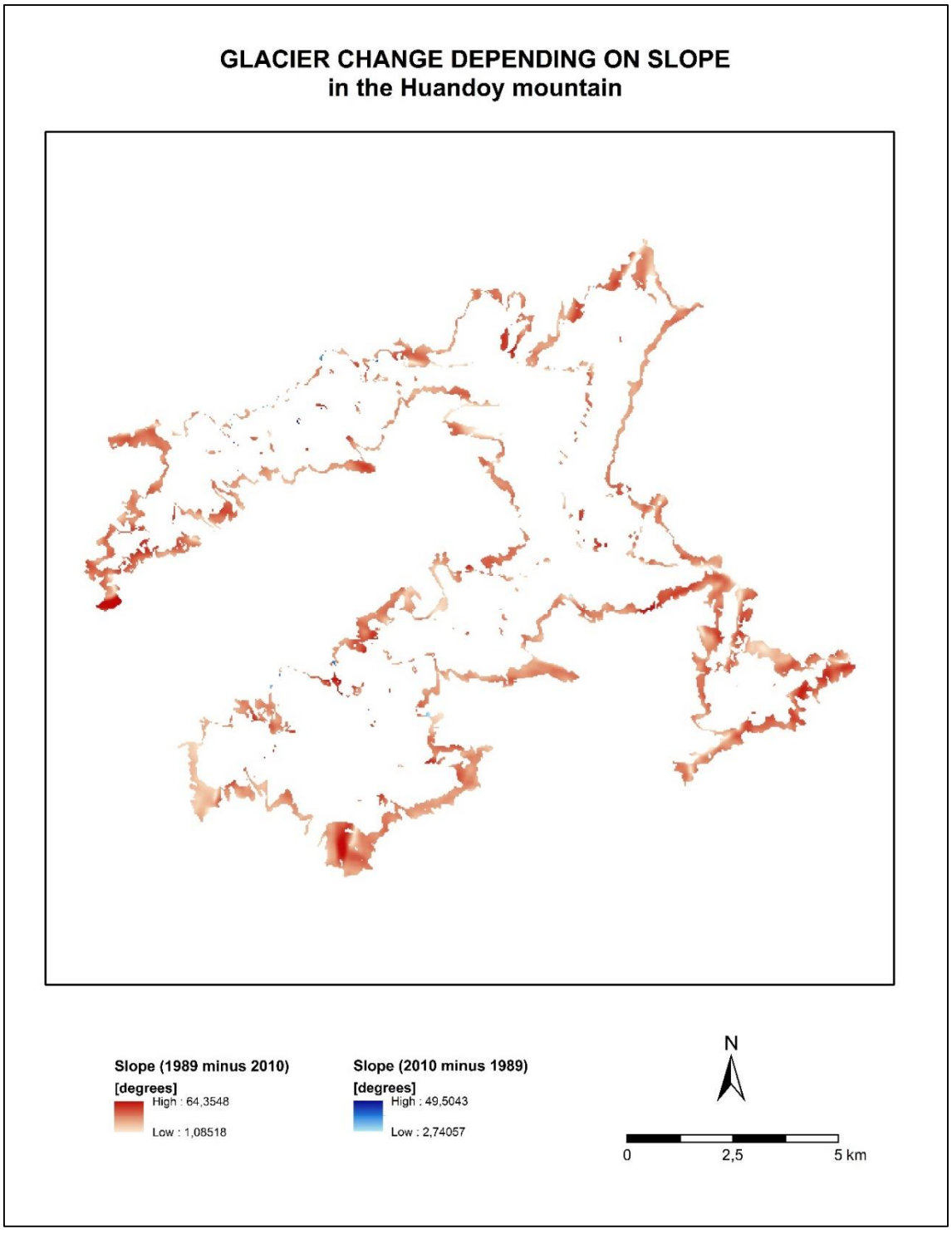

Figure 41: Glacier change depending on slope in the Huandoy mountain

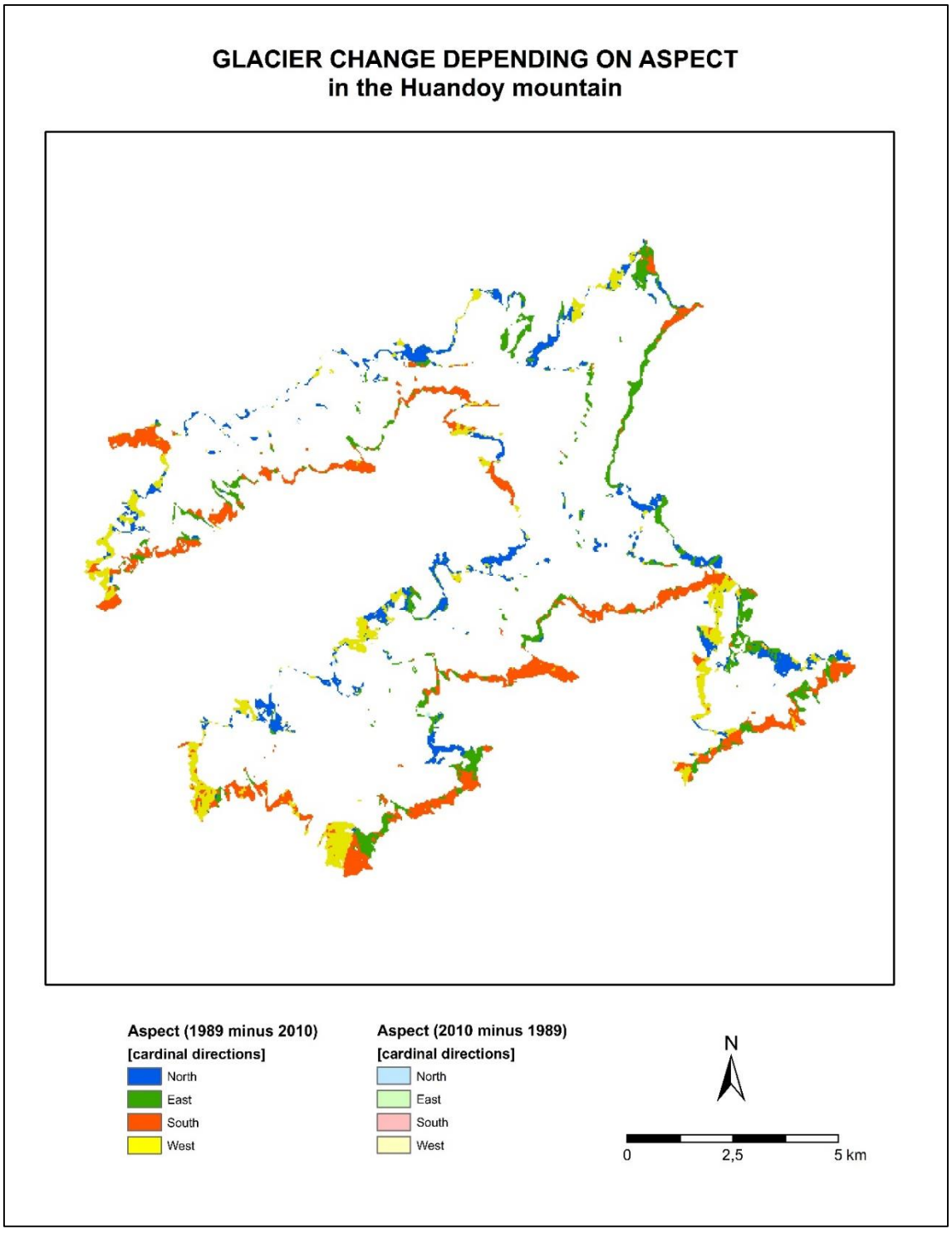

Figure 42: Glacier change depending on aspect in the Huandoy mountain

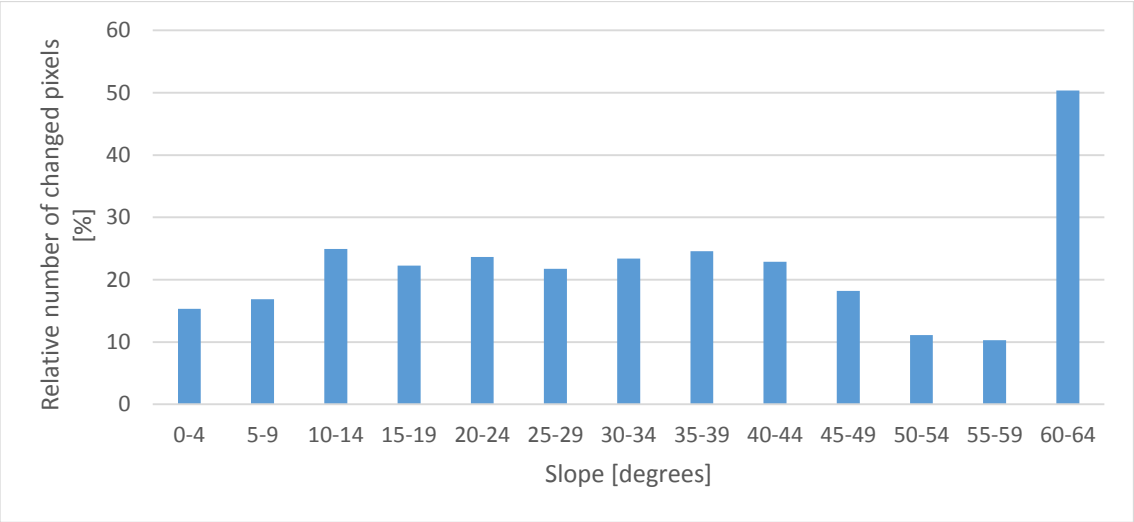

Figure 43: Glacier change depending on slope in the Huandoy mountain

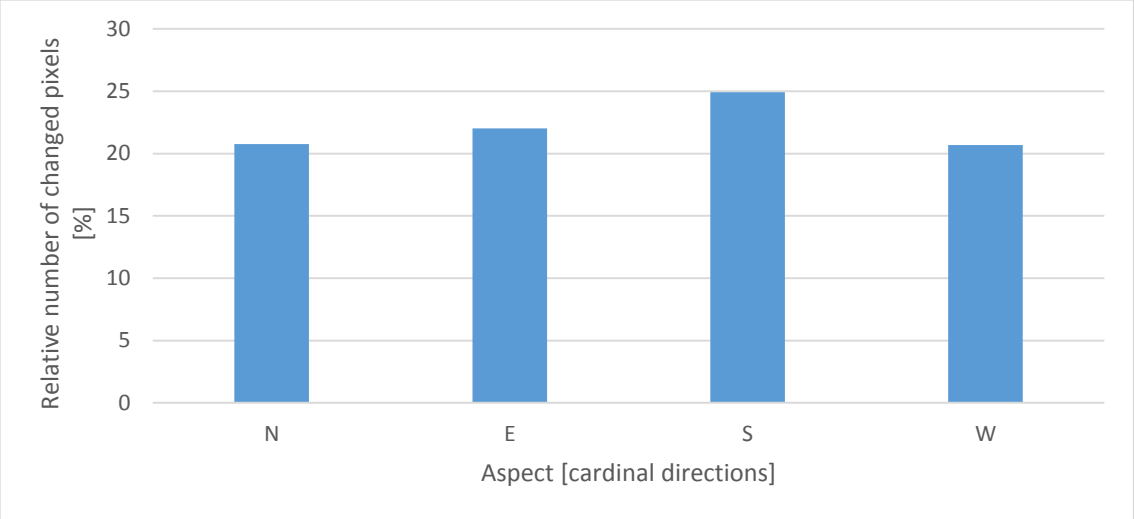

Figure 44: Glacier change depending on aspect (4 cardinal directions) in the Huandoy mountain

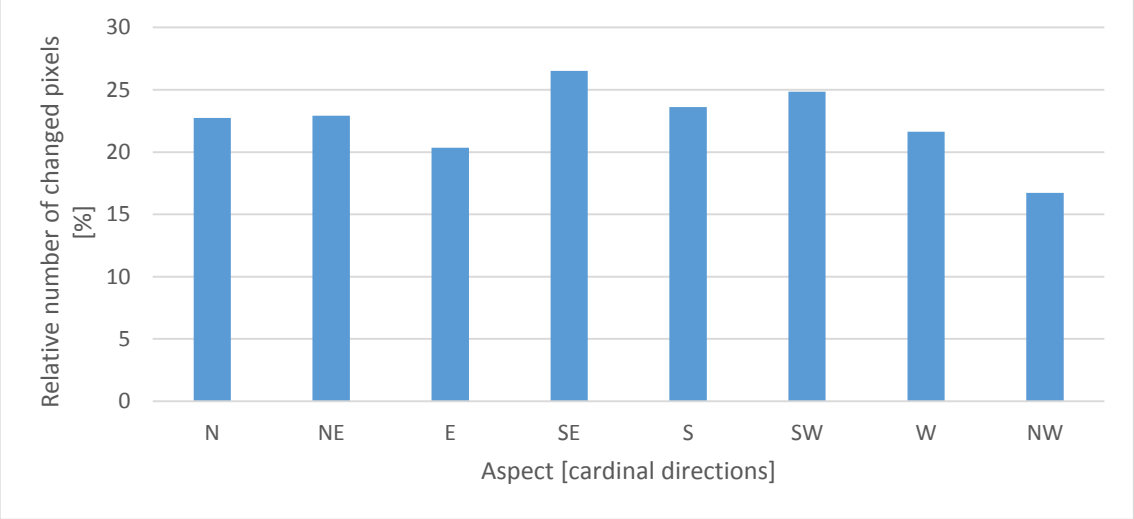

Figure 45: Glacier change depending on aspect (8 cardinal directions) in the Huandoy mountain

5 DISCUSSION

The first task of this diploma thesis was to select and download the most suitable satellite images for glacier change monitoring. The study area has been selected in collaboration with the Department of Physical Geography and Geoecology of the Faculty of Science of the Charles University in Prague. The selected glaciers have been chosen based on the extent of debris-covered snow area. The Landsat program has been chosen as the source of satellite images in regard of its main advantages, i.e. easy data acquisition and zero cost. On the other hand, the quality of the Landsat data is limited by its lower spatial resolution. Although spatial resolution of 30 m is not ideal for monitoring glacier changes, it is still the most admissible solution at the level of a master thesis.

The Landsat data have been downloaded via USGS Earth Explorer. In order to download only usable scenes, two main criteria had to be set. The first criteria involved downloading scenes at the end of the ablation season, i.e. from July to September. This criteria was essential, as the snow area in the Cordillera Blanca is the lowest at this time. In addition to this, Paterson (1994) says, that in case of temperate glaciers, the snowline altitude is roughly equal to the equilibrium line altitude (ELA) at the end of the dry season. The second criteria involved downloading scenes with the lowest possible cloud cover. The goal was to download scenes from the widest time period with one scene per year density. All of the search results have been visually checked by RGB preview in the Earth Explorer. If two or more scenes were suitable from one year, the one with the lowest cloud cover has been chosen. For years 1989 and 1999 two scenes per year have been downloaded due to different Landsat scanner generations. Unfortunately, due to the 16 days scanning repeat cycle of Landsat 5 and 7, no suitable scene was available for the year 2012. Some of the downloaded images were not completely cloud cover free, nevertheless, they could be used for glacier change monitoring in certain parts of the Cordillera Blanca. Finally, 29 scenes were acceptable to download with different usability caused by various cloud cover.

The next task of this diploma thesis was to preprocess Landsat scenes for further analysis. As regards atmospheric correction, it has been discovered that the available tools for this task were either too simple (i.e. calculated atmospheric correction only from the observed pixel spectra in the scene) or too complicated (i.e. required detailed weather information in the observed location, which was not available). Finally, it has been decided, that Landsat CDR scenes with the atmospheric correction provided by USGS will be downloaded. In addition to the atmospheric correction, topographic correction should be applied to scenes in order to eliminate illumination differences caused by terrain in the high mountain areas. Unfortunately, neither high resolution, nor accurate digital elevation models are available in the Cordillera Blanca, which would be essential to complete this task. As discussed in Chapter 3.2, the available SRTM model had many

‘no data’ errors in the Cordillera Blanca. In order to solve this problem, it has been decided to expend the further classification algorithm to eliminate topographic effects in the snow areas of the Cordillera Blanca.

The last part of the preprocessing involved computing scene correlation and completing image coregistration. The correlation has been computed in two ways: firstly, by the ArcMap Band Collection Statistics Tool, secondly, using a Matlab algorithm. The computation using ArcMap Band Collection Statistics Tool included full image comparison, whereas the Matlab algorithm consisted of image comparison based on control points. As it has been discovered, correlation results computed using the ArcMap Band Collection Statistics Tool could have been affected by cloud cover and variable snow, vegetation and water areas. Both methods revealed geometric distortion of the Landsat 7 scene from 1999, which has been adjusted using ENVI Registration: Image to image Tool with the Landsat 5 base image from 1999. Correlation and median distance values computed after completing image coregistration showed, that geometric distortion has been eliminated.

In order to fulfill the aims of this diploma thesis, digital elevation model of the Cordillera Blanca was required beyond the Landsat scenes. The ASTER GDEM 2 has been downloaded via USGS Earth Explorer. The ASTER digital elevation model has the same benefits, as the Landsat data, i.e. cost and accessibility. Similarly, its main disadvantages are the lack of high accuracy and low spatial resolution. It is important to note, that this option is still the best available solution at the level of a master thesis. Two ASTER GDEM scenes needed to be downloaded in order to cover the whole Cordillera Blanca. These scenes had to be merged and then reprojected to UTM. After creating a subset of the Cordillera Blanca, the digital elevation model has been completed for further analysis.

In order to create a semi-automatic classification algorithm it was necessary to discover differences between spectral properties of different land cover types. The reason for this is that the semi-automatic classification algorithm requires detecting and setting up threshold values. As described in Chapter 2.2.4., several studies (e.g. Hendriks and Pellikka, 2007 and Paul et al., 2004) contained NDVI, NDWI and NDSI indexes as an input for land cover classification. Accordingly, these indexes have been computed and used for spectral analysis for the purposes of this diploma thesis. This process has been completed both for Landsat 5 (with the same band distribution as Landsat 4 and 7) and Landsat 8 scenes using ENVI 5.0 software. Several Regions of Interest have been selected for different types of land cover. On the basis of their spectral properties, spectral curves of the selected land cover types have been created using ENVI and Excel. Visual and numerical results revealed the means, how each of the selected land cover types can be separated. This process is described in detail in Chapter 3.5. In this part of the process, the illumination

differences caused by the lack of topographic correction have been corrected by observing snow separately in illuminated and in shadowed areas.

The main goal of this diploma thesis was to create a semi-automatic classification algorithm for classifying snow, water, vegetation and debris-covered snow in the Cordillera Blanca. The classification has been based on area masking, followed by connection of the masks on the basis of specific conditions. The input to the classification algorithm consisted of the Landsat bands, indexes and the ASTER digital elevation model. The algorithm is described in detail in Chapter 3.6. In course of the classification process several problems emerged, which had to be solved. The first problem was connected to the ISODATA classification. For three particular years, K-means classification had to be used instead of ISODATA classification. However, it has been discovered, that the classification algorithm consisting solely of ISODATA classification, and the classification algorithm consisting partly of K-means classification, give the same classification results. The next problem was related to snow and water misclassification. Visual observation of the output masked areas discovered, that the water and snow areas had been misclassified in certain cases. This problem has been partly solved by adding digital elevation model to the Raster Calculator algorithm and by setting threshold values for water and snow areas. The classification of debris-covered snow area has been completed by applying Paul's (2004) criteria. Paul applied a terrain slope threshold value of 24° to determine debris-covered snow areas. Following several tests, the slope threshold value has been set to 25° for the purposes of this diploma thesis.

Visual observation of the output classified images has revealed, that the results contain many separated pixels. Due to this fact, a majority filter with kernel size of 8 neighboring cells had to be applied to all of the 29 classified images. The effect of image filtering has been computed and the results showed, that the filtering process was balanced and had no significant impact on further analyses.

The classification accuracy has been verified by comparing the results with GLIMS Glacier Database shapefiles. As regards snow area, the results of this diploma thesis exceeded the results in the GLIMS Glacier Database by 12,94 % in 2003 and 13,05 % in 2005. With respect to debris-covered snow area the comparison gave significant differences, which can be explained by methodology discrepancies. Additionally, the classified Landsat 5 image from 2010 has been compared with field measurement data provided by Emmer. The low value of classification accuracy (55 %) could have been caused by the low number of sample points and the low number of classified classes. At this point it should be noted, that it still does not appear to be a consensus within the glaciological community on the best method for estimating errors associated with glacier area estimates generated from automated methods (Racoviteanu et al., 2009, Cit. In Burns

and Nolin, 2014). The central problem is that high-resolution 'true area' measurements, which could be used for traditional error analyses, are limited, especially for the Cordillera Blanca (Burns and Nolin, 2014). The accuracy of the classification conducted in this diploma thesis could have been affected by the quality of input datasets, the lack of topographic correction (which has been balanced by extended classification algorithm), variable cloud cover in the Landsat scenes, unsupervised classification algorithm and applied image filtering (the impact of filtering was not significant, though).

Given the limitations of traditional error analysis, it is essential to confront the result of this diploma thesis with the data available from scientific publications. Racoviteanu et al. (2008) identified 485 glaciers with a total area of 516,1 km^2 in 2003. Out of these, 57 glaciers had debris-covered tongues, totaling an area of 14,9 km^2. This diploma thesis gives significantly different results (total area of 588,8 km^2 and debris-covered area of 105,8 km^2) for this particular year. Nevertheless, it is important to note that this inconsistency could be caused by different methodology (difference between the definition of glaciers and snow cover, detection of debris-covered areas inside the glaciers and outside them), as well as by differences in the study area (Racoviteanu's study focuses on the whole area of the Cordillera Blanca, whereas this diploma thesis aims attention at the northern part of the Cordillera Blanca). The only possible comparison has been provided via GLIMS Glacier Database (by area clipping), where Racoviteanu's results are presented.

Silverio and Jaquet (2005) calculated the snow and ice covered glacier area of the Cordillera Blanca for the year 1965 as equal to 625 km^2 and the debris-covered glacier area as equal to 18 km^2. The same calculation for the year 1996 gave the following results: 582 km^2 of snow and ice covered glaciers and 18 km^2 of debris-covered glaciers. In total, Silverio and Jaquet (2005) estimated the glacierized area of the Cordillera Blanca as equal to 643 km^2 in 1987 and 600 km^2 in 1996. This diploma thesis gives a slightly different result for 1987 (total of 601 km^2) and a very close result for 1996 (total of 607 km^2). The study by Silverio and Jaquet (2005) also refers to a study by Hidrandina (1988), according to which the total glacierized area without distinction between ice and debris-covered glaciers equaled 721 km^2 in 1970. As this diploma thesis covers the period from 1987 to 2014, no comparison is possible for the years 1965 and 1970. The study by Silverio and Jaquet shows constant glacier area loss based on three time periods (1970, 1987 and 1996). However, this diploma thesis did not give this clear result. The snow area across the monitored time period has not changed constantly, but the change had a clear negative trend.

Additionally, the mean snowline altitude change has been computed in the whole Cordillera Blanca, the three selected mountains and the eleven selected glaciers. Firstly, the

snowline had to be selected for each particular year from the vectored classified image. Secondly, the mean snowline altitude has been computed using ASTER digital elevation model. Finally, the mean snowline altitude change has been visually presented in maps and charts for all of the glaciers. The analysis showed that the Landsat 4 image from 1989 had a high cloud cover and thus was not usable for mean snowline altitude change interpretation. Racoviteanu et al. (2008) show that in 2003 elevations of the glacier termini in the whole Cordillera Blanca ranged from 4204 m to 5367 m, with a mean of 4881 m. These results are based on SPOT images from 2003 and DEM from 1970. For comparison, the mean snowline altitude computed in this diploma thesis equals 5018,9 m for the Huandoy mountain, 4942 m for the Huascarán mountain and 4953,5 m for the Santa Cruz mountain in this particular year. Unfortunately, no results are available for the whole Cordillera Blanca.

Finally, slope and aspect analyses have been conducted on the glacier change in the Cordillera Blanca. The computation based on slope and aspect images created from ASTER digital elevation model has been conducted for all of the three selected mountains (the Huandoy mountain, the Huascarán mountain, the Santa Cruz mountain) in the period from 1989 to 2010. The slope analysis discovered that in the Huandoy and Huascarán mountains snow areas with a higher slope were more likely to change during monitored time period. On contrary, in the Santa Cruz mountain snow areas with a medium slope (30,0-44,9 degrees) changed more likely than snow areas with an extreme slope.

The aspect analysis did not show consistent results. Generally, orientation to the south had a slight dominance on glacier change in the monitored parts of the Cordillera Blanca. This dominance was observed in the Huandoy and Santa Cruz mountains. On the other hand, in the Huascarán mountain, the north-east orientation was dominant. Nevertheless, no clear pattern of aspect dominance has been discovered. Burns and Nolin (2014) showed, that glacier aspect appears to be important for glacier change in the Cordillera Blanca. Their study discovered that south and south-east facing glaciers had the largest relative percentage change. In addition to this, their study showed no significant difference in the total glacier area loss between glaciers that drain to the Pacific Ocean and those draining to the Atlantic. These results are consistent with the results of this diploma thesis.

Generally, the results of this diploma thesis are unique and it is hard to verify their accuracy. Traditional error analysis is limited because of the lack of true-area measurements. On the other hand, due to different methodology, different determination of the study area and differences in the monitored time period, it is problematic to compare the results of this diploma thesis with the data available from other studies.

Regarding the Landsat OLI/TIRS images, it has been discovered, that the new generation of Landsat sensors has no significant advantage for glacier classification for the purposes of this diploma thesis. It has rather disadvantages concerning data acquisition. The low number of available scenes in the USGS database implies the need to use images with high cloud cover.

6 CONCLUSION

The presented diploma thesis has focused on glacier change monitoring in the Cordillera Blanca. The main goal was to create a semi-automatic classification algorithm to discriminate snow, debris-covered snow, vegetation and water in the Cordillera Blanca. Before the classification process, Landsat and ASTER GDEM preprocessing has been conducted. Because of the lack of meteorological data and detailed elevation model, only the Landsat scenes coregistration has been tested and corrected. On the other hand, as it has been shown, atmospheric correction provided by the USGS was precise enough for completing this task. The lack of topographic correction has been fixed by classifying snow areas in illuminated areas and in shadowed areas.

During the spectral analysis it has been detected, that although spectral properties of the selected land cover types are similar, the land cover types can be separated by the semi-automatic classification algorithm after setting up the correct threshold values, using the combination of NDVI, NDWI and NDSI indexes and band 1 of the Landsat scenes. The classification algorithm has been based on masking techniques and further connection of the masks. For the debris-covered snow classification, Paul's criteria (2004) has been used. This method has not been used in this region before. The semi-automatic classification algorithm caused misclassification of the snow and water areas in some parts of the Cordillera Blanca. Because of this reason, some elevation criteria had to be added to the mask connection process. These criteria have partly solved the problem. Cloud cover in the study area was one of the main error sources. It was almost impossible to find Landsat scenes with no cloud cover at the end of the dry season. Because of the spectral similarity, cloud cover has usually been classified as snow or water area. It has been difficult to compute the accuracy of the classification algorithm by the means of classical error analysis or by comparing the results with data from other publications in this region. The main reason for this lies in the unique classification methodology, the general lack of field data in the Cordillera Blanca and the time period selected for glacier monitoring. The observation of the snow and debris-covered area change showed, that the results are not as linear and consistent, as it has been presumed. In the view of the above, it is necessary to choose as many time periods for glacier monitoring, as possible.

Based on the work by Paterson (1994), the mean snowline altitude change has been computed, which is roughly equal to the equilibrium line altitude change. The results showed, that the change is not linear, but it has a positive trend for the most of the selected glaciers. No unambiguous rule of the mean snowline altitude change depending on glacier location has been discovered.

Finally, the effect of slope and aspect on glacier change in the Cordillera Blanca has been computed. Generally, areas with a higher slope had higher tendency to change in the monitored period. The reason for this could be that areas with a higher slope have thinner snow cover, thus these areas change to rock or debris-covered area more easily, than the areas with thicker snow cover. Speaking of the aspect effect, orientation to the south had the biggest impact on snow area change. This result is in compliance with the results of other studies.

Future works on glacier change monitoring in the Cordillera Blanca should use detailed meteorological data, which would facilitate the selection of the most suitable data for glacier monitoring (i.e. data with the lowest temporary snow cover at the end of the dry season). Furthermore, future studies should use higher resolution satellite images and digital elevation models. Future works should also try to classify the land cover types of the Cordillera Blanca in detail. Finally, but most importantly, it is essential to collect field measurements in order to be able to verify the results of automatic classification algorithms.

REFERENCES

About Glaciers. Remote sensing of glaciers: A Case Study: The Mendenhall Glacier. University of Alaska [online]. [citied 24.07.2015]. Accessible from: http://www.polar-remotesensing.alaska.edu/case_glacier/about.html

ACKERMAN, S. 2004. Satellite Meteorology. University of Wisconsin-Madison [online]. [citied 24.07.2015]. Accessible from: http://profhorn.meteor.wisc.edu/wxwise/satmet/index.html

ADVANCED SPACEBORNE THERMAL EMISSION AND REFLECTION RADIOMETER (ASTER) GLOBAL DIGITAL ELEVATION MODEL (GDEM) VERSION 2 Readme. October 2011. p. 11

BHARDWAJ, A., JOSHI, P. K., SNEHMANI, SINGH, M. K. 2014. Mapping debris-covered glaciers and identifying factors affecting the accuracy. *Cold Regions Science and Technology*, 106-107, p. 161-174, Accessible from: http://www.sciencedirect.com/science/article/pii/S0165232X14001293

BURNS, P., NOLIN, A. 2014. Using atmospherically-corrected Landsat imagery to measure glacier area change in the Cordillera Blanca, Peru from 1987 to 2010. *Remote Sensing of Environment*, 140, p. 165-178. Accessible from: http://www.sciencedirect.com/science/article/pii/S0034425713002848

CECCATO, P., FLASSE, S., TARANTOLA, S., JACQUEMOUD, S., GRÉGOIRE, J.-M. 2001. Detecting vegetation leaf water content using reflectance in the optical domain. *Remote Sensing of Environment*, 77, p. 22-33, Accessible from: http://www.sciencedirect.com/science/article/pii/S0034425701001912

Clustering. Japan Association of Remote Sensing. [online]. [citied 24.07.2015]. Accessible from: http://wtlab.iis.u-tokyo.ac.jp/~wataru/lecture/rsgis/rsnote/cp11/cp11-3.htm

EARTH OBSERVATORY: Where every day is Earth Day. [online]. [citied 24.07.2015]. Accessible from: http://earthobservatory.nasa.gov/

EMMER, A., LOARTE, E. C., KLIMEŠ, J., VILÍMEK, V. 2015. Recent evolution and degradation of the bent Jatunraju glacier (Cordillera Blanca, Peru). *Geomorphology*, 228, p. 345-355. Accessible from: http://www.sciencedirect.com/science/article/pii/S0169555X14004930

ESA eduspace: European Space Agency. [online]. [citied 24.07.2015]. Accessible from: http://www.esa.int/ESA

Facts about glaciers. National Snow & Ice Data Center (NSIDC) [online]. [citied 24.07.2015]. Accessible from: http://nsidc.org/cryosphere/glaciers/quickfacts.html

GEMACHE, M. 2002. Mapping the Cordillera Huayhuash, Accessible from: http://www.mountaincartography.org/mt_hood/pdfs/gamache2.pdf

GLIMS: Global Land Ice Measurements from Space: Monitoring the World's Changing Glaciers. [online]. [citied 24.07.2015]. Accessible from: http://www.glims.org/

HALL, S. R., FARBER, D. L., RAMAGE, J. M., RODBELL, D. T., FINKEL, R. C., SMITH, J. A., MARK, B. G., KASSEL, CH. 2009. Geochronology of Quaternary glaciations from the tropical Cordillera Huayhuash, Peru. *Quatemary Science Reviews*, 28, p. 2991-3009, Accessible from: http://www.sciencedirect.com/science/article/pii/S0277379109002698

HASTENRATH, S., AMES, A. 1995. Recession of Yanatnarey Glacier in Cordillera Blanca, Peru, during the 20th century. *Journal of Glaciology*, 41, p. 6. Accessible from: http://www.igsoc.org:8080/journal/41/137/igs_journal_vol41_issue137_pg191-196.pdf

HEISKANEN, J., KAJUUTTI, K., PELLIKKA, P. 2003. Mapping glacier changes, snowline altitude and AAR using Landsat data in Svartisen, Northern Norway. OMEGA project, Development of Operational monitoring System of European Glacial Areas, p. 1. Accessible from: http://omega.utu.fi/reports/Heiskanen_et_al_Nice.pdf

HENDRIKS, J., PELLIKKA, P. 2007. Semi-automatic glacier delineation from Landsat imagery over Hintereisferner in the Austrian Alps. *Zeitschrift für Gletscherkunde und Glazialgeologie*, 41, p. 55-75. Accessible from: http://www.helsinki.fi/geography/geoinformatics/pdf/zgg_41_055-075_hendriks.pdf

ITURRIZAGA, L. 2013. Bent glacier tongues: A new look at Lliboutry's model of the evolution of the crooked Jatunraju Glacier (Parón Valley, Cordillera Blanca, Perú). *Geomorphology*, 198, p. 147-162. Accessible from: http://www.sciencedirect.com/science/article/pii/S0169555X13003085

JOMELLI, V., FAVIER, V., RABATEL, A., BRUNSTEIN, D., HOFFMAN, G., FRANCOU, B. 2009. Fluctuations of glaciers in the tropical Andes over the last millennium and palaeoclimatic implications: A review. *Palaeogeography, Palaeoclimatology, Palaeoecology*, 281, p. 269-282. Accessible from: http://www.sciencedirect.com/science/article/pii/S0031018209001369

KARIMI, N., FAROKHNIA, A., KARIMI, L., EFTEKHARI, M., GHALKHANI, H. 2012. Combining optical and thermal remote sensing data for mapping debris-covered glaciers (Alamkouh Glaciers, Iran). *Cold Regions Science and Technology*, 71, p. 73-83, Accessible from: http://www.sciencedirect.com/science/article/pii/S0165232X11001984

KASER, G. (1999): A review of the modern fluctuations of tropical glaciers. *Global and Planetary Change*, 22, p. 93-103. Accessible from: http://www.sciencedirect.com/science/article/pii/S0921818199000284

KASER, G., GEORGES, C. 1997. Changes of the equilibrium.-line altitude in the tropical Cordillera Blanca, Peru, 1930-50, and their spatial variations. *Annals of Glaciology*, 24, p. 6. Accessible from: http://www.igsoc.org:8080/annals/24/igs_annals_vol24_year1997_pg344-349.pdf

LICCIARDI, J., SCHAEFER, J., TAGGART, J., LUND, D. 2009. Holocene Glacier Fluctuations in the Peruvian Andes Indicate Northern Climate Linkages. *Science*, 325, p. 3. Accessible from: http://www.unh.edu/esci/people/pdf/licciardi_et-al-2009.pdf

LLIBOUTRY, L. 1977. Glaciological problems set by the control of dangerous lakes in Cordillera Blanca, Peru. II. Movement of a covered glacier embedded within a rock glacier. *Journal of Glaciology*, 79, p. 255-273. Accessible from: http://www.igsoc.org:8080/journal/18/79/igs_journal_vol18_issue079_pg255-273.pdf

LLIBOUTRY, L., ARNAO, B. M., PAUTRE, A., SCHNEIDER, B. 1977. Glaciological problems set by the control of dangerous lakes in Cordillera Blanca, Peru. I. Historical failures of morainic dams, their causes and prevention. *Journal of Glaciology*, 79, p. 239-254. Accessible from: http://www.igsoc.org:8080/journal/18/79/igs_journal_vol18_issue079_pg239-254.pdf

LLIBOUTRY, L., ARNAO, B. M., SCHNEIDER, B. 1977. Glaciological problems set by the control of dangerous lakes in Cordillera Blanca, Peru. III. Study of moraines and mass balances at Safuna. *Journal of Glaciology*, 79, p. 275-290. Accessible from: http://www.igsoc.org:8080/journal/18/79/igs_journal_vol18_issue079_pg275-290.pdf

MARK, B. G. 2002. Observations of modern deglaciation and hydrology in the Cordillera Blanca. ACTA MONTANA IRSM AS CR, 19 (123), p. 23-36.

MARK, B. G., SELTZER, G. O. 2005. Evaluation of recent glacier recession in the Cordillera Blanca, Peru (AD 1962–1999): spatial distribution of mass loss and climatic forcing. *Quatemary Science Reviews*, 24, p. 2265-2280, Accessible from: http://www.sciencedirect.com/science/article/pii/S0277379105000260

MATHIEU, R., CHINN, T., FITZHARRIS, B. 2009. Detecting the equilibrium-line altitudes of New Zealand glaciers using ASTER satellite images. *New Zealand Journal of Geology and Geophysics*, 52, p. 209-222. Accessible from: http://www.tandfonline.com/doi/abs/10.1080/00288300909509887

MCFADDEN, E. M., RAMAGE, J., RODBELL, D. T. 2011. Landsat TM and ETM+ derived snowline altitudes in the Cordillera Huayhuash and Cordillera Raura, Peru, 1986–2005. *The Cryosphere*, 5, p. 419-430. Accessible from: http://www.the-cryosphere.net/5/419/2011/tc-5-419-2011.html

MORRIS, J. N., POOLE, A. J., KLEIN, A. G. 2006. Retreat of tropical glaciers in Colombia and Venezuela from 1984 to 2004 as Measured from ASTER and Landsat Images. p. 11, Accessible from: http://www.easternsnow.org/proceedings/2006/morris_et_al.pdf

NICHOL, J., HANG, L. K., SING, W. M. 2006. Empirical correction of low Sun angle images in steeply sloping terrain: a slope-matching technique. *International Journal of Remote Sensing*, 27, p. 629-635. Accessible from: http://www.lsgi.polyu.edu.hk/rsrg/resources/people/paper/empirical_topocorr.pdf

OSMASTON, H. 2005. Estimates of glacier equilibrium line altitudes by the Area×Altitude, the Area×Altitude Balance Ratio and the Area×Altitude Balance Index methods and their validation. *Quaternary International*, 138–139, p. 22-31. Accessible from: http://www.sciencedirect.com/science/article/pii/S104061820500039X

PATERSON, W. S. B. 1994. The Physics of Glaciers. 3rd ed., Oxford, England: Pergamon. Accessible from: http://www.sciencedirect.com/science/book/9780080379449

PAUL, F., HUGGEL, CH., KÄÄB, A. 2004. Combining satellite multispectral image data and a digital elevation model for mapping debris-covered glaciers. *Remote Sensing of Environment*, 89, p. 510-518. Accessible from: http://www.sciencedirect.com/science/article/pii/S0034425703003444

RABATEL, A., FRANCOU, B., JOMELLI, V., NAVEAU, P., GRANCHER, D. 2008. A chronology of the little ice age in the tropical Andes of Bolivia (16°S) and its implications for climate reconstruction. *Quaternary Research*, 70, p. 198-212. Accessible from: http://www.sciencedirect.com/science/article/pii/S0033589408000318

RACOVITEANU, A. E., ARNAUD, Y., WILLIAMS, M. W., ORDONEZ, J. 2008. Decadal changes in glacier parameters in the Cordillera Blanca, Peru, derived from remote sensing. *Journal of Glaciology*, 186, p. 499-510. Accessible from: http://www.glims.org/glacierdata/data/lit_ref_files/racoviteanu2008b.pdf

SCHAUWECKER, S., ROHRER, M., ACUÑA, D., COCHACHIN, A., DÁVILA, L., FREY, H., GIRÁLDEZ, C., GÓMEZ, J., HUGGEL, C., JACQUES-COPER, M., LOARTE, E., SALZMANN, N., VUILLE, M. 2014. Climate trends and glacier retreat in the Cordillera Blanca, Peru, revisited. *Global and Planetary Change*, 119, p. 85-97, Accessible from: http://www.sciencedirect.com/science/article/pii/S0921818114001003

SEIDEL, K., EHRLER, C., MARTINEC, J., TURPIN, O. 1997. Derivation of the statistical snowline altitude from high resolution snow cover mapping. Proceedings of the EARSel Workshop Remote Sensing of Land Ice and Snow, University of Freiburg, Germany, 17-18 April 1997, 31–36. Accessible from: http://www.vision.ee.ethz.ch/publications/papers/proceedings/eth_biwi_00120.pdf

SEOS PROJECT: Introduction to Remote Sensing. [online]. [citied 24.07.2015]. Accessible from: http://www.seos-project.eu/home.html

SHUKLA, A., ARORA, M. K., GUPTA, R. P. 2010. Synergistic approach for mapping debris-covered glaciers using optical-thermal remote sensing data with inputs from geomorphometric parameters. *Remote Sensing of Environment*, 114, p. 1378-1387. Accessible from: http://www.sciencedirect.com/science/article/pii/S0034425710000374

SILVERIO, W., JAQUET, J.-M. 2005. Glacial cover mapping (1987-1996) of the Cordillera Blanca (Peru) using satellite imagery. *Remote Sensing of Environment*, 95, p. 342-350, Accessible from: http://www.sciencedirect.com/science/article/pii/S0034425705000192

SOLOMINA, O., JOMELLI, V., KASER, G., AMES, A., BERGER, B., POUYAUD, B. 2007. Lichenometry in the Cordillera Blanca, Peru: "Little Ice Age" moraine chronology. *Global and Planetary Change*, 59, p. 225-235. Accessible from: http://www.sciencedirect.com/science/article/pii/S0921818106002992

STANSELL, N. D., POLISSAR, P. J., ABBOTT, M. B. 2006. Last glacial maximum equilibrium-line altitude and paleo-temperature reconstructions for the Cordillera de Mérida, Venezuelan Andes. *Quaternary Research*, 67, p. 115-127. Accessible from: http://www.sciencedirect.com/science/article/pii/S0033589406000986

SUMMERFIELD, M. A. Global geomorphology: an introduction to the study of landforms. Reprint. Harlow, Essex: Longman Scientific. ISBN 978-058-2301-566.

USGS: Science for a changing world. [online]. [citied 24.07.2015]. Accessible from: http://www.usgs.gov

VUILLE, M., FRANCOU, B., WAGNON, P., JUEN, I., KASER, G., MARK, B. G., BRADLEY, R. S. 2008. Climate change and tropical Andean glaciers: Past, present and future. *Earth-Science Reviews*, 89, p. 79-96. Accessible from: http://www.geography.osu.edu/faculty/bmark/2008%20ESR%20Vuille_etal.pdf

YALE UNIVERSITY: Center for Earth Observation. [online]. [citied 24.07.2015]. Accessible from: http://yceo.yale.edu/

DATA SOURCES

U.S. Geological Survey: Earth Explorer. [online]. Accessible from: http://earthexplorer.usgs.gov/

RACOVITEANU, A. (submitter), RACOVITEANU, A. (analyst(s)). 2005. GLIMS Glacier Database. Boulder, CO. National Snow and Ice Data Center. http://dx.doi.org/10.7265/N5V98602

EMMER, A. (2015) Field measurement data in the Cordillera Blanca

LIST OF APPENDICES

APPENDICES

Appendix 1: Characteristics of downloaded Landsat images

Date			Time	Landsat generation	Sensor	Solar angles [degrees]	
Year	Month	Day				Zenith	Azimuth
1987	7	18	14:41	Landsat 5	TM	48,007	51,205
1988	8	21	14:47	Landsat 5	TM	41,517	60,839
1989	8	24	14:42	Landsat 5	TM	41,860	62,681
1989	9	1	14:49	Landsat 4	TM	38,556	65,082
1990	7	10	14:36	Landsat 5	TM	49,537	50,730
1991	8	14	14:39	Landsat 5	TM	44,626	59,168
1992	7	31	14:39	Landsat 5	TM	46,987	55,093
1993	7	2	14:38	Landsat 5	TM	49,292	49,224
1994	7	21	14:34	Landsat 5	TM	49,171	53,214
1995	8	25	14:19	Landsat 5	TM	46,992	66,327
1996	7	26	14:31	Landsat 5	TM	49,171	55,004
1997	7	29	14:47	Landsat 5	TM	45,623	52,985
1998	9	2	14:55	Landsat 5	TM	37,188	64,554
1999	7	11	15:09	Landsat 7	ETM+	43,507	44,457
1999	8	20	14:53	Landsat 5	TM	40,457	59,001
2000	7	21	14:53	Landsat 5	TM	45,436	49,940
2001	8	9	14:56	Landsat 5	TM	41,993	54,623
2002	8	20	15:04	Landsat 7	ETM+	38,152	56,978
2003	8	15	14:53	Landsat 5	TM	41,577	57,166
2004	8	1	14:59	Landsat 5	TM	42,840	51,684
2005	7	3	15:03	Landsat 5	TM	44,723	44,446
2006	7	22	15:09	Landsat 5	TM	42,387	46,694
2007	7	25	15:09	Landsat 5	TM	41,929	47,225
2008	8	12	15:02	Landsat 5	TM	40,149	54,552
2009	7	30	15:05	Landsat 5	TM	41,976	49,727
2010	8	18	15:06	Landsat 5	TM	38,106	55,709
2011	7	20	15:05	Landsat 5	TM	43,362	47,056
2013	7	9	15:18	Landsat 8	OLI/TIRS	41,970	42,099
2014	7	12	15:16	Landsat 8	OLI/TIRS	42,137	43,095

Appendix 2: Correlation between SWIR bands of downloaded Landsat scenes (1987-2014) - part 1 (L4 – Landsat 4, L5 – Landsat 5, L7 – Landsat 7 and L8 – Landsat 8)

	1987 L5	**1988 L5**	**1989 L4**	**1989 L5**	**1990 L5**	**1991 L5**	**1992 L5**	**1993 L5**	**1994 L5**	**1995 L5**	**1996 L5**	**1997 L5**	**1998 L5**	**1999 L7**	**1999 L5**
1987 L5	1,00	0,94	0,25	0,94	0,95	0,94	0,89	0,49	0,94	0,93	0,94	0,94	0,90	0,34	0,92
1988 L5	0,94	1,00	0,24	0,97	0,94	0,97	0,89	0,45	0,94	0,96	0,94	0,96	0,94	0,37	0,95
1989 L4	0,25	0,24	1,00	0,25	0,25	0,25	0,27	0,23	0,26	0,25	0,26	0,25	0,23	0,03	0,25
1989 L5	0,94	0,97	0,25	1,00	0,95	0,97	0,89	0,46	0,95	0,96	0,95	0,95	0,93	0,37	0,95
1990 L5	0,95	0,94	0,25	0,95	1,00	0,95	0,89	0,49	0,96	0,94	0,95	0,95	0,90	0,35	0,93
1991 L5	0,94	0,97	0,25	0,97	0,95	1,00	0,90	0,47	0,95	0,96	0,96	0,97	0,95	0,37	0,96
1992 L5	0,89	0,89	0,27	0,89	0,89	0,90	1,00	0,47	0,90	0,90	0,90	0,91	0,88	0,31	0,89
1993 L5	0,49	0,45	0,23	0,46	0,49	0,47	0,47	1,00	0,50	0,47	0,51	0,48	0,44	0,11	0,47
1994 L5	0,94	0,94	0,26	0,95	0,96	0,95	0,90	0,50	1,00	0,96	0,97	0,96	0,91	0,33	0,95
1995 L5	0,93	0,96	0,25	0,96	0,94	0,96	0,90	0,47	0,96	1,00	0,97	0,97	0,95	0,36	0,96
1996 L5	0,94	0,94	0,26	0,95	0,95	0,96	0,90	0,51	0,97	0,97	1,00	0,97	0,93	0,34	0,95
1997 L5	0,94	0,96	0,25	0,95	0,95	0,97	0,91	0,48	0,96	0,97	0,97	1,00	0,96	0,36	0,97
1998 L5	0,90	0,94	0,23	0,93	0,90	0,95	0,88	0,44	0,91	0,95	0,93	0,96	1,00	0,37	0,96
1999 L7	0,34	0,37	0,03	0,37	0,35	0,37	0,31	0,11	0,33	0,36	0,34	0,36	0,37	1,00	0,37
1999 L5	0,92	0,95	0,25	0,95	0,93	0,96	0,89	0,47	0,95	0,96	0,95	0,97	0,96	0,37	1,00
2000 L5	0,60	0,59	0,22	0,60	0,60	0,61	0,58	0,44	0,63	0,61	0,63	0,62	0,59	0,20	0,62
2001 L5	0,83	0,84	0,27	0,84	0,84	0,84	0,79	0,46	0,85	0,84	0,85	0,85	0,83	0,31	0,86
2002 L7	0,87	0,89	0,24	0,89	0,87	0,90	0,83	0,45	0,88	0,89	0,89	0,91	0,90	0,35	0,91
2003 L5	0,93	0,95	0,25	0,95	0,94	0,96	0,89	0,47	0,95	0,96	0,95	0,97	0,96	0,36	0,97
2004 L5	0,65	0,64	0,29	0,64	0,66	0,66	0,63	0,41	0,66	0,65	0,66	0,67	0,65	0,22	0,66
2005 L5	0,90	0,89	0,26	0,89	0,91	0,90	0,86	0,50	0,92	0,90	0,93	0,93	0,90	0,31	0,92
2006 L5	0,92	0,93	0,25	0,92	0,93	0,94	0,88	0,48	0,94	0,93	0,95	0,96	0,94	0,34	0,96
2007 L5	0,53	0,51	0,23	0,52	0,53	0,53	0,51	0,50	0,54	0,53	0,55	0,55	0,53	0,16	0,54
2008 L5	0,87	0,88	0,25	0,89	0,88	0,89	0,83	0,46	0,89	0,89	0,90	0,90	0,88	0,34	0,91
2009 L5	0,61	0,59	0,27	0,60	0,61	0,60	0,58	0,46	0,62	0,60	0,62	0,62	0,60	0,20	0,62
2010 L5	0,90	0,92	0,23	0,91	0,91	0,93	0,87	0,45	0,91	0,93	0,93	0,95	0,95	0,36	0,95
2011 L5	0,21	0,21	0,17	0,21	0,22	0,21	0,23	0,24	0,24	0,23	0,23	0,23	0,21	0,05	0,22
2013 L8	0,85	0,83	0,24	0,84	0,86	0,84	0,80	0,50	0,86	0,83	0,86	0,87	0,83	0,31	0,86
2014 L8	0,90	0,89	0,25	0,89	0,91	0,90	0,85	0,48	0,92	0,89	0,92	0,93	0,90	0,33	0,92

Appendix 3: Correlation between SWIR bands of downloaded Landsat scenes (1987-2014) - part 2 (L4 – Landsat 4, L5 – Landsat 5, L7 – Landsat 7 and L8 – Landsat 8)

	2000 L5	**2001 L5**	**2002 L7**	**2003 L5**	**2004 L5**	**2005 L5**	**2006 L5**	**2007 L5**	**2008 L5**	**2009 L5**	**2010 L5**	**2011 L5**	**2013 L8**	**2014 L8**
1987 L5	0,60	0,83	0,87	0,93	0,65	0,90	0,92	0,53	0,87	0,61	0,90	0,21	0,85	0,90
1988 L5	0,59	0,84	0,89	0,95	0,64	0,89	0,93	0,51	0,88	0,59	0,92	0,21	0,83	0,89
1989 L4	0,22	0,27	0,24	0,25	0,29	0,26	0,25	0,23	0,25	0,27	0,23	0,17	0,24	0,25
1989 L5	0,60	0,84	0,89	0,95	0,64	0,89	0,92	0,52	0,89	0,60	0,91	0,21	0,84	0,89
1990 L5	0,60	0,84	0,87	0,94	0,66	0,91	0,93	0,53	0,88	0,61	0,91	0,22	0,86	0,91
1991 L5	0,61	0,84	0,90	0,96	0,66	0,90	0,94	0,53	0,89	0,60	0,93	0,21	0,84	0,90
1992 L5	0,58	0,79	0,83	0,89	0,63	0,86	0,88	0,51	0,83	0,58	0,87	0,23	0,80	0,85
1993 L5	0,44	0,46	0,45	0,47	0,41	0,50	0,48	0,50	0,46	0,46	0,45	0,24	0,50	0,48
1994 L5	0,63	0,85	0,88	0,95	0,66	0,92	0,94	0,54	0,89	0,62	0,91	0,24	0,86	0,92
1995 L5	0,61	0,84	0,89	0,96	0,65	0,90	0,93	0,53	0,89	0,60	0,93	0,23	0,83	0,89
1996 L5	0,63	0,85	0,89	0,95	0,66	0,93	0,95	0,55	0,90	0,62	0,93	0,23	0,86	0,92
1997 L5	0,62	0,85	0,91	0,97	0,67	0,93	0,96	0,55	0,90	0,62	0,95	0,23	0,87	0,93
1998 L5	0,59	0,83	0,90	0,96	0,65	0,90	0,94	0,53	0,88	0,60	0,95	0,21	0,83	0,90
1999 L7	0,20	0,31	0,35	0,36	0,22	0,31	0,34	0,16	0,34	0,20	0,36	0,05	0,31	0,33
1999 L5	0,62	0,86	0,91	0,97	0,66	0,92	0,96	0,54	0,91	0,62	0,95	0,22	0,86	0,92
2000 L5	1,00	0,57	0,59	0,61	0,48	0,61	0,62	0,48	0,59	0,50	0,60	0,25	0,59	0,61
2001 L5	0,57	1,00	0,81	0,86	0,68	0,85	0,85	0,51	0,82	0,58	0,83	0,22	0,79	0,83
2002 L7	0,59	0,81	1,00	0,92	0,64	0,87	0,90	0,54	0,87	0,62	0,90	0,23	0,82	0,88
2003 L5	0,61	0,86	0,92	1,00	0,68	0,94	0,97	0,55	0,92	0,62	0,96	0,23	0,87	0,94
2004 L5	0,48	0,68	0,64	0,68	1,00	0,70	0,68	0,49	0,66	0,53	0,66	0,21	0,65	0,67
2005 L5	0,61	0,85	0,87	0,94	0,70	1,00	0,95	0,57	0,90	0,63	0,92	0,24	0,88	0,93
2006 L5	0,62	0,85	0,90	0,97	0,68	0,95	1,00	0,57	0,92	0,63	0,96	0,23	0,89	0,96
2007 L5	0,48	0,51	0,54	0,55	0,49	0,57	0,57	1,00	0,56	0,50	0,55	0,25	0,56	0,56
2008 L5	0,59	0,82	0,87	0,92	0,66	0,90	0,92	0,56	1,00	0,62	0,91	0,24	0,85	0,90
2009 L5	0,50	0,58	0,62	0,62	0,53	0,63	0,63	0,50	0,62	1,00	0,62	0,29	0,62	0,64
2010 L5	0,60	0,83	0,90	0,96	0,66	0,92	0,96	0,55	0,91	0,62	1,00	0,22	0,87	0,94
2011 L5	0,25	0,22	0,23	0,23	0,21	0,24	0,23	0,25	0,24	0,29	0,22	1,00	0,25	0,24
2013 L8	0,59	0,79	0,82	0,87	0,65	0,88	0,89	0,56	0,85	0,62	0,87	0,25	1,00	0,91
2014 L8	0,61	0,83	0,88	0,94	0,67	0,93	0,96	0,56	0,90	0,64	0,94	0,24	0,91	1,00

Appendix 4: Matlab algorithm used to compare Landsat scenes through control points

```
clc
clear
format compact

image1 = imread('1987_LT50080661987199XXX07_sr_band5_subset.TIF');
image2 = imread('1988_LT50080661988234CUB00_sr_band5_subset.TIF');

[a,b,c] = size(image1);

npx = 9; %the number of all control points is npx*npy
npy = 9;
crop1sizex = 15;
crop1sizey = 15;
crop2sizex = 31;
crop2sizey = 31;
corr = -1; %correlation set to -1 as default

A = zeros(npx,npy);
B = zeros(npx,npy);

for i = 1:npx
    for j = 1:npy
        x1 = i*((1/(npx+1))*a);
        y1 = j*((1/(npy+1))*b);
        crop1 = imcrop(image1,[x1-((crop1sizex-1)/2) y1-((crop1sizex-1)/2)
crop1sizex-1 crop1sizey-1]);

        for m = 1:(crop2sizex-crop1sizex+1)
            for n = 1:(crop2sizey-crop1sizey+1)
                crop2 = imcrop(image2,[x1-(((crop2sizex+1)/2)-m) y1-
(((crop2sizey+1)/2)-n) crop1sizex-1 crop1sizey-1]);
                corrtemp = corr2(crop1,crop2);
                if corrtemp > corr
                    corr = corrtemp;
                    x2 = x1-(((crop2sizex-crop1sizex+2)/2)-m);
                    y2 = y1-(((crop2sizey-crop1sizey+2)/2)-n);
                end
            end
        end
        A(i,j) = corr;
        corr = -1;
        B(i,j) = sqrt((x2-x1)^2+(y2-y1)^2);
    end
end

max(B(:))
median(B(:))
```

Appendix 5: Maximum distances (in pixels) between the centers of the sample area and the search window during Matlab computation - part 1 (L4 – Landsat 4, L5 – Landsat 5, L7 – Landsat 7 and L8 – Landsat 8)

	1987 L5	**1988 L5**	**1989 L4**	**1989 L5**	**1990 L5**	**1991 L5**	**1992 L5**	**1993 L5**	**1994 L5**	**1995 L5**	**1996 L5**	**1997 L5**	**1998 L5**	**1999 L7**	**1999 L5**
1987 L5	0,0	5,0	11,3	8,2	8,5	11,3	10,6	11,3	5,7	7,3	7,3	9,4	8,9	11,3	8,5
1988 L5	5,0	0,0	11,3	4,5	8,5	8,5	1,4	11,3	4,5	8,5	11,3	6,1	8,5	11,3	5,1
1989 L4	11,3	11,3	0,0	10,6	11,3	10,6	10,6	11,3	11,3	10,6	11,3	11,3	11,3	11,3	11,3
1989 L5	8,2	4,5	10,6	0,0	4,5	7,2	7,6	11,3	4,1	7,2	11,3	8,2	8,2	11,3	8,0
1990 L5	8,5	8,5	11,3	4,5	0,0	7,1	8,9	11,3	4,1	10,0	10,6	10,0	8,9	11,3	8,5
1991 L5	11,3	8,5	10,6	7,2	7,1	0,0	1,4	11,3	6,0	5,7	10,0	3,2	5,0	11,3	4,1
1992 L5	10,6	1,4	10,6	7,6	8,9	1,4	0,0	11,3	6,1	7,8	5,0	3,6	6,4	11,3	3,6
1993 L5	11,3	11,3	11,3	11,3	11,3	11,3	11,3	0,0	11,3	11,3	11,3	11,3	11,3	11,3	11,3
1994 L5	5,7	4,5	11,3	4,1	4,1	6,0	6,1	11,3	0,0	8,2	9,4	8,2	8,1	11,3	8,2
1995 L5	7,3	8,5	10,6	7,2	10,0	5,7	7,8	11,3	8,2	0,0	9,4	1,4	5,0	11,3	3,0
1996 L5	7,3	11,3	11,3	11,3	10,6	10,0	5,0	11,3	9,4	9,4	0,0	8,9	8,9	11,3	9,4
1997 L5	9,4	6,1	11,3	8,2	10,0	3,2	3,6	11,3	8,2	1,4	8,9	0,0	3,2	11,3	1,4
1998 L5	8,9	8,5	11,3	8,2	8,9	5,0	6,4	11,3	8,1	5,0	8,9	3,2	0,0	11,3	6,3
1999 L7	11,3	11,3	11,3	11,3	11,3	11,3	11,3	11,3	11,3	11,3	11,3	11,3	11,3	0,0	11,3
1999 L5	8,5	5,1	11,3	8,0	8,5	4,1	3,6	11,3	8,2	3,0	9,4	1,4	6,3	11,3	0,0
2000 L5	11,3	11,3	11,3	10,6	11,3	11,3	10,0	11,3	11,3	10,6	10,6	10,0	10,0	11,3	10,0
2001 L5	8,5	8,9	10,6	9,4	10,6	10,6	10,6	11,3	10,6	11,3	11,3	11,3	11,3	11,3	11,3
2002 L7	11,3	11,3	11,3	11,3	11,3	10,6	11,3	11,3	11,3	11,3	11,3	11,3	11,3	11,3	10,6
2003 L5	8,6	7,3	10,6	7,8	7,1	5,4	4,2	11,3	7,2	8,5	8,9	7,3	4,0	11,3	7,3
2004 L5	11,3	11,3	10,6	11,3	11,3	11,3	11,3	11,3	11,3	8,9	11,3	11,3	11,3	11,3	11,3
2005 L5	8,2	10,0	11,3	10,0	9,4	9,4	8,9	11,3	10,0	8,5	9,4	9,4	10,0	11,3	10,6
2006 L5	10,0	10,6	11,3	10,0	10,6	7,1	6,1	11,3	9,2	10,0	7,3	6,3	8,0	11,3	8,5
2007 L5	11,3	11,3	11,3	11,3	11,3	11,3	11,3	11,3	11,3	11,3	11,3	11,3	11,3	11,3	11,3
2008 L5	11,3	8,9	11,3	6,7	6,7	6,3	6,4	11,3	6,7	8,5	7,3	6,4	8,1	11,3	8,5
2009 L5	11,3	10,6	11,3	10,6	10,6	10,6	10,6	11,3	10,6	11,3	10,6	10,6	11,3	11,3	10,6
2010 L5	8,9	8,5	11,3	8,2	9,2	8,2	8,9	11,3	8,5	8,5	8,5	8,9	8,9	11,3	8,5
2011 L5	11,3	11,3	11,3	11,3	11,3	11,3	11,3	11,3	11,3	11,3	11,3	11,3	11,3	11,3	11,3
2013 L8	11,3	11,3	11,3	11,3	11,3	11,3	11,3	11,3	11,3	11,3	11,3	11,3	11,3	11,3	11,3
2014 L8	8,2	8,5	11,3	8,5	8,1	10,6	8,5	11,3	10,0	8,9	8,0	10,6	10,0	11,3	10,6

Appendix 6: Maximum distances (in pixels) between the centers of the sample area and the search window during Matlab computation - part 2 (L4 – Landsat 4, L5 – Landsat 5, L7 – Landsat 7 and L8 – Landsat 8)

	2000 L5	**2001 L5**	**2002 L7**	**2003 L5**	**2004 L5**	**2005 L5**	**2006 L5**	**2007 L5**	**2008 L5**	**2009 L5**	**2010 L5**	**2011 L5**	**2013 L8**	**2014 L8**
1987 L5	11,3	8,5	11,3	8,6	11,3	8,2	10,0	11,3	11,3	11,3	8,9	11,3	11,3	8,2
1988 L5	11,3	8,9	11,3	7,3	11,3	10,0	10,6	11,3	8,9	10,6	8,5	11,3	11,3	8,5
1989 L4	11,3	10,6	11,3	10,6	10,6	11,3	11,3	11,3	11,3	11,3	11,3	11,3	11,3	11,3
1989 L5	10,6	9,4	11,3	7,8	11,3	10,0	10,0	11,3	6,7	10,6	8,2	11,3	11,3	8,5
1990 L5	11,3	10,6	11,3	7,1	11,3	9,4	10,6	11,3	6,7	10,6	9,2	11,3	11,3	8,1
1991 L5	11,3	10,6	10,6	5,4	11,3	9,4	7,1	11,3	6,3	10,6	8,2	11,3	11,3	10,6
1992 L5	10,0	10,6	11,3	4,2	11,3	8,9	6,1	11,3	6,4	10,6	8,9	11,3	11,3	8,5
1993 L5	11,3	11,3	11,3	11,3	11,3	11,3	11,3	11,3	11,3	11,3	11,3	11,3	11,3	11,3
1994 L5	11,3	10,6	11,3	7,2	11,3	10,0	9,2	11,3	6,7	10,6	8,5	11,3	11,3	10,0
1995 L5	10,6	11,3	11,3	8,5	8,9	8,5	10,0	11,3	8,5	11,3	8,5	11,3	11,3	8,9
1996 L5	10,6	11,3	11,3	8,9	11,3	9,4	7,3	11,3	7,3	10,6	8,5	11,3	11,3	8,0
1997 L5	10,0	11,3	11,3	7,3	11,3	9,4	6,3	11,3	6,4	10,6	8,9	11,3	11,3	10,6
1998 L5	10,0	11,3	11,3	4,0	11,3	10,0	8,0	11,3	8,1	11,3	8,9	11,3	11,3	10,0
1999 L7	11,3	11,3	11,3	11,3	11,3	11,3	11,3	11,3	11,3	11,3	11,3	11,3	11,3	11,3
1999 L5	10,0	11,3	10,6	7,3	11,3	10,6	8,5	11,3	8,5	10,6	8,5	11,3	11,3	10,6
2000 L5	0,0	11,3	11,3	10,6	11,3	11,3	11,3	11,3	11,3	11,3	11,3	11,3	11,3	11,3
2001 L5	11,3	0,0	10,6	5,0	11,3	10,0	7,1	10,0	7,1	10,6	10,0	11,3	11,3	10,6
2002 L7	11,3	10,6	0,0	11,3	11,3	10,6	10,6	11,3	11,3	11,3	11,3	11,3	11,3	11,3
2003 L5	10,6	5,0	11,3	0,0	11,3	10,0	4,5	11,3	6,4	10,6	7,6	11,3	11,3	10,0
2004 L5	11,3	11,3	11,3	11,3	0,0	10,0	10,0	10,6	10,0	11,3	10,0	11,3	10,6	10,0
2005 L5	11,3	10,0	10,6	10,0	10,0	0,0	2,2	11,3	8,1	11,3	8,2	11,3	11,3	9,4
2006 L5	11,3	7,1	10,6	4,5	10,0	2,2	0,0	11,3	4,1	11,3	8,2	11,3	11,3	8,5
2007 L5	11,3	10,0	11,3	11,3	10,6	11,3	11,3	0,0	11,3	11,3	11,3	11,3	10,6	11,3
2008 L5	11,3	7,1	11,3	6,4	10,0	8,1	4,1	11,3	0,0	11,3	8,0	11,3	11,3	8,0
2009 L5	11,3	10,6	11,3	10,6	11,3	11,3	11,3	11,3	11,3	0,0	11,3	11,3	11,3	11,3
2010 L5	11,3	10,0	11,3	7,6	10,0	8,2	8,2	11,3	8,0	11,3	0,0	11,3	11,3	9,4
2011 L5	11,3	11,3	11,3	11,3	11,3	11,3	11,3	11,3	11,3	11,3	11,3	0,0	11,3	11,3
2013 L8	11,3	11,3	11,3	11,3	10,6	11,3	11,3	10,6	11,3	11,3	11,3	11,3	0,0	10,0
2014 L8	11,3	10,6	11,3	10,0	10,0	9,4	8,5	11,3	8,0	11,3	9,4	11,3	10,0	0,0

Appendix 7: Median distances (in pixels) between the centers of the sample area and the search window during Matlab computation - (L4 – Landsat 4, L5 – Landsat 5, L7 – Landsat 7 and L8 – Landsat 8)

	1999 L7	**2011 L5**
1987 L5	8,0	0,0
1988 L5	8,0	1,0
1989 L4	8,2	5,4
1989 L5	7,8	1,0
1990 L5	8,1	1,0
1991 L5	8,1	1,4
1992 L5	8,0	0,0
1993 L5	8,1	1,0
1994 L5	8,1	0,0
1995 L5	8,1	1,0
1996 L5	8,1	0,0
1997 L5	8,1	0,0
1998 L5	8,1	1,0
1999 L7	0,0	8,0
1999 L5	8,2	1,0
2000 L5	8,1	1,0
2001 L5	8,0	0,0
2002 L7	8,1	1,4
2003 L5	8,1	1,0
2004 L5	8,2	0,0
2005 L5	8,0	0,0
2006 L5	8,1	0,0
2007 L5	8,1	0,0
2008 L5	8,1	0,0
2009 L5	8,1	0,0
2010 L5	8,0	0,0
2011 L5	8,0	0,0
2013 L8	8,1	0,0
2014 L8	8,1	0,0

Appendix 8: RMS error distribution of the GCPs

No. GCP	**Base Image (1999, L5)**		**Warp Image (1999, L7)**		**Predicted Image**		**Error**		**RMS Error [px]**
	x [px]	**y [px]**	**x [px]**	**y [px]**	**x [px]**	**y [px]**	**x [px]**	**y [px]**	
1	6946,6	2113,7	6804,7	2072,4	0,0	0,0	0,0	0,0	0,0
2	6383,4	1262,5	6240,5	1221,5	6241,0	1221,6	0,4	0,1	0,4
3	2057,5	4821,4	1906,4	4778,5	0,0	0,0	0,0	0,0	0,0
4	2879,6	6043,5	2732,4	6002,3	2731,0	6001,7	-1,4	-0,6	1,6
5	2250,0	1837,2	2091,3	1793,9	2090,6	1793,4	-0,7	-0,5	0,9
6	4308,3	3300,7	4165,4	3259,4	0,0	0,0	0,0	0,0	0,0
7	1321,3	4326,5	1158,4	4282,6	1160,1	4282,9	1,7	0,3	1,8
8	2962,8	4418,8	2812,0	4376,2	2811,7	4376,5	-0,3	0,3	0,5
9	4833,7	4907,5	4694,8	4866,6	4695,4	4866,8	0,6	0,2	0,6
10	4064,7	1800,2	3918,4	1758,4	0,0	0,0	0,0	0,0	0,0
11	3143,3	2784,5	2991,6	2742,0	2990,0	2741,8	-1,6	-0,2	1,7
12	1554,7	2643,8	1392,0	2599,5	1393,0	2599,9	1,0	0,4	1,0
13	4061,0	5715,0	3920,0	5673,9	3919,8	5674,0	-0,2	0,1	0,2
14	5488,0	6045,0	5357,0	6005,2	5357,6	6005,2	0,6	0,0	0,6

Appendix 9: Correlation and median distance comparison for the Landsat 7 scene from the year 1999 before and after geometric transformation (L4 – Landsat 4, L5 – Landsat 5, L7 – Landsat 7 and L8 – Landsat 8)

	Correlation		**Median distances [pixels]**	
	1999 L7 before transformation	**1999 L7 after transformation**	**1999 L7 before transformation**	**1999 L7 after transformation**
1987 L5	0,34	0,87	8,0	1,0
1988 L5	0,37	0,87	8,0	1,0
1989 L4	0,03	0,23	8,2	1,4
1989 L5	0,37	0,87	7,8	1,0
1990 L5	0,35	0,89	8,1	1,0
1991 L5	0,37	0,87	8,1	1,0
1992 L5	0,31	0,82	8,0	1,0
1993 L5	0,11	0,46	8,1	1,0
1994 L5	0,33	0,90	8,1	1,0
1995 L5	0,36	0,86	8,1	1,0
1996 L5	0,34	0,89	8,1	1,0
1997 L5	0,36	0,89	8,1	1,0
1998 L5	0,37	0,85	8,1	1,0
1999 L7	1,00	1,00	0,0	0,0
1999 L5	0,37	0,90	8,2	1,0
2000 L5	0,20	0,59	8,1	1,4
2001 L5	0,31	0,80	8,0	1,0
2002 L7	0,35	0,83	8,1	1,0
2003 L5	0,36	0,88	8,1	1,0
2004 L5	0,22	0,62	8,2	1,4
2005 L5	0,31	0,87	8,0	1,0
2006 L5	0,34	0,89	8,1	1,0
2007 L5	0,16	0,52	8,1	1,0
2008 L5	0,34	0,84	8,1	1,0
2009 L5	0,20	0,59	8,1	1,0
2010 L5	0,37	0,86	8,0	1,0
2011 L5	0,05	0,21	8,0	3,0
2013 L8	0,31	0,83	8,1	1,0
2014 L8	0,33	0,88	8,1	1,0

Appendix 10: Comparison of measured points provided by Emmer with the results of the classification provided in this diploma thesis – part 1 (Classes: I – snow, II – debris-covered snow, III – water, IV – vegetation, V - other)

POINT	LATITUDE (S)	LONGITUDE (W)	ALTITUDE (m a.s.l.)	LOCALITY	CLASS_FIELD	CLASS_CLASS	EQUALS	ACCURACY < ± 10 m	YEAR TAKEN	NOTE
1	9.479667	77.424911	4571	Churup	V	II	N	Y	2015	Churupito moraine
2	9.475747	77.422750	4729	Churup	V	V	Y	Y	2015	exposed bedrock (young)
3	9.473816	77.422642	4818	Churup	V	II	N	Y	2015	exposed bedrock (young)
4	9.475491	77.426266	4821	Churup	V	V	Y	Y	2015	scree
5	9.481239	77.428691	4549	Churup	IV	IV	Y	N	2015	polylepis
6	9.482892	77.429619	4544	Churup	IV	V	N	Y	2015	grass
7	9.476550	77.427202	4820	Churup	V	V	Y	Y	2015	exposed bedrock (old)
8	9.487967	77.430081	4504	Churup	III	III	Y	Y	2015	
9	9.471814	77.420303	4950	Churup	I	I	Y	Y	2015	small glacier
10	9.912964	77.184872	4995	Pastoruri	III	I	N	Y	2015	young proglacial lake
11	9.917106	77.185519	5040	Pastoruri	I	I	Y	Y	2015	
12	9.913869	77.183806	5010	Pastoruri	V	I	N	Y	2015	bedrock (sedimentary rock)
13	8.929867	77.662231	3888	Santa Cruz	III	III	Y	Y	2015	
14	8.919056	77.616239	4150	Santa Cruz	IV	V	N	Y	2015	vegetated moraine
15	8.924283	77.615967	4231	Santa Cruz	V	V	Y	Y	2015	accumulation of 2012 GLOF
16	8.915213	77.622108	3955	Santa Cruz	IV	IV	Y	N	2015	polylepis
17	8.938567	77.677725	3850	Santa Cruz	IV / V	V	Y	Y	2015	pampa (seasonally vegetated lake)
18	9.429608	77.440783	4516	Llaca	II	II	Y	Y	2012	cca 0,5 m thick debris cover
19	9.436017	77.446556	4473	Llaca	IV	IV	Y	N	2012	polylepis
20	9.004656	77.678881	4483	Jatunraju	II	II	Y	Y	2014	debris thickness cca 1 m
21	8.994167	77.690286	4748	Jatunraju	V	V	Y	Y	2014	breached moraine
22	9.313694	77.206267	3507	Purhuay	III	III	Y	Y	2015	
23	9.315383	77.205072	3528	Purhuay	V	V	Y	Y	2015	rockslide accumulation
24	9.317366	77.201558	3399	Purhuay	IV	IV	Y	N	2015	eucalyptus forest
25	9.527511	77.528592	3062	Huaráz	V	II	N	Y	2015	settlement (artificial surfaces)

Appendix 11: Comparison of measured points provided by Emmer with the results of the classification provided in this diploma thesis – part 2 (Classes: I – snow, II – debris-covered snow, III – water, IV – vegetation, V - other)

POINT	LATITUDE (S)	LONGITUDE (W)	ALTITUDE (m a.s.l.)	LOCALITY	CLASS_FIELD	CLASS_CLASS	EQUALS	ACCURACY < ± 10 m	YEAR TAKEN	NOTE
26	9.046503	77.809331	2248	Caraz	V	II	N	Y	2015	settlement (artificial surfaces)
27	9.092355	77.548722	4715	Ulta	II	II	Y	N	2013	debris thickness cca 2-3 m
28	9.094556	77.546083	4616	Ulta	III	III	Y	N	2013	
29	9.117344	77.517700	4270	Ulta	IV	IV	Y	N	2013	polylepis
30	9.116175	77.522814	4135	Ulta	V	II	N	Y	2013	debris fan
31	9.027483	77.636861	4763	NE Huandoy	IV	II	N	N	2014	debris thickness cca 0,5 m
32	8.965519	77.639397	4807	Parón / Arteson	I	I	Y	Y	2014	
33	8.965678	77.645061	4836	Parón / Arteson	V	II	N	Y	2014	moraine
34	8.981464	77.647467	4217	Parón	V	II	N	Y	2014	debris fan
35	9.012431	77.611067	4625	Lake 69	V	II	N	N	2015	moraine
36	9.029808	77.626611	4637	NE Huandoy	V	II	N	Y	2014	rock glacier
37	9.215947	77.552725	4422	Chucchun	V	II	N	Y	2014	exposed bedrock (young)
38	9.210742	77.542317	4642	Chucchun	I	I	Y	Y	2014	
39	9.235206	77.577978	3608	Chucchun	IV	V	N	Y	2014	pampa
40	9.366886	77.422092	4425	Ishinca	V	II	N	Y	2013	debris fan
41	9.384522	77.402486	5210	Ishinca	I	I	Y	Y	2013	
42	9.384914	77.401189	5170	Ishinca	III	I	N	Y	2013	new lake
43	9.386972	77.397772	5290	Ishinca	V	V	N	Y	2013	scree
44	9.396667	77.421078	5210	Ishinca	I	I	Y	Y	2013	small glacier / snow field
45	9.393906	77.425847	4890	Ishinca	V	II	N	Y	2013	scree

Appendix 12: Classified land cover in the Cordillera Blanca in 1987

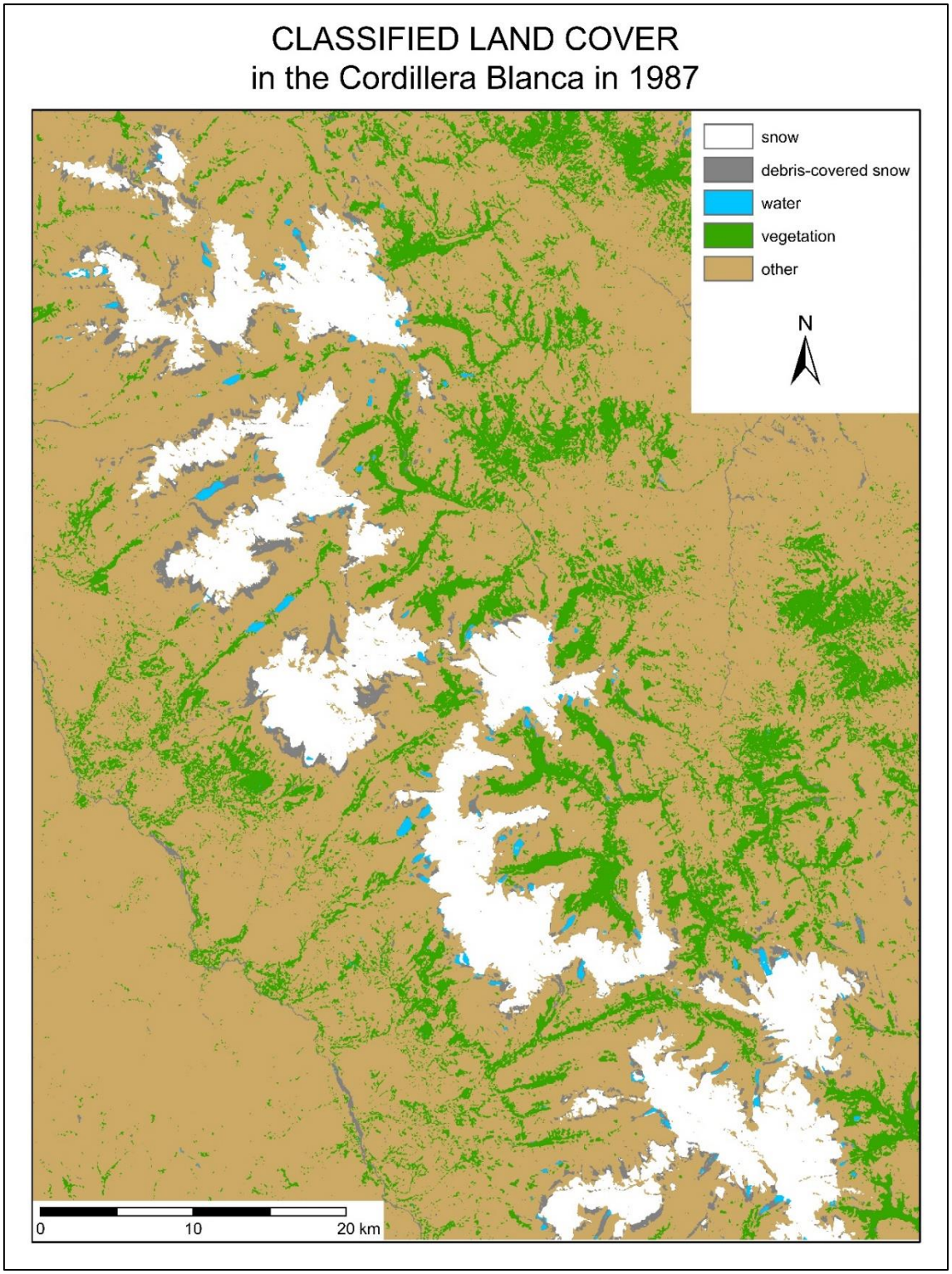

Appendix 13: Classified land cover in the Huascarán mountain in 1987

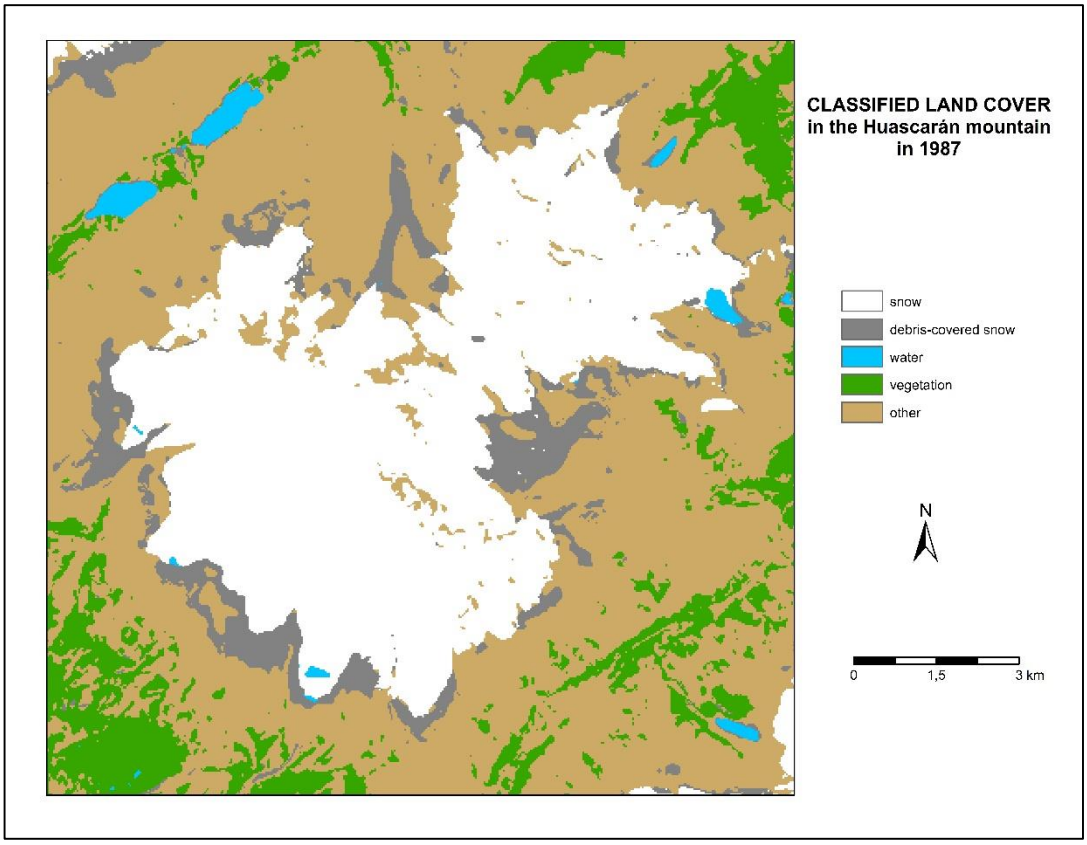

Appendix 14: Classified land cover in the Santa Cruz mountain in 1987

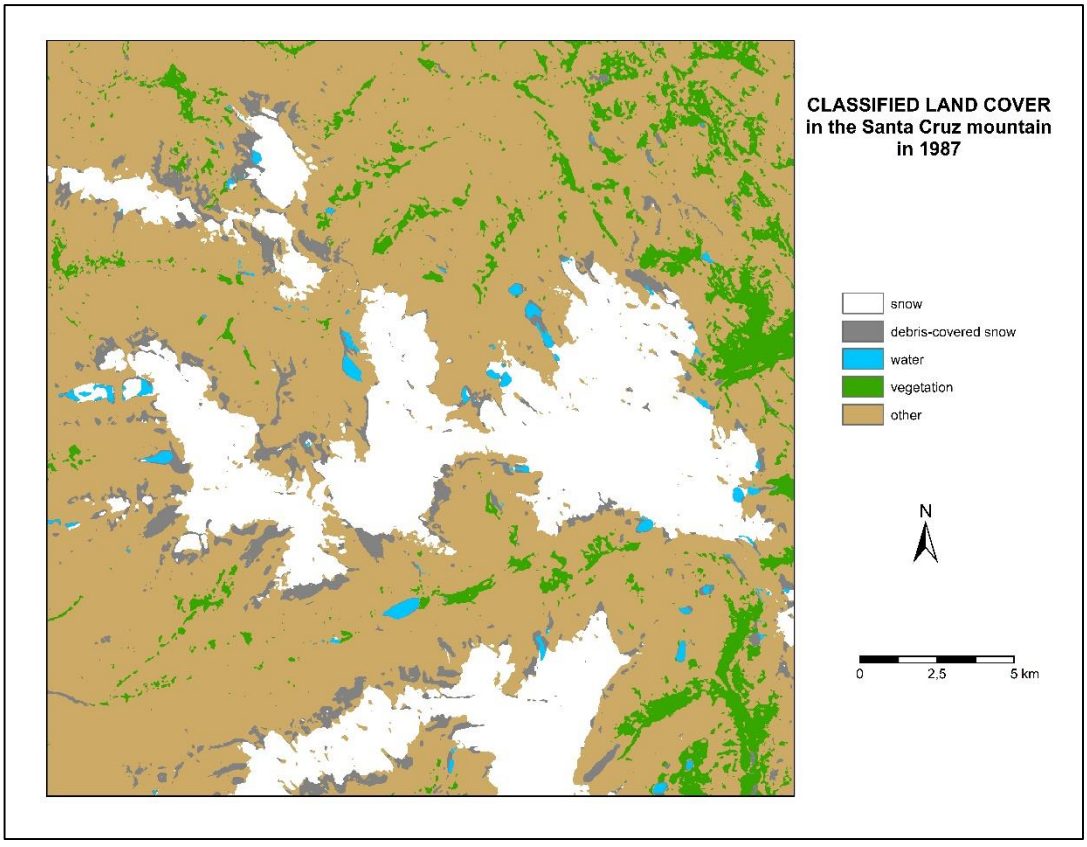

Appendix 15: Snow area and debris-covered snow area in the Cordillera Blanca (L4 – Landsat 4, L5 – Landsat 5, L7 – Landsat 7 and L8 – Landsat 8)

	Snow area [km^2]	**Debris-covered snow area [km^2]**
1987 L5	507,40	93,76
1988 L5	514,05	103,23
1989 L4	551,88	91,06
1989 L5	718,72	152,08
1990 L5	555,00	172,70
1991 L5	552,92	284,59
1992 L5	508,54	121,54
1993 L5	566,32	111,26
1994 L5	547,76	95,04
1995 L5	502,79	101,97
1996 L5	508,99	97,94
1997 L5	481,90	109,19
1998 L5	440,73	111,95
1999 L7	566,43	92,56
1999 L5	517,96	100,97
2000 L5	562,24	169,06
2001 L5	540,38	105,08
2002 L7	485,22	116,78
2003 L5	482,99	105,80
2004 L5	502,85	114,53
2005 L5	454,45	105,10
2006 L5	466,65	102,05
2007 L5	501,42	134,38
2008 L5	505,64	103,97
2009 L5	523,87	125,51
2010 L5	433,71	105,22
2011 L5	728,93	178,53
2013 L8	526,75	160,69
2014 L8	452,83	97,51

Appendix 16: Snowline change in the Huandoy South glacier

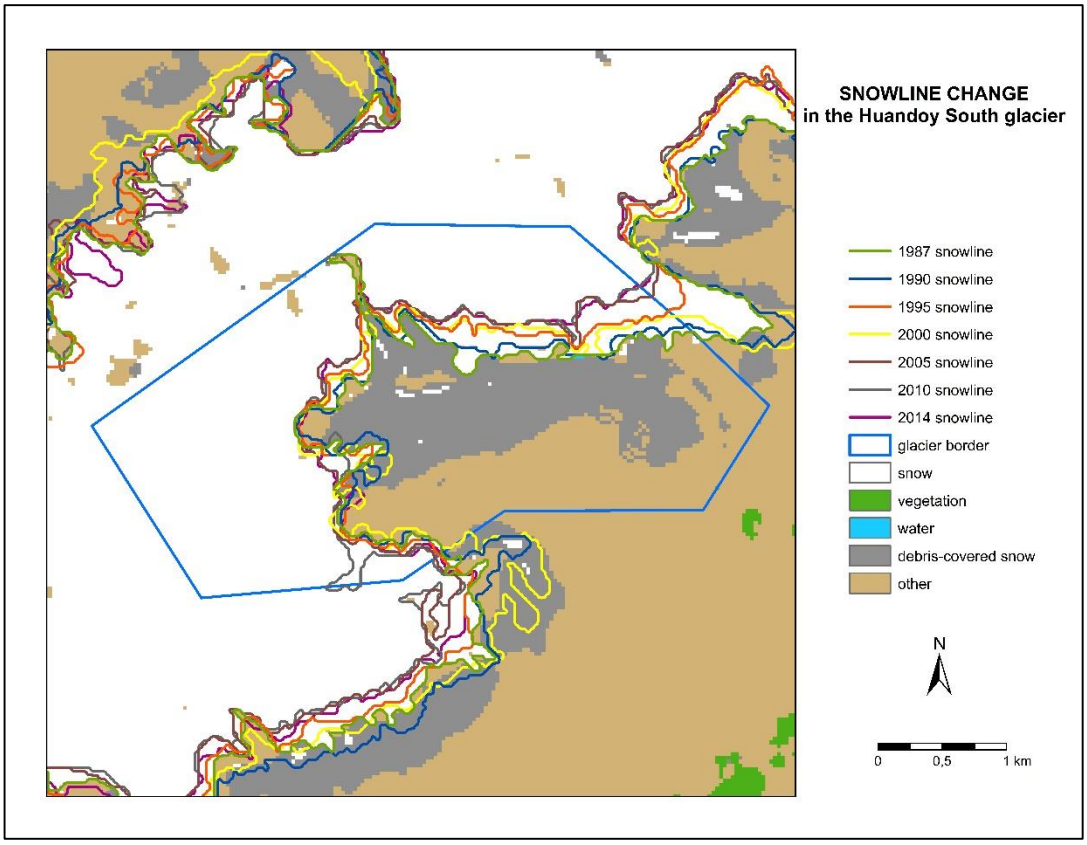

Appendix 17: Snowline change in the Huandoy East glacier

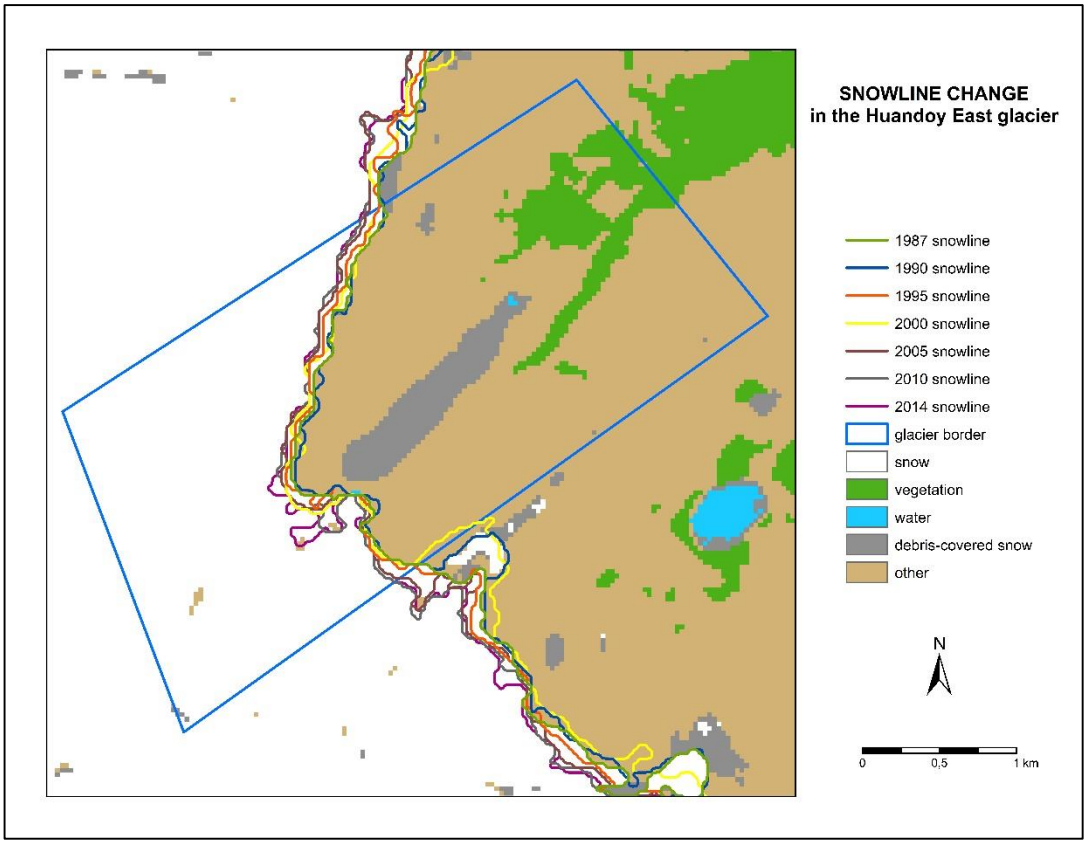

Appendix 18: Snowline change in the Piramide glacier

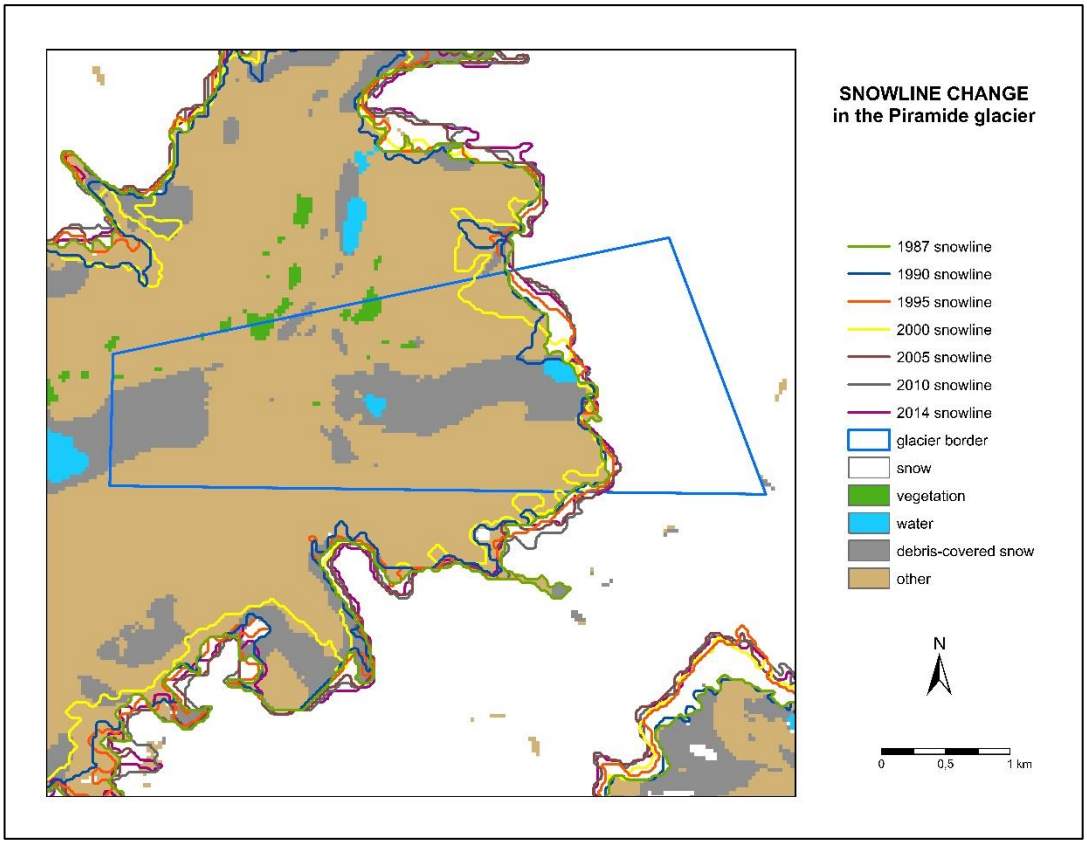

Appendix 19: Snowline change in the Huancotepampa glacier

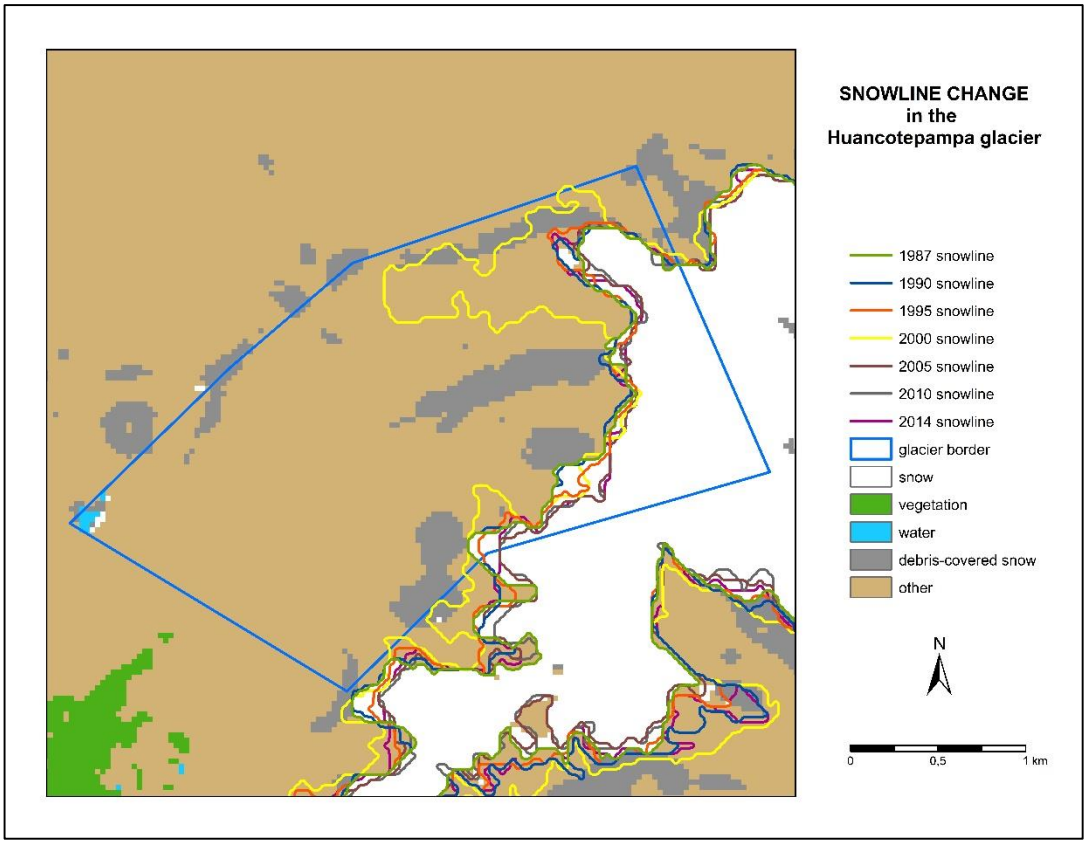

Appendix 20: Snowline change in the Knizl glacier

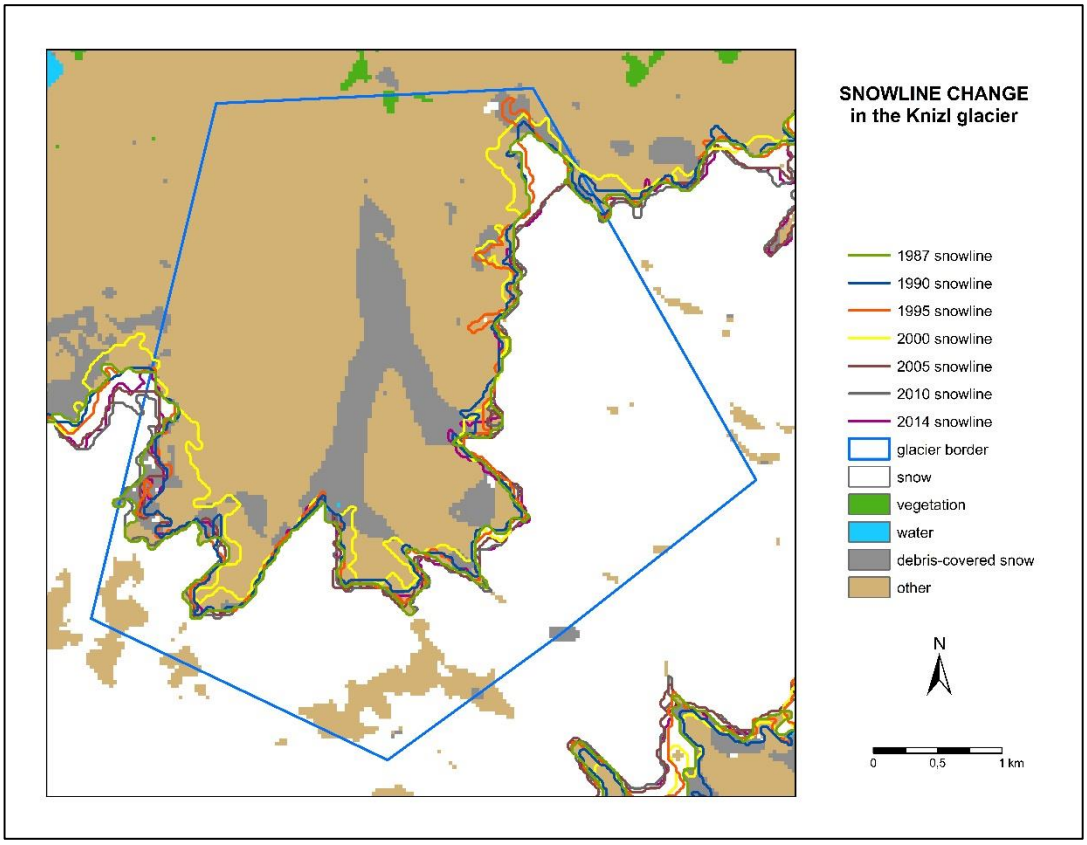

Appendix 21: Snowline change in the Schneider glacier

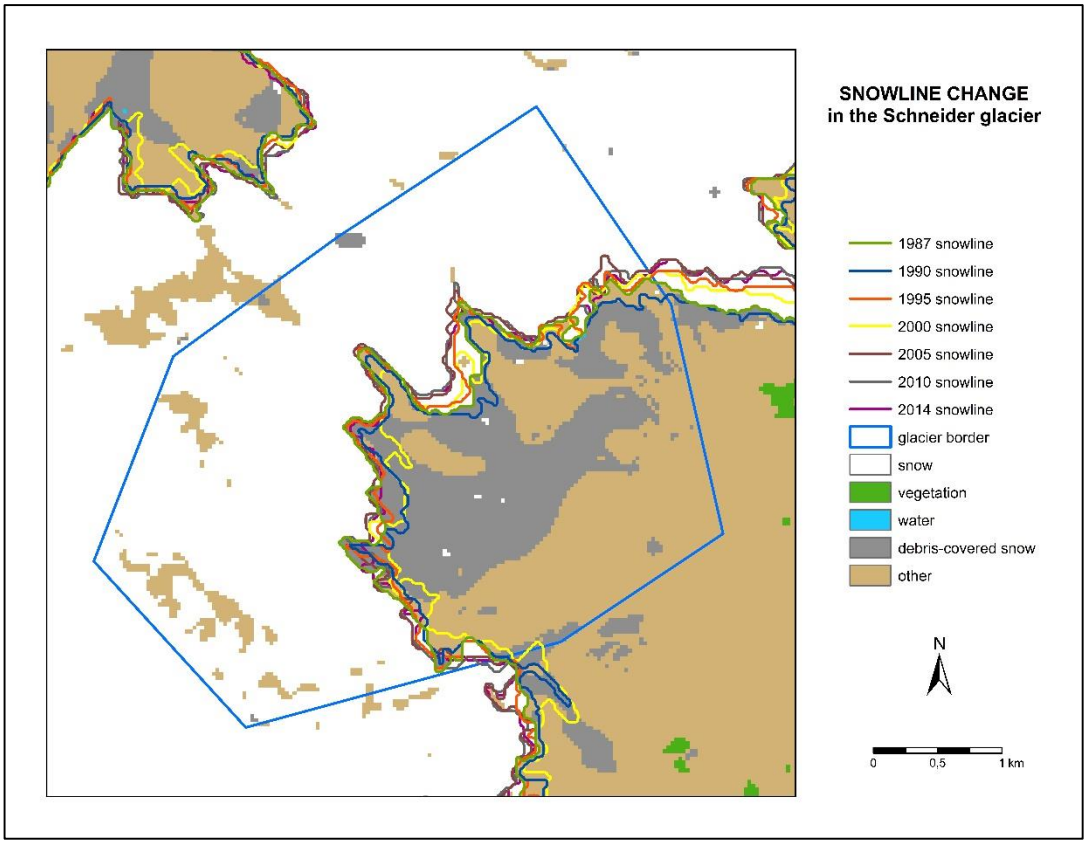

Appendix 22: Snowline change in the Cancahua glacier

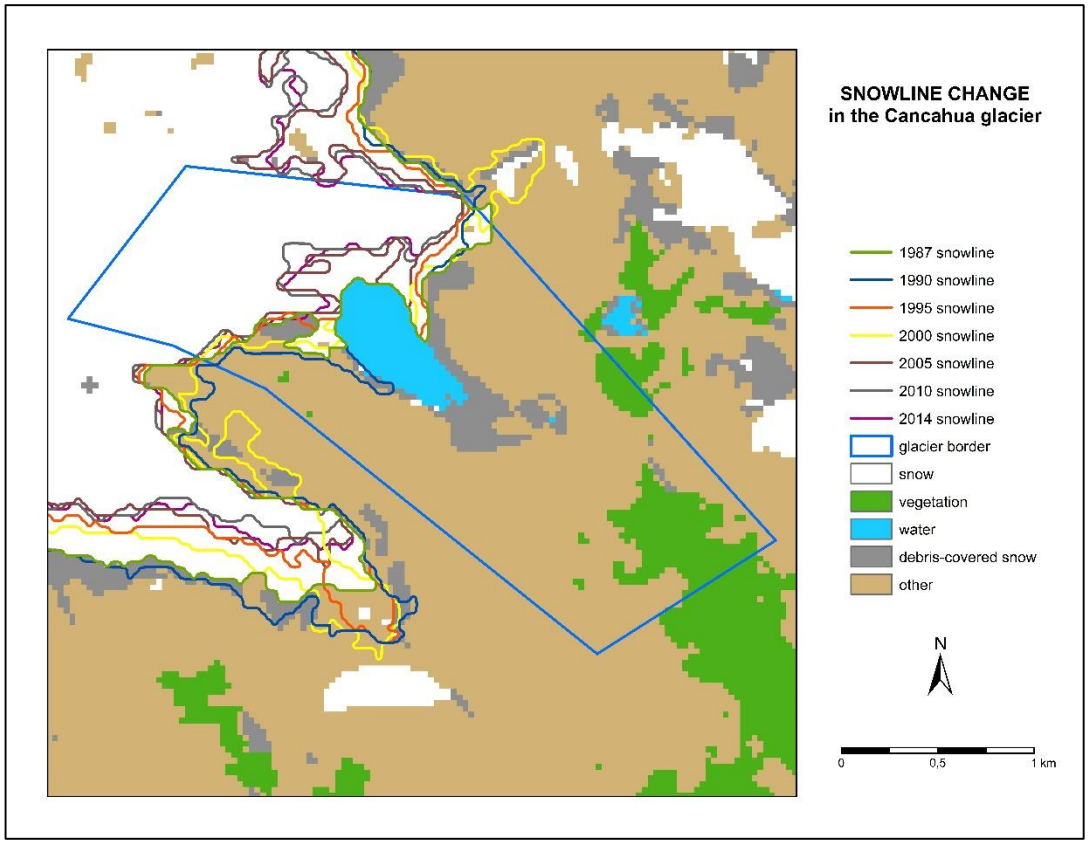

Appendix 23: Snowline change in the Santa Cruz West glacier

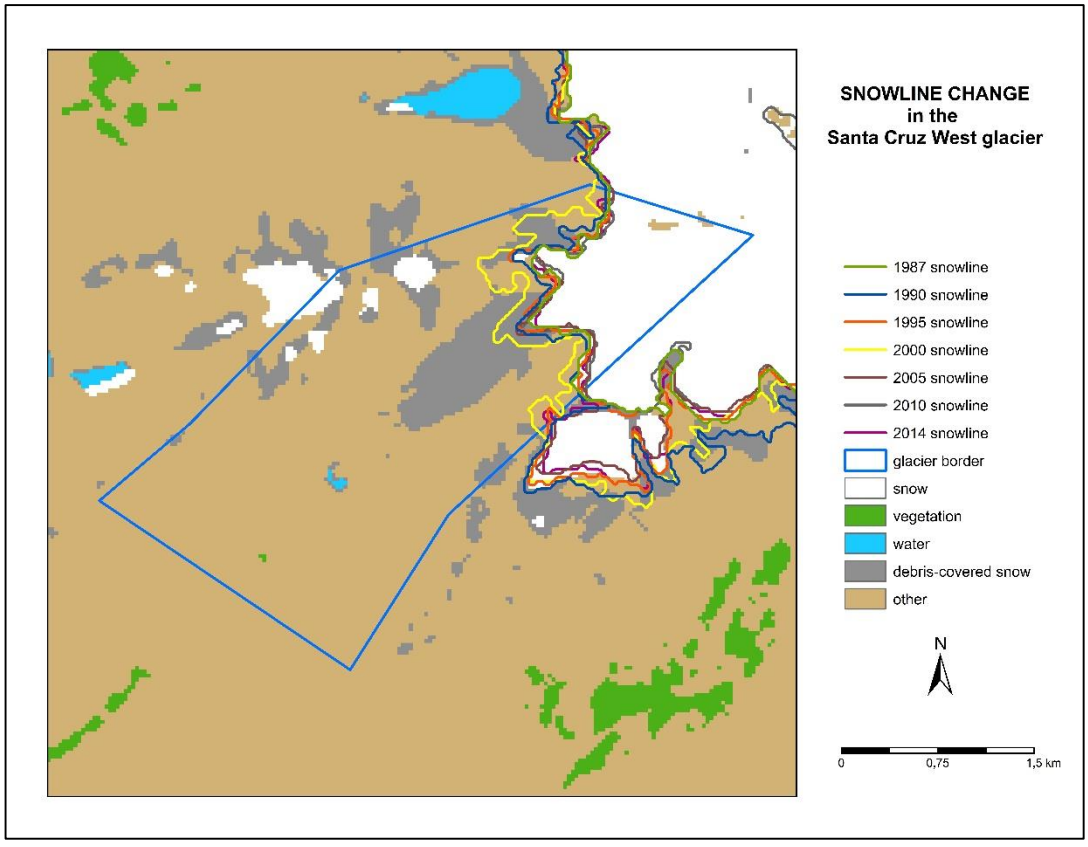

Appendix 24: Snowline change in the Santa Cruz South glacier

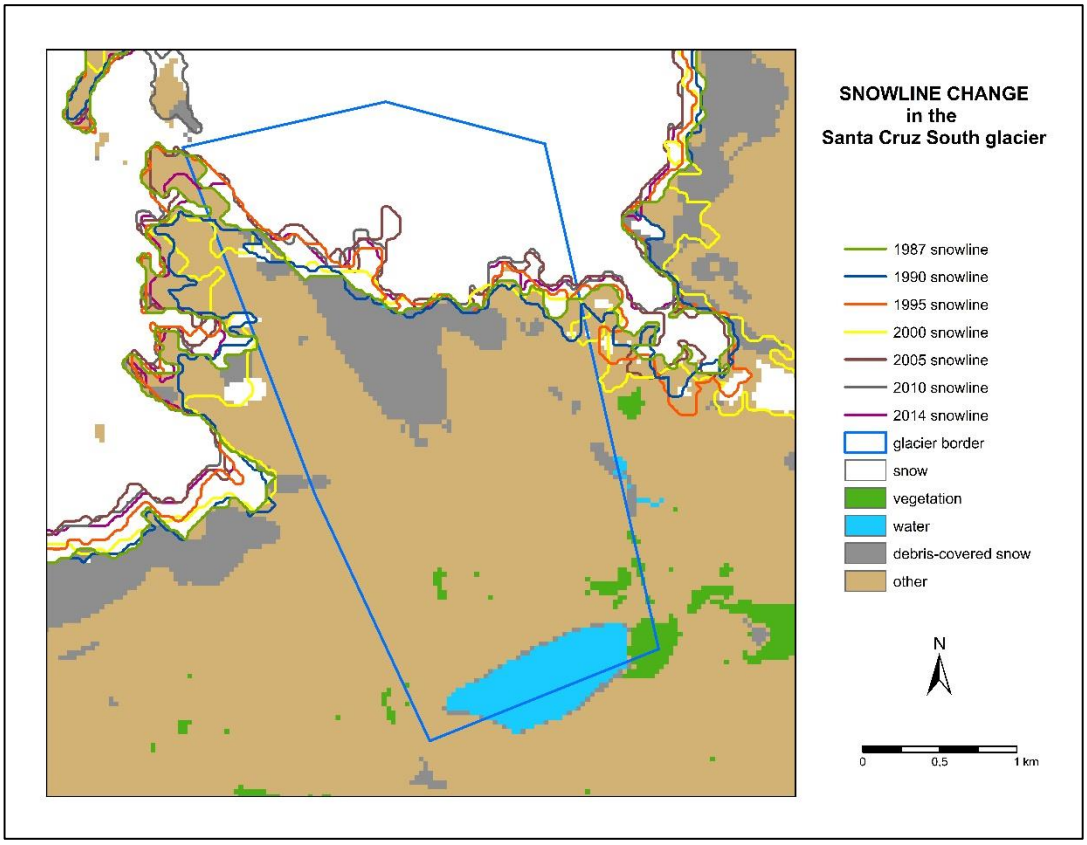

Appendix 25: Snowline change in the Paccharuri glacier

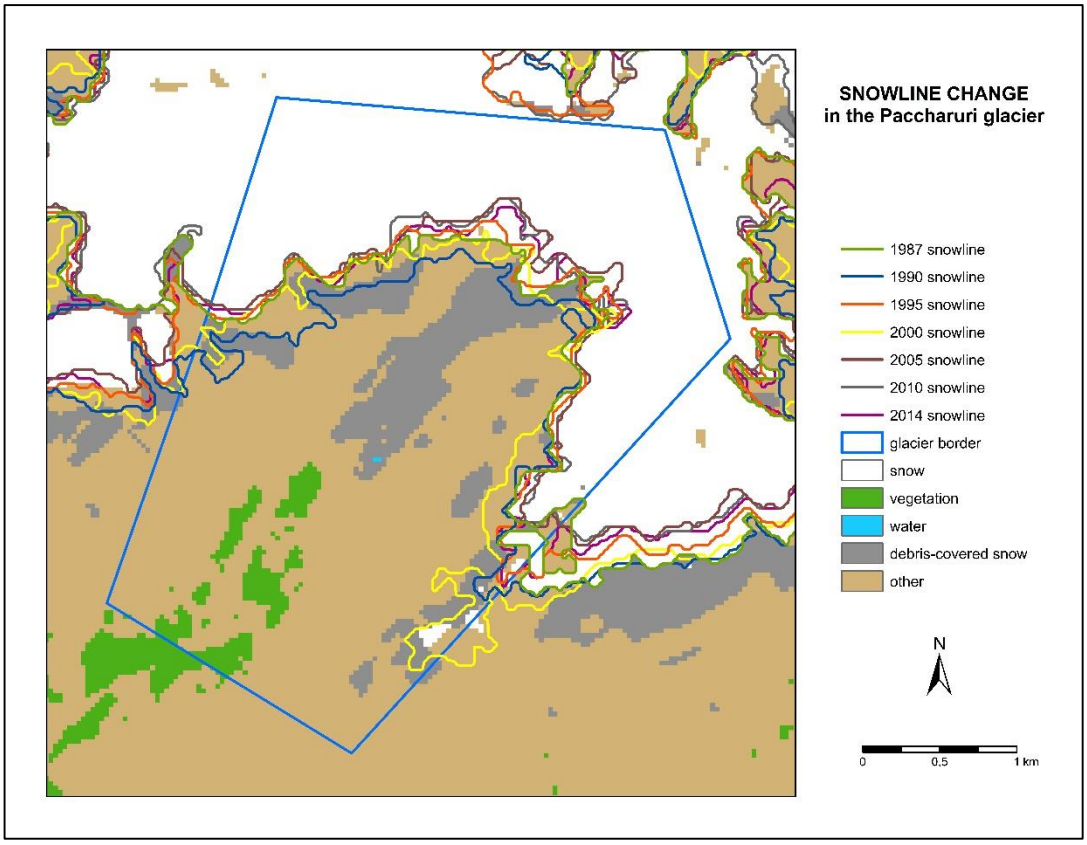

Appendix 26: Mean snowline altitude in the Cordillera Blanca (L4 – Landsat 4, L5 – Landsat 5, L7 – Landsat 7 and L8 – Landsat 8)

	Mean snowline altitude [m]		
	Huandoy mountain	**Huascarán mountain**	**Santa Cruz mountain**
1987 L5	5020,8	4933,7	4933,3
1988 L5	4999,5	4917,7	4926,4
1989 L4	4961,4	4896,2	4905,9
1989 L5	4813,7	4778,9	4806,7
1990 L5	4961,2	4901,5	4896,8
1991 L5	4991,7	4905,2	4888,6
1992 L5	5020,8	4966,8	4928,3
1993 L5	4973,7	4891,5	4882,3
1994 L5	4960,5	4895,4	4898,9
1995 L5	5016,7	4927,2	4937,3
1996 L5	5010,4	4924,6	4925,1
1997 L5	5029,5	4936,0	4952,6
1998 L5	5095,6	5034,0	4984,2
1999 L7	4926,2	4894,0	4892,3
1999 L5	4979,8	4921,3	4934,9
2000 L5	4940,8	4885,8	4896,9
2001 L5	4955,0	4899,8	4913,1
2002 L7	5052,6	4936,6	4955,4
2003 L5	5018,9	4942,0	4953,5
2004 L5	5008,8	4929,1	4939,5
2005 L5	5057,9	4954,8	4975,0
2006 L5	5049,6	4943,7	4964,9
2007 L5	5034,5	4943,5	4914,4
2008 L5	4980,8	4924,2	4932,3
2009 L5	4976,0	4900,1	4926,1
2010 L5	5056,5	4962,0	4992,5
2011 L5	4881,2	4851,4	
2013 L8	4914,7	4892,2	4894,4
2014 L8	5033,5	4947,4	4970,8

Appendix 27: Mean snowline altitude in the glaciers of the Huandoy mountain (L4 – Landsat 4, L5 – Landsat 5, L7 – Landsat 7 and L8 – Landsat 8)

	Mean snowline altitude [m]				
	Huancotepampa	**Huandoy East**	**Piramide**	**Huandoy South**	**Jatunraju**
1987 L5	5018,1	4740,2	4805,6	4957,4	5174,0
1988 L5	5025,3	4739,4	4809,0	4967,7	5124,4
1989 L4	5004,5	4740,0	4808,4	4933,8	5036,4
1989 L5	4923,9	4546,7	4626,9	4741,9	4851,1
1990 L5	5023,3	4728,2	4777,7	4932,9	5083,3
1991 L5	5026,1	4741,2	4812,5	4968,6	5293,3
1992 L5	5031,0	4680,9	4709,5	4984,6	5284,5
1993 L5	4997,4	4741,5	4770,6	4954,3	5103,7
1994 L5	5003,3	4738,3	4783,7	4946,2	5089,6
1995 L5	5042,6	4743,8	4819,3	4978,1	5160,8
1996 L5	5037,5	4748,2	4804,1	4984,2	5171,5
1997 L5	5051,4	4752,9	4824,4	4993,3	5227,1
1998 L5	5020,4	4776,9	4830,2	5067,3	5225,9
1999 L7	4992,7	4767,9	4801,3	4947,3	5014,2
1999 L5	5027,6	4778,0	4816,3	4973,4	5065,5

2000 L5	5013,3	4765,5	4803,0	4956,6	5055,7
2001 L5	5027,7	4755,9	4806,1	4943,3	5059,5
2002 L7	5054,2	4756,9	4815,0	5004,2	5250,6
2003 L5	5053,5	4757,5	4818,5	5007,2	5159,2
2004 L5	5057,3	4751,2	4819,0	4991,2	5179,8
2005 L5	5068,3	4769,7	4831,4	5035,0	5119,9
2006 L5	5042,9	4760,9	4821,1	5028,9	5145,8
2007 L5	5042,0	4766,2	4819,7	5015,2	5143,3
2008 L5	5024,9	4759,6	4814,3	4992,6	5030,6
2009 L5	5019,0	4758,7	4818,5	4991,6	5057,4
2010 L5	5065,5	4766,9	4835,4	5051,0	5189,5
2011 L5	4852,7	4735,3	4717,6	4918,6	4979,1
2013 L8	5054,2	4681,5	4682,9	4993,4	5058,1
2014 L8	5063,8	4770,6	4827,0	5014,9	5095,7

Appendix 28: Mean snowline altitude in the glaciers of the Huascarán mountain (L4 – Landsat 4, L5 – Landsat 5, L7 – Landsat 7 and L8 – Landsat 8)

	Mean snowline altitude [m]		
	Cancahua	**Schneider**	**Knizl**
1987 L5	4759,4	5009,2	5020,7
1988 L5	4760,6	5003,3	4987,2
1989 L4	4754,6	4986,4	4963,3
1989 L5	4694,3	4883,8	4824,9
1990 L5	4741,1	4975,1	4980,3
1991 L5	4770,9	4992,4	4975,1
1992 L5	4746,4	5025,9	5076,9
1993 L5	4768,0	5011,0	4924,3
1994 L5	4762,2	4986,4	4941,3
1995 L5	4774,6	5004,1	4984,8
1996 L5	4772,7	5017,3	4976,6
1997 L5	4765,9	5021,2	5006,1
1998 L5	4787,0	5097,4	5119,5
1999 L7	4751,9	5010,5	4953,4
1999 L5	4774,8	5026,0	4974,6
2000 L5	4769,3	4962,9	4930,4
2001 L5	4769,4	4983,4	4938,0
2002 L7	4777,4	5022,3	5006,2
2003 L5	4778,4	5013,8	5010,7
2004 L5	4760,9	4993,3	4987,4
2005 L5	4796,9	5039,0	4999,3
2006 L5	4794,7	5017,5	5004,8
2007 L5	4786,7	5032,7	5009,1
2008 L5	4789,1	5011,5	4974,6
2009 L5	4777,7	4984,1	4944,8
2010 L5	4840,3	5040,0	5019,3
2011 L5	4752,2	4936,2	4926,1
2013 L8	4795,8	5002,0	4900,9
2014 L8	4847,1	5025,6	5000,0

Appendix 29: Mean snowline altitude in the glaciers of the Santa Cruz mountain (L4 – Landsat 4, L5 – Landsat 5, L7 – Landsat 7 and L8 – Landsat 8)

	Mean snowline altitude [m]		
	Santa Cruz South	**Santa Cruz West**	**Paccharuri**
1987 L5	4850,9	5019,6	5027,4
1988 L5	4863,5	4996,1	5022,8
1989 L4	4825,3	4977,8	4994,4
1989 L5	4778,8	4835,0	4873,8
1990 L5	4795,2	5000,4	4981,7
1991 L5	4800,6	5007,8	5037,2
1992 L5	4825,6	5003,8	5003,2
1993 L5	4782,8	4952,4	4995,1
1994 L5	4810,2	4965,6	4985,9
1995 L5	4855,4	5013,0	5019,3
1996 L5	4860,4	5014,6	5017,9
1997 L5	4848,7	5004,4	5008,0
1998 L5	4939,0	5006,6	5023,4
1999 L7	4790,9	4919,1	4978,5
1999 L5	4848,8	4976,1	5016,6
2000 L5	4819,7	4953,4	5007,3
2001 L5	4813,2	4953,2	5003,8
2002 L7	4885,9	5016,0	5030,2
2003 L5	4863,1	5003,3	5025,3
2004 L5	4805,5	5004,3	5009,0
2005 L5	4908,3	5009,8	5033,5
2006 L5	4875,3	5020,4	5036,2
2007 L5	4873,8	5012,2	5015,2
2008 L5	4845,0	4979,0	5007,6
2009 L5	4801,9	4956,6	5004,7
2010 L5	4884,6	5017,3	5029,0
2013 L8	4781,9	4962,9	4993,0
2014 L8	4857,5	5044,5	5029,7

Appendix 30: Glacier change depending on slope in the Huascarán mountain

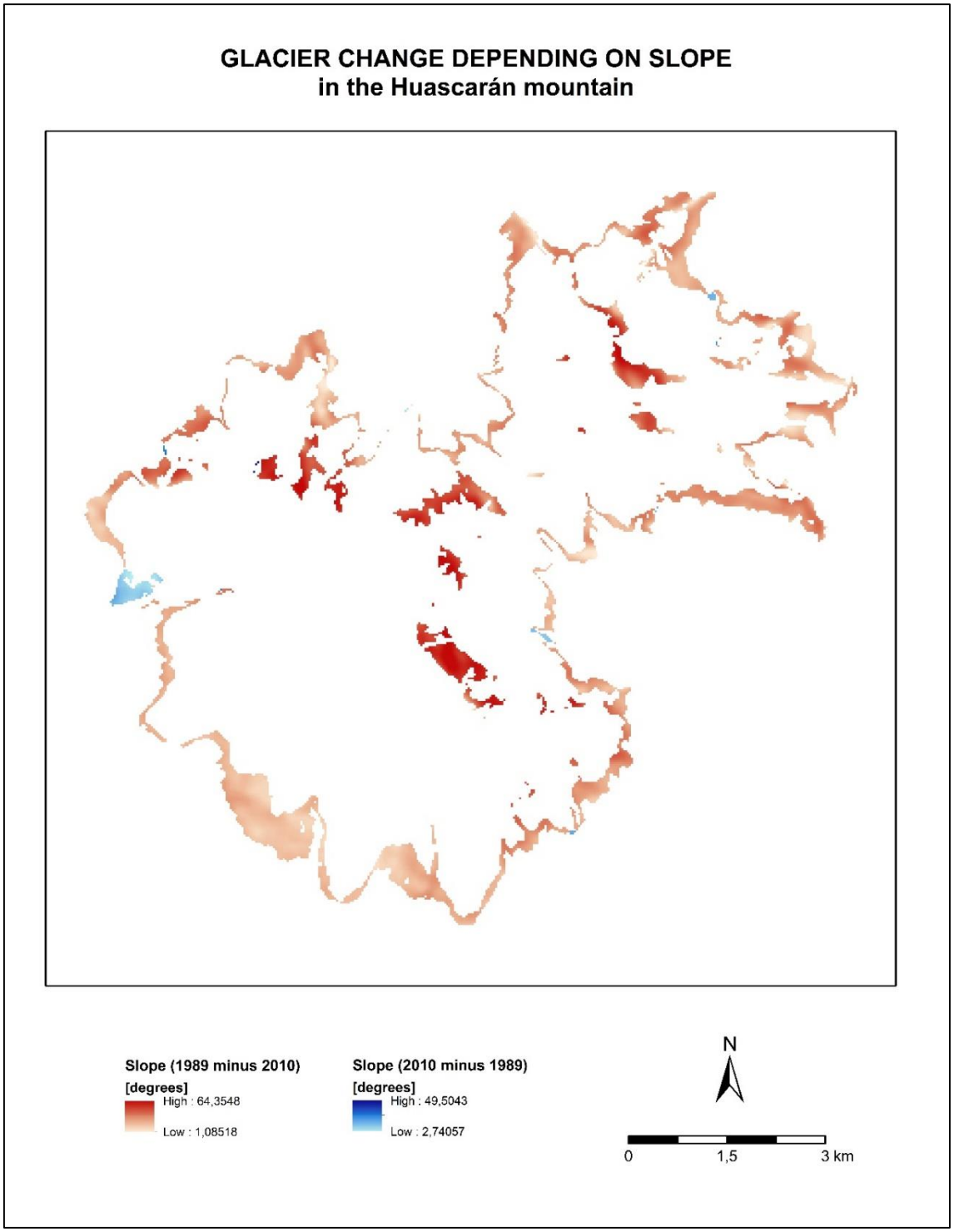

Appendix 31: Glacier change depending on slope in the Santa Cruz mountain

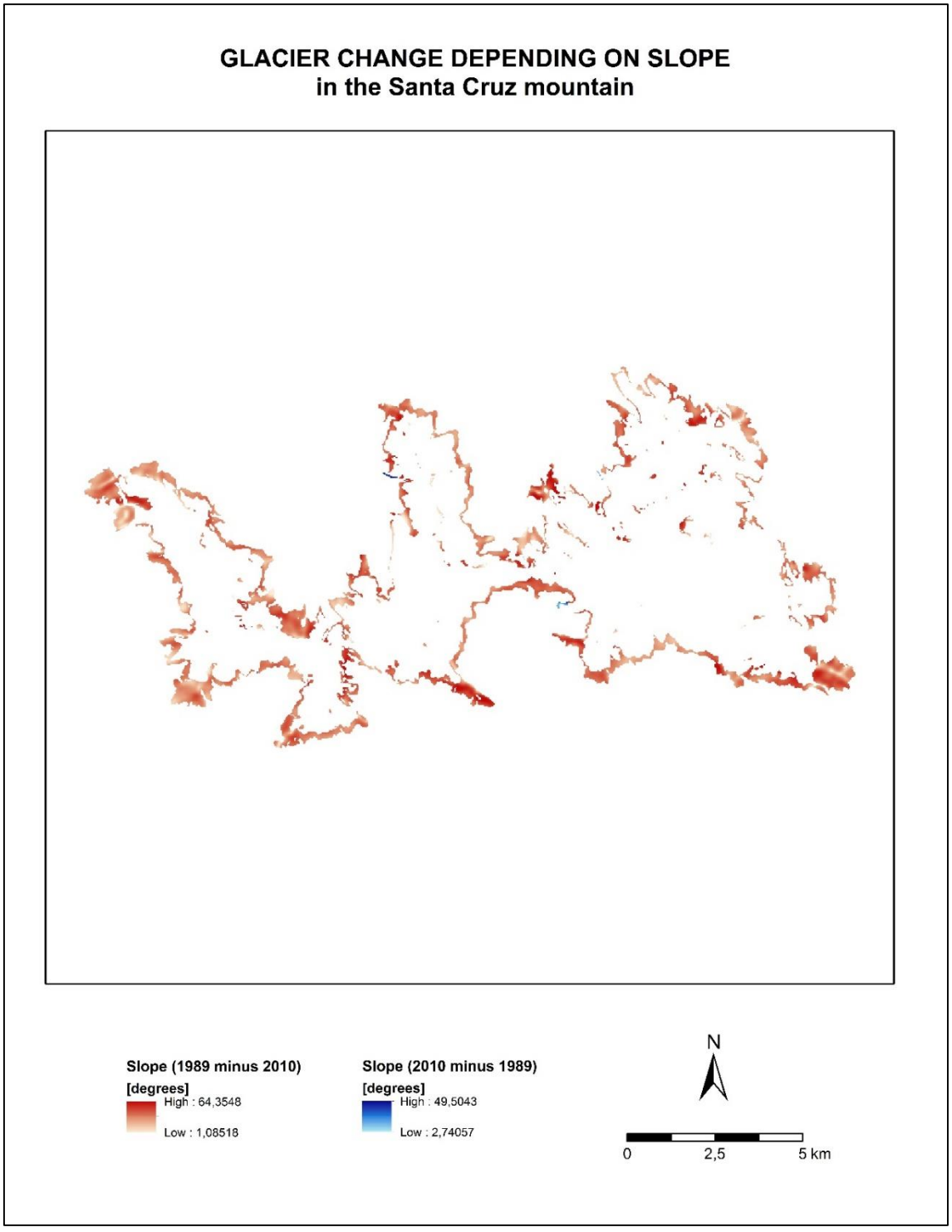

Appendix 32: Glacier change depending on slope in the Cordillera Blanca

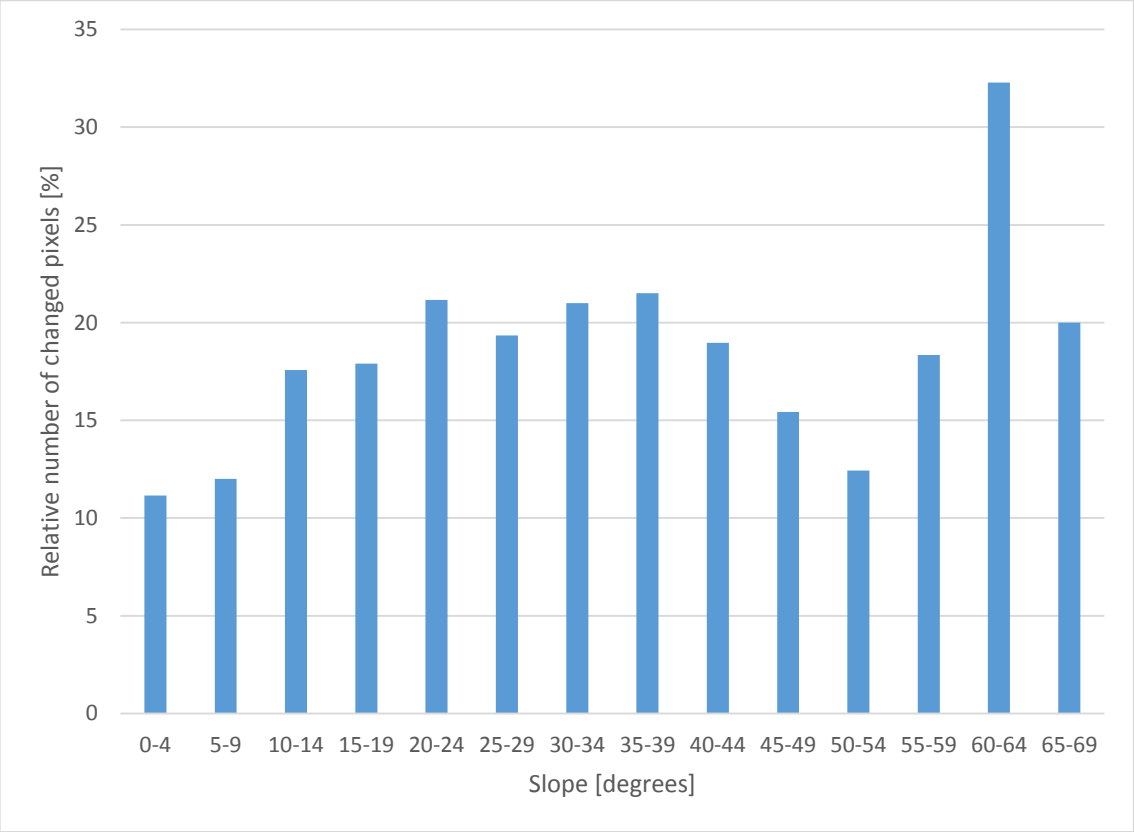

Appendix 33: Glacier change depending on slope in the Huascarán mountain

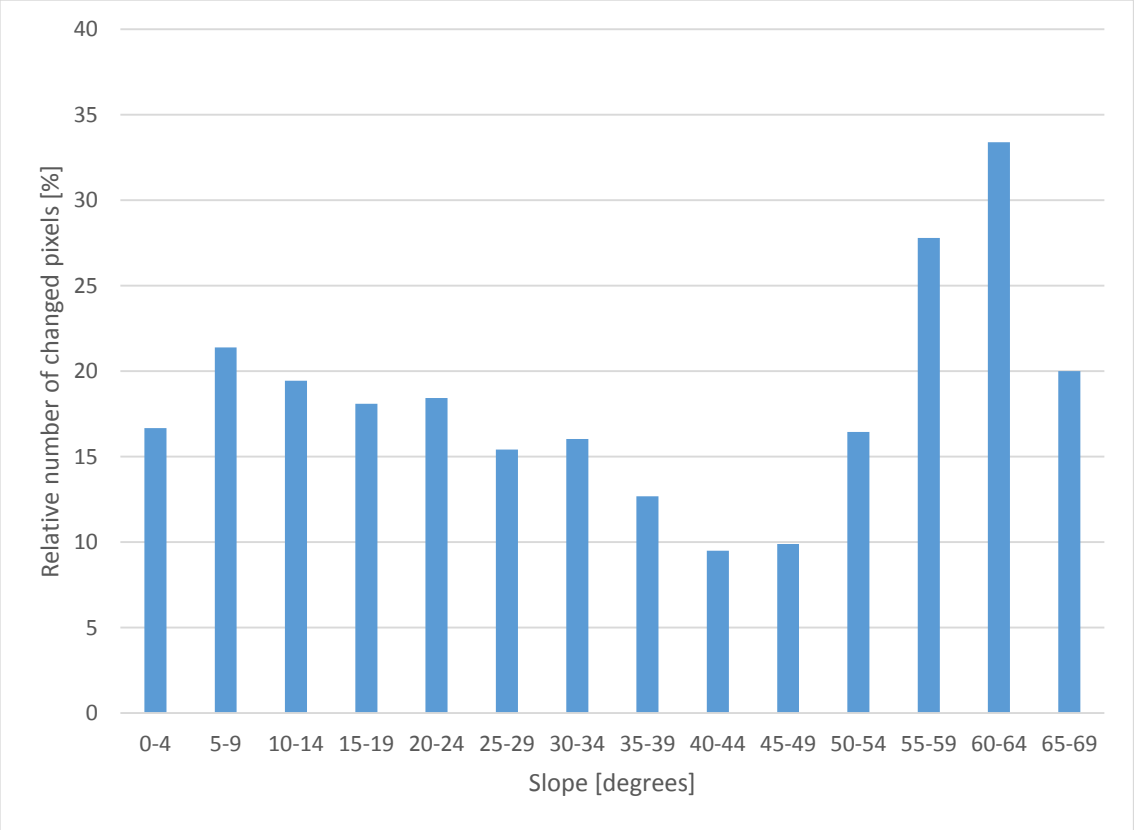

Appendix 34: Glacier change depending on slope in the Santa Cruz mountain

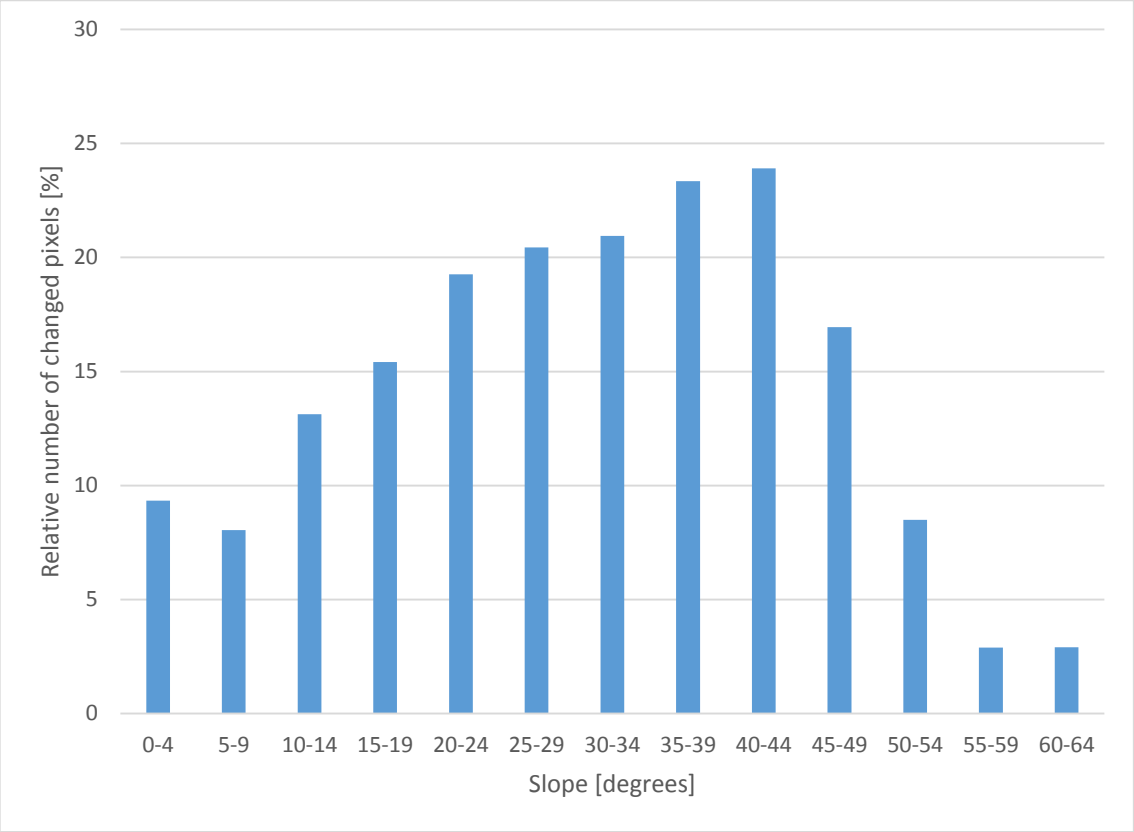

Appendix 35: Glacier change depending on slope in the Cordillera Blanca

Slope [degrees]	Relative number of changed pixels [%]			
	Cordillera Blanca	Huandoy mountain	Huascarán mountain	Santa Cruz mountain
0-4	11,15	15,31	16,67	9,34
5-9	12,01	16,89	21,38	8,05
10-14	17,57	24,92	19,45	13,13
15-19	17,90	22,25	18,08	15,41
20-24	21,16	23,63	18,43	19,27
25-29	19,35	21,73	15,42	20,44
30-34	21,01	23,40	16,03	20,95
35-39	21,50	24,56	12,67	23,34
40-44	18,96	22,89	9,50	23,92
45-49	15,42	18,23	9,90	16,95
50-54	12,43	11,12	16,45	8,49
55-59	18,35	10,31	27,79	2,90
60-64	32,28	50,35	33,38	2,90
65-69	20,00		20,00	

Appendix 36: Glacier change depending on aspect in the Huascarán mountain

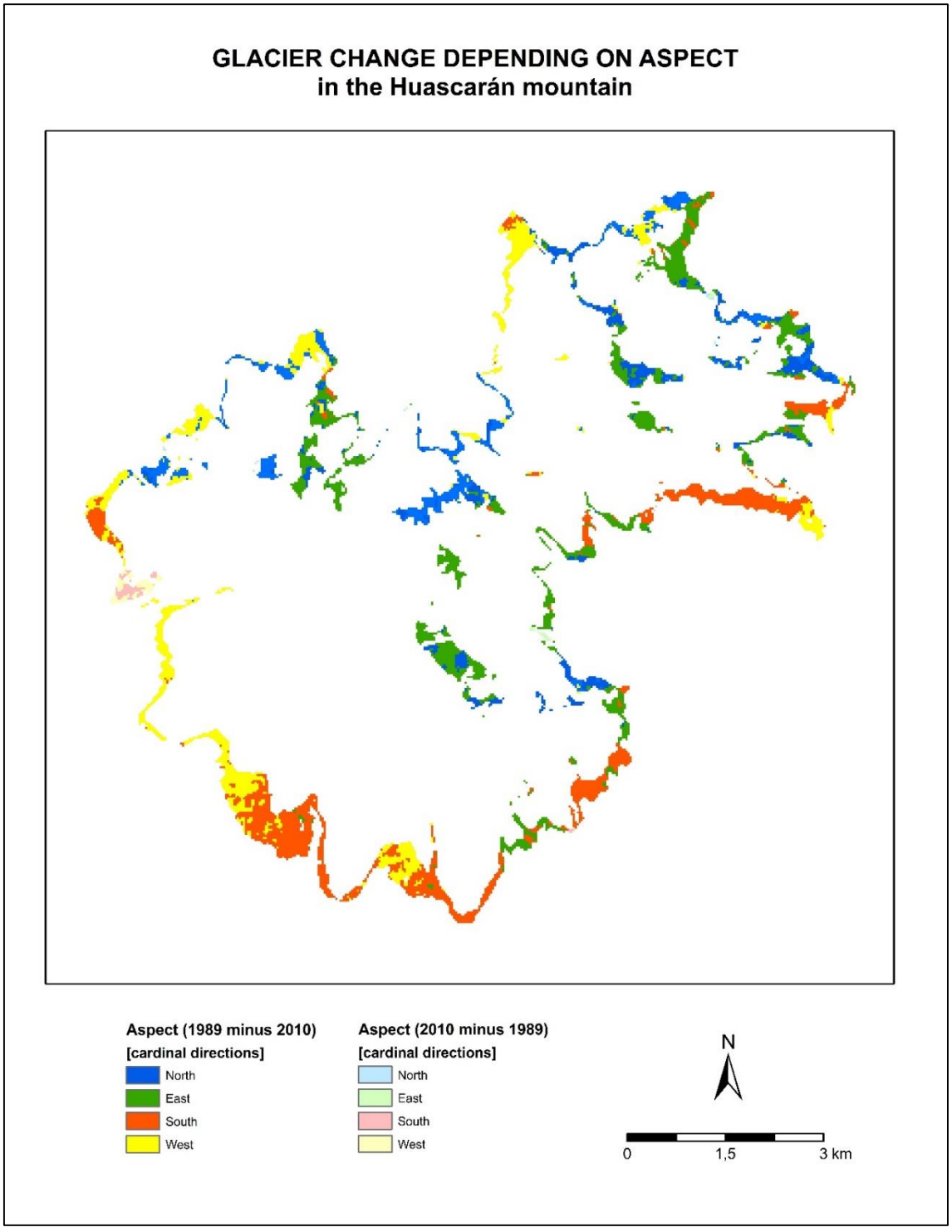

Appendix 37: Glacier change depending on aspect in the Santa Cruz mountain

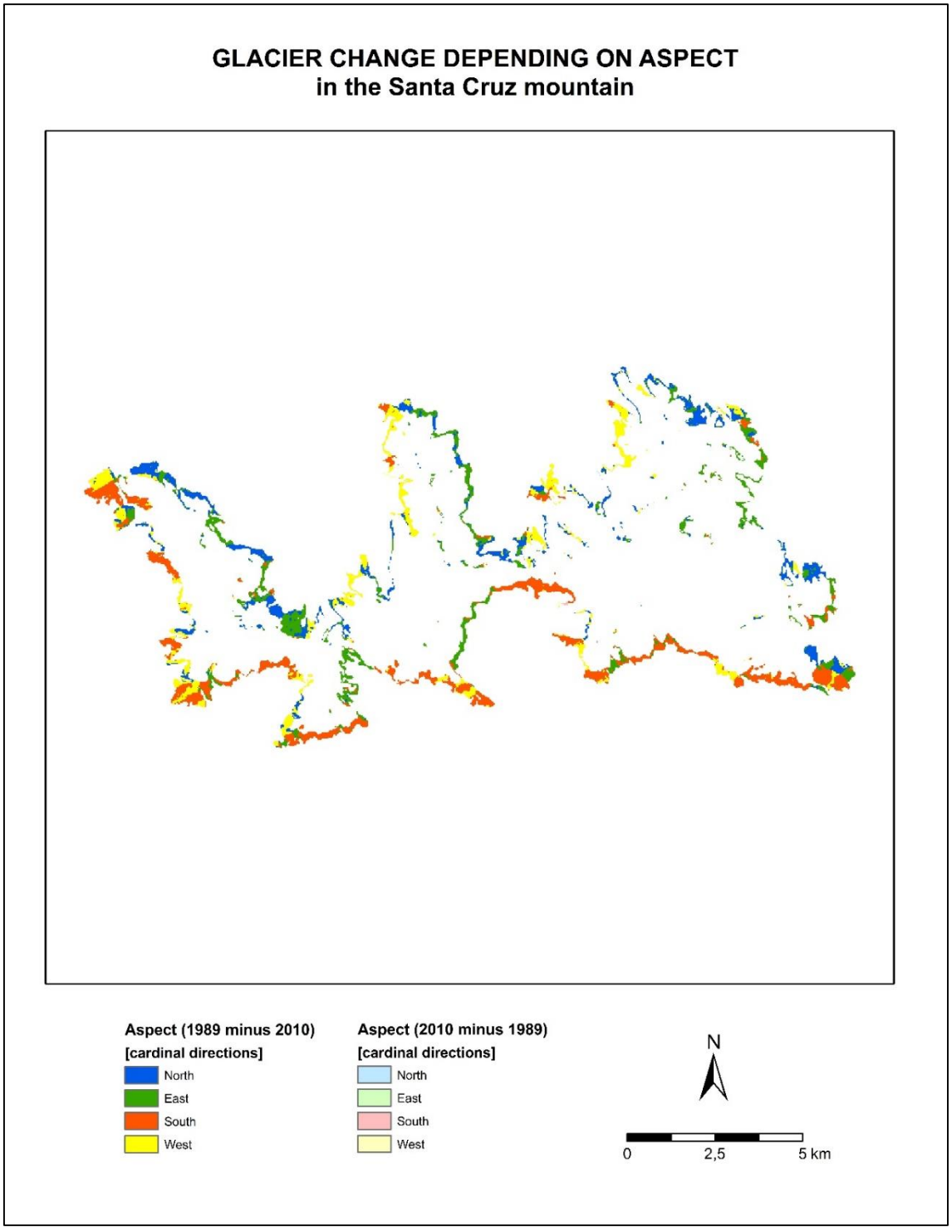

Appendix 38: Glacier change depending on aspect (4 cardinal directions) in the Cordillera Blanca

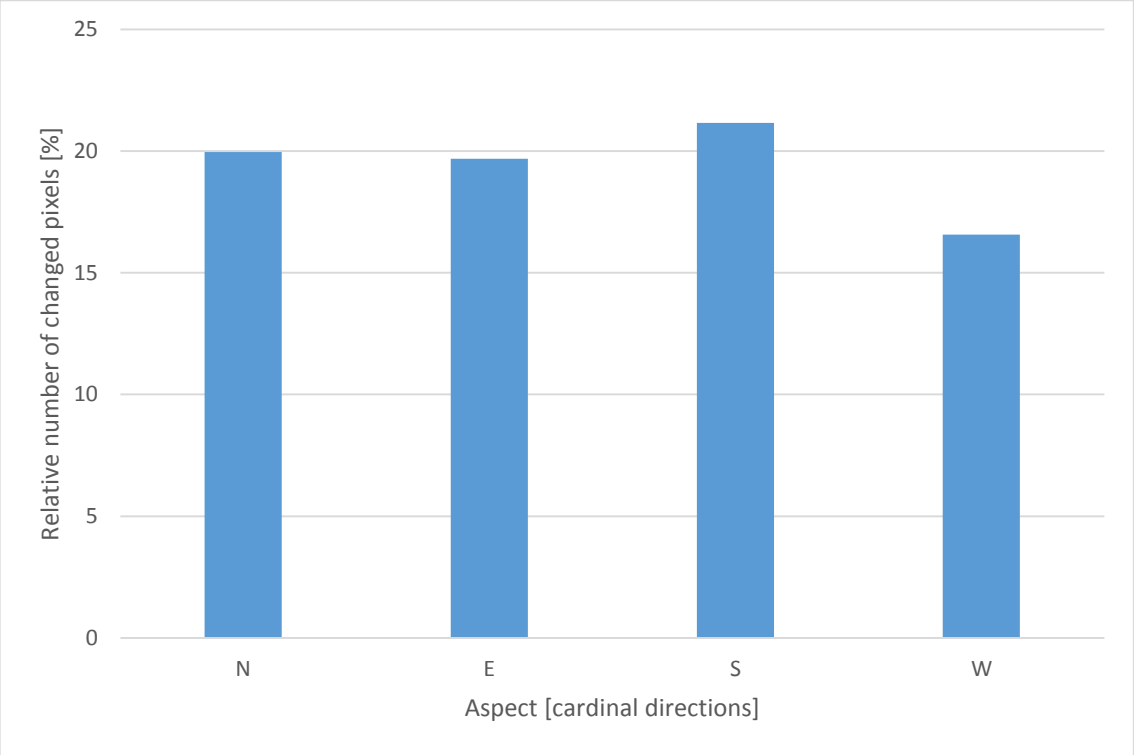

Appendix 39: Glacier change depending on aspect (8 cardinal directions) in the Cordillera Blanca

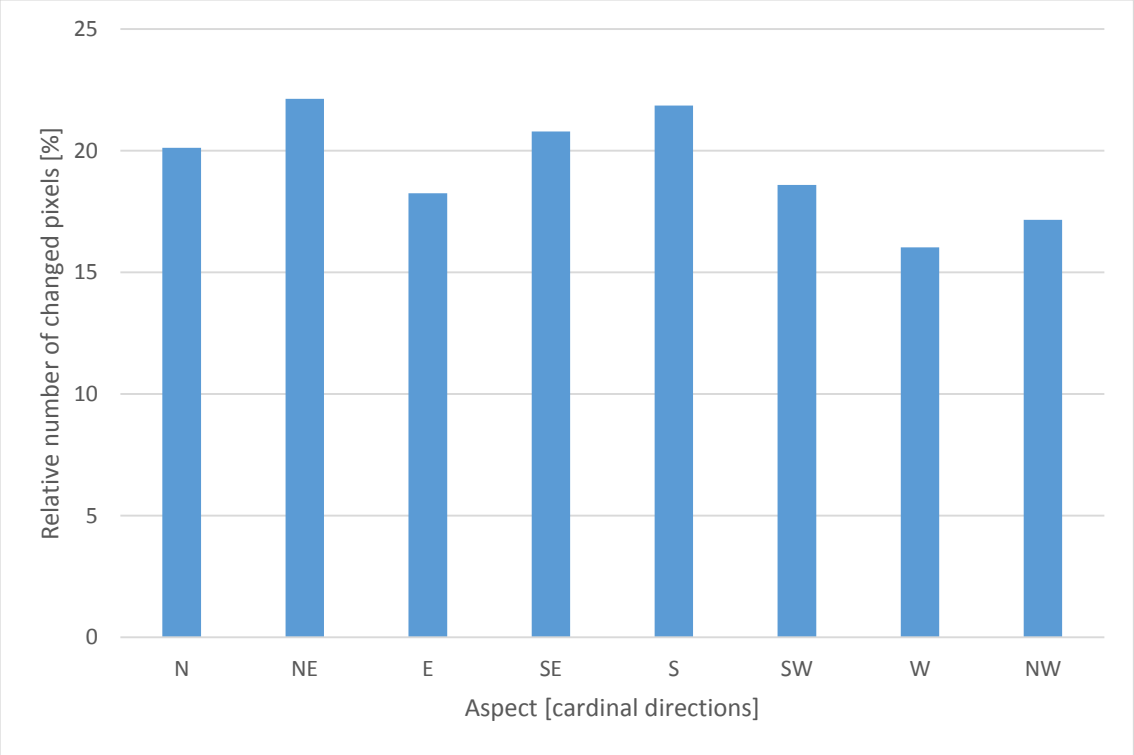

Appendix 40: Glacier change depending on aspect (4 cardinal directions) in the Huascarán mountain

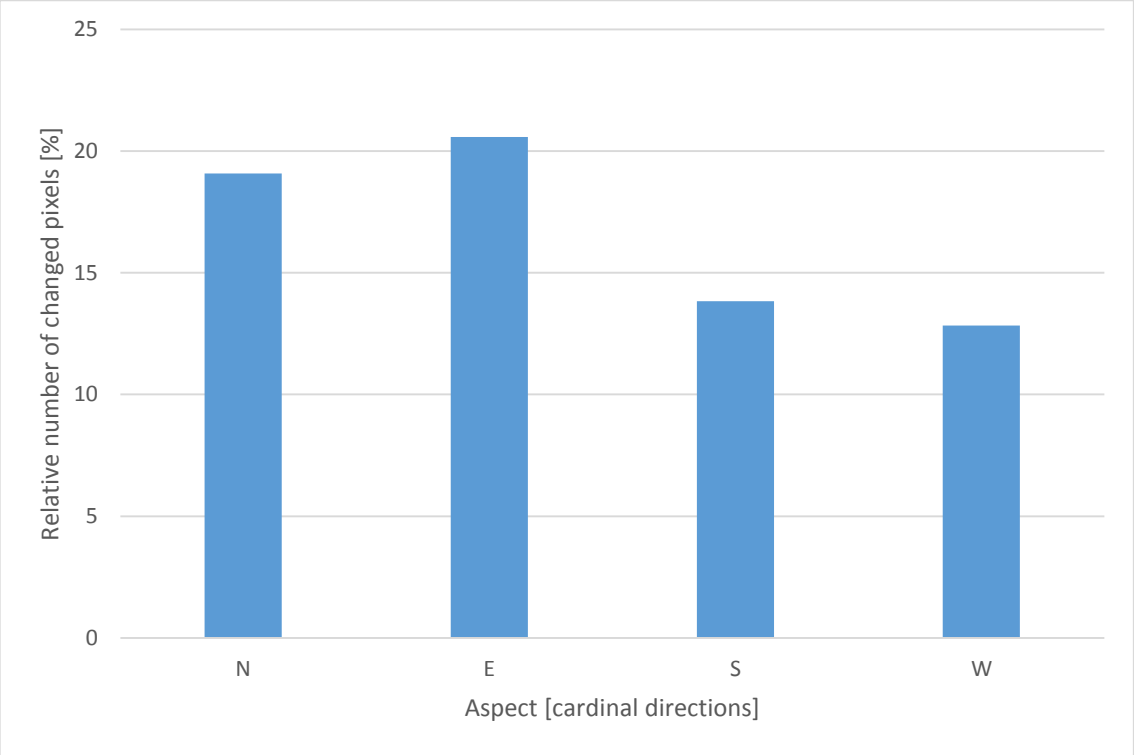

Appendix 41: Glacier change depending on aspect (8 cardinal directions) in the Huascarán mountain

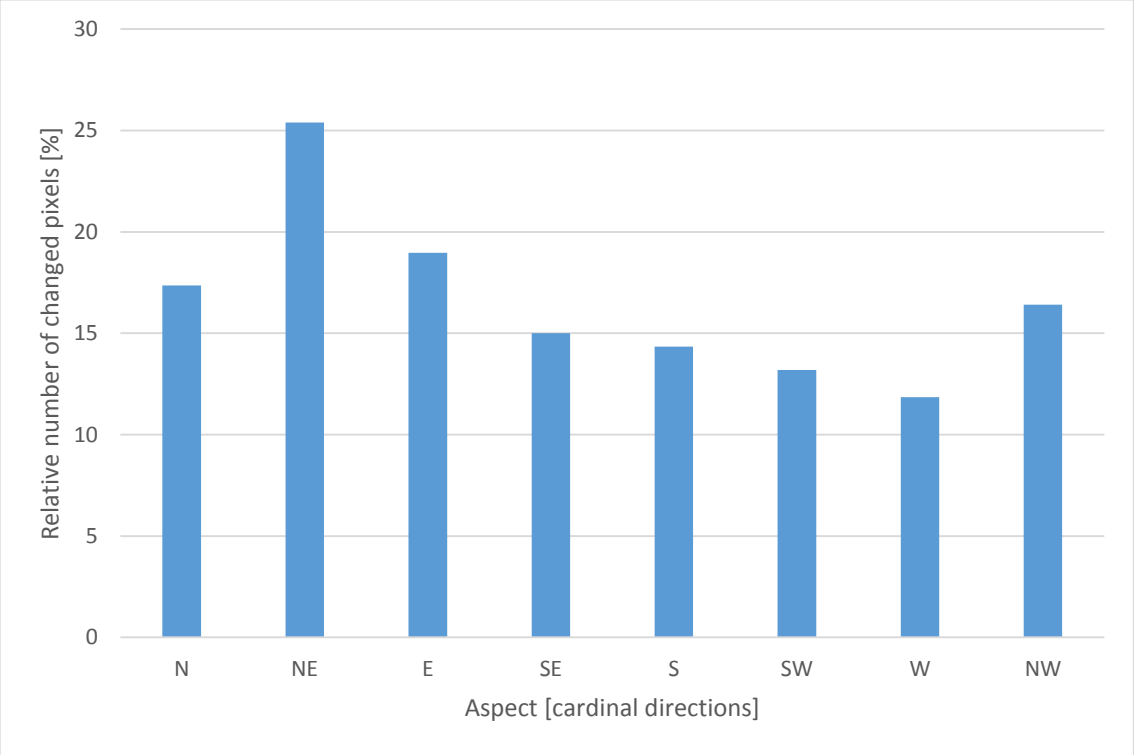

Appendix 42: Glacier change depending on aspect (4 cardinal directions) in the Santa Cruz mountain

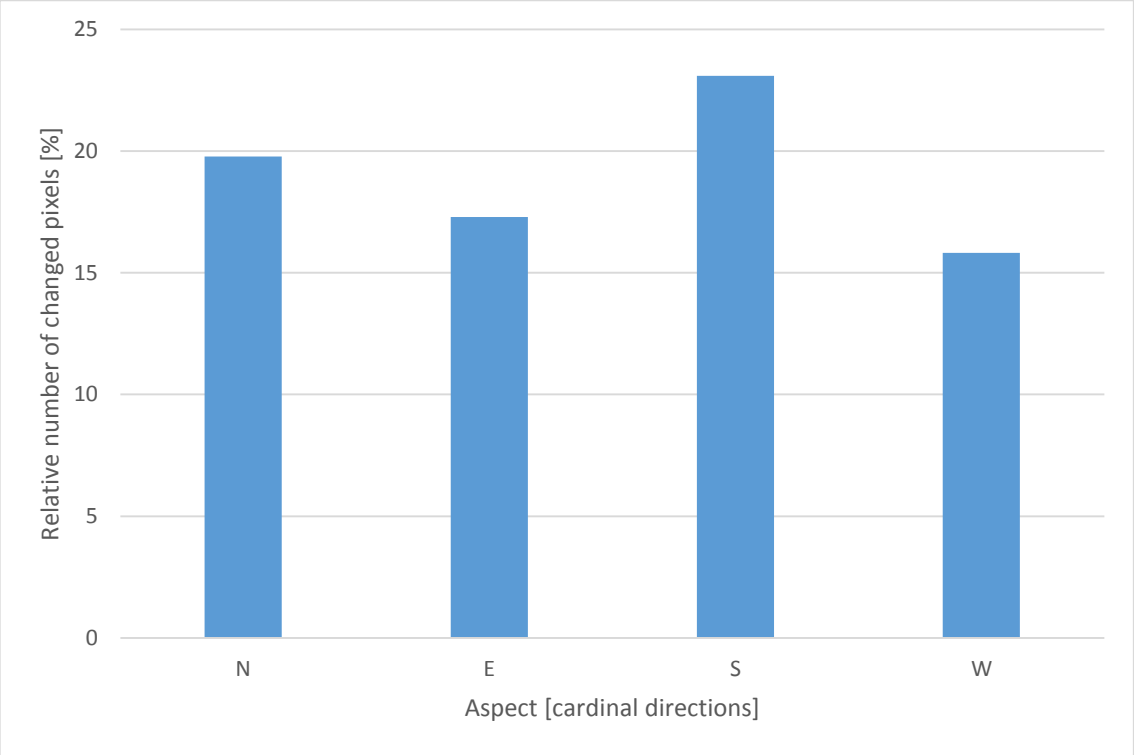

Appendix 43: Glacier change depending on aspect (8 cardinal directions) in the Santa Cruz mountain

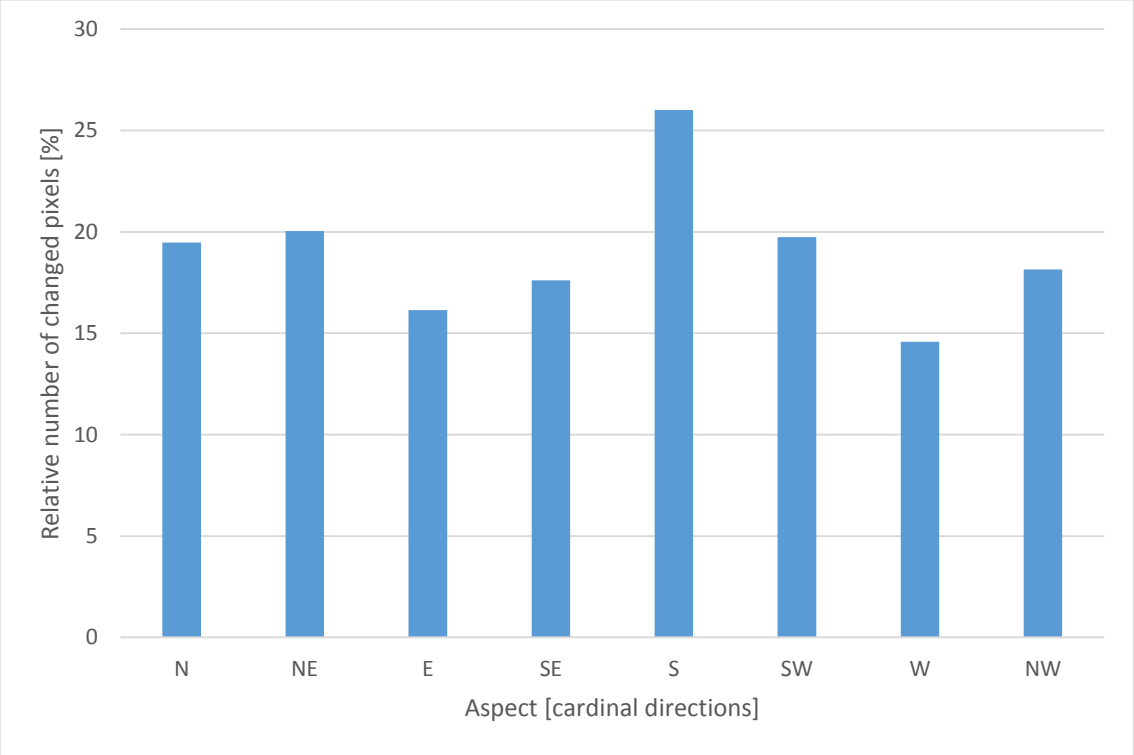

Appendix 44: Glacier change depending on aspect in the Cordillera Blanca

Aspect [cardinal directions]	Relative number of changed pixels [%]			
	Cordillera Blanca	Huandoy mountain	Huascarán mountain	Santa Cruz mountain
N	19,97	20,75	19,08	19,78
E	19,69	22,03	20,59	17,30
S	21,16	24,94	13,83	23,10
W	16,57	20,70	12,83	15,82
N	20,12	22,72	17,35	19,47
NE	22,13	22,91	25,40	20,03
E	18,26	20,35	18,97	16,15
SE	20,79	26,52	15,01	17,61
S	21,86	23,60	14,34	26,01
SW	18,59	24,83	13,20	19,74
W	16,03	21,62	11,85	14,57
NW	17,16	16,72	16,41	18,15

Appendix 45: Content of the attached digital disk

- digital version of this diploma thesis
- correlation computation by ArcMap and Matlab
- classification results (raster images and maps)
- results of the mean snowline altitude change (shapefiles, raster images and maps)
- results of the slope and aspect analyses (shapefiles, raster images and maps)